

**UNIVERSIDADE DE LISBOA  
INSTITUTO SUPERIOR TÉCNICO**

**Numerical modelling of hydrodynamics and  
sediment transport in coastal systems**

**Guilherme Augusto Stefanelo Franz**

**Supervisor: Doctor Ramiro Joaquim de Jesus Neves  
Co-Supervisor: Doctor Paulo Miguel Chambel Filipe Lopes Leitão**

**Thesis approved in public session to obtain the PhD Degree in  
Environmental Engineering**

**Jury final classification: Pass with Distinction**

**Jury**

**Chairperson: Chairman of the IST Scientific Board**

**Members of the Committee:**

**Doctor Maurício Almeida Noernberg  
Doctor Ramiro Joaquim de Jesus Neves  
Doctor André Bustorff Fortunato  
Doctor António Alberto Pires Silva**



**UNIVERSIDADE DE LISBOA**  
**INSTITUTO SUPERIOR TÉCNICO**

# **Numerical modelling of hydrodynamics and sediment transport in coastal systems**

**Guilherme Augusto Stefanelo Franz**

**Supervisor: Doctor Ramiro Joaquim de Jesus Neves**

**Co-Supervisor: Doctor Paulo Miguel Chambel Filipe Lopes Leitão**

**Thesis approved in public session to obtain the PhD Degree in  
Environmental Engineering**

**Jury final classification: Pass with Distinction**

**Jury**

**Chairperson: Chairman of the IST Scientific Board**

**Members of the Committee:**

**Doctor Maurício Almeida Noernberg, Professor Associado do Centro de  
Estudos do Mar da Universidade Federal do Paraná, Brasil**

**Doctor Ramiro Joaquim de Jesus Neves, Professor Associado do Instituto  
Superior Técnico da Universidade de Lisboa**

**Doctor André Bustorff Fortunato, Investigador Principal com Habilitação  
do Laboratório Nacional de Engenharia Civil**

**Doctor António Alberto Pires Silva, Professor Associado do Instituto  
Superior Técnico da Universidade de Lisboa**

**Funding Institutions**

**Brazilian National Council for Scientific and Technological Development (CNPQ)  
*Ciências Sem Fronteiras* program (research grant no. 237448/2012-2)**

**2017**



*To my mother, who taught me to walk.*

*To my wife, who walked with me throughout this journey.*



# Abstract

Coastal systems are dynamic environments that are often subjected to intense anthropogenic pressures. Numerical models can represent the diverse natural processes and predict the impacts of human interventions, which is particularly relevant for the study of sediment transport and morphological changes. The central aim of this thesis is to develop and test a numerical modelling approach for the study of hydrodynamics and sediment dynamics in coastal systems, in order to support an effective coastal management. This goal encompasses the verification of a methodology replicable for diverse coastal systems. The MOHID modelling system was the main numerical tool adopted for this purpose. Firstly, the applicability of a numerical model following a downscaling methodology was evaluated for the south-eastern Brazilian shelf (regional model) and Paranaguá estuarine system (local model). This approach permits the simulation of different scale processes, providing realistic oceanic boundary conditions for the local model. Afterwards, a numerical approach was followed to investigate the main factors that influence the cohesive sediment dynamics in an estuarine system composed of large mudflats (Tagus estuary, Portugal). The comprehension of cohesive sediment dynamics in estuarine systems is vital for an effective coastal management, as cohesive sediments are related to several engineering problems and environmental concerns. The main novelty of this thesis is the development of a morphological model that enables the simultaneous assessment of the transport of multiple sediment fractions (non-cohesive and cohesive) and associated morphological evolution. The effects of sediment mixtures and bed consolidation on resistance to erosion were considered, whereas the multi-layer bottom column permits a representation of the bottom stratigraphy. The morphological model was applied to schematic cases and laboratory experiments in order to evaluate its performance. In a real test case, the model was applied to the Tagus estuary to investigate the generation of realistic sediment distribution based on the local hydrodynamic conditions. The model applicability was also tested under the combined action of waves and currents. For this purpose, the MOHID modelling system was coupled with the SWAN wave model to simulate the impact of different designs of coastal defence structures (detached breakwaters and groynes) and the formation of sandbars. The same modelling methodology was applied to a coastal zone (Costa da Caparica) located at the mouth of the Tagus Estuary to evaluate the hydrodynamics and sediment transport in calm water conditions and during events of highly energetic waves. The outcomes of these test cases confirmed the model potential to be used as a valuable tool for engineering studies.

Keywords: hydrodynamics; morphodynamics; sediment transport; coastal systems; MOHID modelling system



# Resumo

Os sistemas costeiros são ambientes dinâmicos que são frequentemente submetidos a intensas pressões antrópicas. Modelos numéricos podem representar os diversos processos naturais e prever os impactos das intervenções humanas, o que é particularmente relevante para o estudo do transporte de sedimentos e alterações morfológicas. O objectivo central desta tese é desenvolver e testar uma abordagem de modelação numérica para o estudo da hidrodinâmica e dinâmica de sedimentos em sistemas costeiros, a fim de apoiar uma gestão costeira eficaz. Este objectivo abrange a verificação de uma metodologia replicável para diversos sistemas costeiros. O sistema de modelação MOHID foi a principal ferramenta numérica adoptada para este fim. Em primeiro lugar, avaliou-se a aplicabilidade de um modelo numérico seguindo a metodologia de downscaling para a plataforma do Sudeste do Brasil (modelo regional) e para o estuário de Paranaguá (modelo local). Esta abordagem permite a simulação de processos de diferentes escalas, proporcionando condições de fronteira oceânicas realistas para o modelo local. Em seguida, seguiu-se uma abordagem numérica para investigar os principais factores que influenciam a dinâmica de sedimentos coesivos em um sistema estuarino composto por grandes lodaçais (estuário do Tejo, Portugal). A compreensão da dinâmica de sedimentos coesivos nos sistemas estuarinos é vital para uma gestão costeira eficaz, considerando que os sedimentos coesivos estão relacionados com vários problemas de engenharia e preocupações ambientais. A principal inovação desta tese é o desenvolvimento de um modelo morfológico que permite avaliar simultaneamente o transporte de múltiplas fracções de sedimentos (não-coesivo e coesivo) e a evolução morfológica associada. Os efeitos da mistura de sedimentos e da consolidação do leito sobre a resistência à erosão foram considerados, enquanto a coluna de fundo multicamadas permite representar a estratigrafia do fundo. O modelo morfológico foi aplicado em casos esquemáticos e em experimentos laboratoriais para avaliar seu desempenho. Em um caso de teste real, o modelo foi aplicado ao estuário do Tejo para investigar a geração realista de distribuição de sedimentos com base nas condições hidrodinâmicas locais. A aplicabilidade do modelo também foi testada sob a acção combinada de ondas e correntes. Para este efeito, o sistema de modelação MOHID foi acoplado ao modelo de ondas SWAN para simular o impacto de diferentes projectos de estruturas de defesa costeira (quebra-mares e esporões) e a formação de barras. A mesma metodologia de modelação foi aplicada a uma zona costeira (Costa da Caparica) localizada na embocadura do estuário do Tejo para avaliar a hidrodinâmica e o transporte de sedimentos em condições de águas calmas e durante eventos de ondas altamente energéticas. Os resultados destes testes confirmam o potencial do modelo para ser usado como uma ferramenta valiosa para estudos de engenharia. Palavras-chave: hidrodinâmica; morfodinâmica; transporte de sedimentos; sistemas costeiros; sistema de modelação MOHID

## Acknowledgements

Firstly, I would like to thank Prof. Ramiro Neves for the opportunity to join the MARETEC research group in 2011, and later in 2013 to accept the role of supervisor of my PhD. I want to especially thank Dr Paulo Leitão for helping with my questions about the MOHID modelling system, despite his busy work in the HIDROMOD company. I am grateful to my MARETEC colleagues that provided the support I needed to accomplish this thesis and for all these years of friendship (particularly Lúcia Pinto, Marcos Mateus, Francisco Campuzano, David Brito, Rodrigo Fernandes, Isabela Ascione, Eduardo Jauch, João Sobrinho, Hilda de Pablo, Cláudia Viegas, Guillaume Riflet, Rosa Trancão, Andreia Amaral, Carina Almeida, and Lucian Simionesei). This work was made possible due to the financial support provided by the Brazilian National Council for Scientific and Technological Development (CNPq) under the *Ciências Sem Fronteiras* program (research grant no. 237448/2012-2).

# Contents

Abstract.....	vii
Resumo .....	ix
Acknowledgements.....	x
Contents.....	xi
Chapter 1 Introduction .....	1
1.1 Background .....	1
1.2 Objectives.....	4
1.3 MOHID modelling system .....	4
1.4 Thesis Structure .....	5
Chapter 2 From regional to local scale modelling on the south-eastern Brazilian shelf: Case study of Paranaguá estuarine system.....	7
2.1 Introduction .....	8
2.2 Study Area.....	9
2.3 Previous Studies.....	10
2.4 Material and Methods .....	11
2.4.1 Numerical model.....	11
2.4.2 Model Domains.....	14
2.4.3 Numerical Simulations .....	16
2.5 Results.....	17
2.5.1 Data Analysis.....	17
2.5.2 Barotropic Model.....	18
2.5.3 Baroclinic model.....	25
2.6 Discussion.....	29
Chapter 3 Modelling of cohesive sediment dynamics in tidal estuarine systems: case study of Tagus estuary, Portugal.....	31
3.1 Introduction .....	32

3.2	Cohesive sediment dynamics.....	33
3.3	Study area .....	34
3.4	Model Setup.....	37
3.4.1	Cohesive Sediment Transport.....	38
3.4.2	Initial Conditions .....	40
3.4.3	Boundary Conditions.....	40
3.4.4	Waves.....	41
3.5	Field data.....	41
3.6	Results.....	42
3.6.1	Hydrodynamics .....	42
3.6.2	Cohesive Suspended Sediment.....	44
3.6.3	Bottom Sediment.....	49
3.7	Discussion and Conclusions .....	50
Chapter 4	Development and validation of a morphological model for multiple sediment classes ..	53
4.1	Introduction .....	54
4.2	Background .....	55
4.3	Numerical model.....	56
4.3.1	Layers description .....	56
4.3.2	Suspended sediment transport.....	58
4.3.3	Sand settling velocity .....	59
4.3.4	Mud settling velocity.....	59
4.3.5	Initiation of sediment motion .....	60
4.3.6	Bed load .....	63
4.3.7	Erosion and deposition .....	65
4.3.8	Bed evolution .....	68
4.3.9	Consolidation .....	68
4.4	Test cases .....	69
4.4.1	Steady uniform flow.....	69

4.4.2	Bed load for non-cohesive sand-mud mixtures.....	70
4.4.3	Consolidation column .....	71
4.4.4	Trench migration.....	72
4.4.5	Schematic estuary.....	76
4.4.6	Sediment distribution in the Tagus Estuary.....	77
4.5	Conclusions .....	79
Chapter 5 Modelling of sediment transport and morphological evolution under the combined action of waves and currents.....		81
5.1	Introduction .....	82
5.2	Background .....	84
5.3	Numerical model.....	84
5.3.1	Hydrodynamic module.....	85
5.3.2	Bed load transport .....	87
5.3.3	Bed slope correction .....	89
5.3.4	Model Coupling.....	90
5.4	Test Cases.....	90
5.4.1	Coastal Defence Structures.....	90
5.4.2	Detached Breakwaters.....	91
5.4.3	Groynes .....	97
5.4.4	Sandbars Formation.....	100
5.4.5	Costa da Caparica.....	103
5.5	Conclusions .....	109
Chapter 6 General Conclusions.....		111
6.1	Hydrodynamic modelling of coastal systems.....	111
6.2	Modelling of cohesive sediment dynamics in estuarine systems.....	112
6.3	Morphological modelling of coastal systems.....	112
6.4	Model validation .....	113
6.5	Future work.....	113

Bibliography .....	115
List of Figures .....	131
List of Tables .....	135

# Chapter 1 Introduction

## 1.1 Background

The growth of human populations and expansion of socioeconomic activities has increased the vulnerability of coastal systems. In particular, large industrial and urban centres have been developed around estuarine systems or bays, due to their characteristics of natural harbours. The wastewater discharges from these centres in addition to the inherent consequences of port activities, such as channels dredging, are some of the causes of significant environmental impacts. Erosion problems are also a relevant issue in coastal zones, caused by the intense natural dynamics associated with inadequate land use.

Morphological features of coastal zones depend on the sediment characteristics and the combined action of waves and currents. The bottom of estuarine systems is usually composed of a broad range of sediment particles. Muddy sediments may occur in areas where both currents and waves exert generally weak forces on the bed (e.g., tidal flats and salt marshes), while sandy sediments may be found in areas where currents and waves are more intense (e.g., channels and beaches). Wind waves are the main energy source for beaches. Particularly in the surf zone, waves may induce considerable changes in mean sea level and strong currents.

Numerical models are often used in natural sciences studies and engineering projects as powerful tools for understanding the dynamics of coastal systems and predicting the impacts of human interventions. This is particularly relevant for the study of sediment transport and morphological changes, providing essential information for an effective coastal management. The natural dynamics of coastal systems is governed by a variety of processes ranging from different temporal and spatial scales (e.g., tidal motion, wind and wave action, oceanic currents, river discharges). To simulate phenomena with different scales, models with different covered areas and grid resolutions can be nested. Following this downscaling approach, realistic boundary conditions can be provided for models of coastal systems.

The modelling of sediment transport and hydrodynamics are intrinsically related. The bathymetry changes affect the hydrodynamics which in turn modify the sediment transport. Generally, hydrodynamic models for large scales are based on the Reynolds-Averaged Navier-Stokes (RANS) equations, coupled with a turbulence-closure model (e.g.,  $k-\epsilon$ ) to compute the turbulent viscosity, assuming the hydrostatic pressure assumption. The hydrostatic pressure assumption is valid when vertical accelerations are irrelevant, which can be accepted in many practical cases, resulting in a

significant reduction in computational costs compared to fully three-dimensional (non-hydrostatic) models. Through the integration of equations along the different spatial coordinates ( $x$ ,  $y$ ,  $z$ ), the number of computational (grid) points and, consequently, the computational cost (time demand) can be reduced. However, this simplification may disregard important physical processes. Although two-dimensional depth-averaged (2DH) models are still commonly applied, the development of parallel processing and more powerful computers have enabled the applicability of three-dimensional (3D) models in coastal systems. This is an important step in order to represent the full processes involved in coastal dynamics. The alternative modelling approaches must be evaluated by modellers considering the goals and resources of a particular study.

Sediment transport can be divided into bed load (in close contact with the bed) and suspended load. To avoid the explicit inclusion of the advection-diffusion mechanism of suspended sediment, the suspended load may be inferred from the depth-integration of the product of the flow velocity and the equilibrium sediment profile (e.g. van Rijn, 1984). In this case, the equilibrium profile is inferred from a near-bed equilibrium concentration through empirical relations that depend on the bed shear stresses. Other approaches include the suspended load into a formulation for the total load that also depends on the bed shear stresses. Although these approaches can reduce computational time, the suspended load is not in equilibrium with the instantaneous bed shear stresses in unsteady flows, thus explicitly resolving the advection-diffusion equation for suspended sediment leads to more realistic transport results. This is also important when the velocity profile does not follow a logarithmic curve, as in stratified flows (e.g., in estuarine systems) or in the surf zone where three-dimensional effects (e.g., undertow) are important. Therefore, the majority of 2D and 3D models use the advection-diffusion equation with an additional settling velocity term to describe the suspended sediment transport (Garcia, 2008). Transport in suspension is more important for particles with smaller diameters. Very fine (cohesive) sediments are considered to be transported exclusively in suspension.

The mathematical equations behind numerical models are based on physical principles or empirical relations, depending on our knowledge and computational resources for representing the processes in sufficient detail. Morphological models developed for solving practical problems are normally based on simplified concepts instead of a complete mathematical description, such as the artificial partition of the sediment transport in suspended load and bed load. Thus, additional relations (often empirical) are required in such models, e.g., for the bed load transport and the near-bed equilibrium concentration. Attempts to formulate a more general mathematical model of sediment-flow interaction are based on the two-phase flow approach, in which the basic idea is to formulate

governing conservation equations for both phases (e.g., Amoudry and Liu, 2010). Although the two-phase flow approach seems promising, practical applications with this type of model are not found in the literature to date, possibly due to the computational costs involved. Moreover, the high spatial and temporal resolutions needed to satisfactorily represent some processes (e.g., consolidation) makes its complete inclusion in large-scale models infeasible, despite the well-known mathematical descriptions. Thus, simplified relations are required for considering these processes.

Previously, uniform sediment distributions were generally considered in morphological models by defining a unique fraction with a representative diameter (e.g.,  $d_{50}$ ). Thereon, sand mixtures (multiple sand fractions) have been included to represent the effects of particle interaction on erosion behaviour (hiding and exposure) and different settling velocities. Furthermore, the habitual separation between cohesive (clay, silt and organic particles) and non-cohesive (sand and gravel) sediments for modelling studies has started to be contested (van Ledden, 2003), as cohesive particles can fill the spaces between sand grains, increasing their resistance to removal (Mitchener and Torfs, 1996; Panagiotopoulos et al., 1997) and, when a bed starts to have a cohesive behaviour, even prevent bed load transport from occurring. Beyond the importance of cohesive sediments for engineering studies (e.g., siltation of marinas, harbours and navigation channels in estuarine systems), it is also relevant for water quality concerns (e.g., algae growth and contaminants transport). To study the transport of adsorbed contaminants, an important model feature is the bottom column layering capability. The consolidation of cohesive beds is an important process that increases the resistance to erosion. The sorting of sediments is easily observed in the different zones of estuarine systems, but also occur, e.g., in the different zones of beach profiles.

Reviews of hydrodynamic and sediment transport models are found in the literature (e.g., Garcia, 2008, Papanicolaou et al., 2008, Amoudry and Souza, 2011). Some of the most referenced comprehensive modelling systems are Delft 3D (Lesser et al., 2004), MIKE (Kristensen et al., 2013), ROMS (Warner et al. 2008) and TELEMAC (Villaret et al., 2013). The models basically differ in the equations for the several processes involved in sediment transport (e.g., bed load transport and erosion rate), as well as in the numerical methods (finite difference, finite element, finite volume), horizontal and vertical grid discretization (e.g., structure and non-structure). While most models consider multiple fractions of sand, few account for the simultaneous transport of non-cohesive and cohesive sediments (Le Hir et al., 2011). Other models have been developed focusing on specific problems, such as nearshore processes during storm conditions (e.g., Roelvink et al., 2009).

## 1.2 Objectives

The central aim of this thesis is to develop and test a numerical modelling approach for the study of hydrodynamics and sediment transport in coastal systems, in order to support an effective coastal management. Specific objectives are:

1. Apply a hydrodynamic model to an estuarine system through a downscaling approach from regional scale to local scale.
2. Assess the dynamics of cohesive sediments in an estuarine system following a numerical approach.
3. Develop a morphological model for multiple sediment fractions (non-cohesive and cohesive) to study sediment transport in natural systems.
4. Evaluate the morphological model performance taking into account analytic solutions, experimental and field data.

The MOHID modelling system was the main numerical tool adopted in this work. For the first and second specific objectives, this modelling system was basically applied in its previous state, with few developments performed in the scope of this thesis. The central novelty in terms of the development of the MOHID modelling system was performed to achieve the third objective. To complete the fourth objective, MOHID was coupled with the SWAN wave model to verify model results under combined action of waves and currents. The goal of this thesis encompasses the verification of a methodology replicable for diverse coastal systems. Thus, model applications for estuarine systems with different characteristics are presented, specifically the Paranaguá estuarine system (Brazil) and Tagus estuary (Portugal). The model results were validated taking into account the available data. Moreover, schematic cases and laboratory experiments were simulated to compare model results with analytic solutions and experimental data, confirming the model capacity to simulate the dynamics of cohesive and non-cohesive sediments.

## 1.3 MOHID modelling system

The origin of the MOHID modelling system goes back to 1985, with the development of a two-dimensional semi-implicit hydrodynamic model in finite differences (Neves, 1985). In the early 1990s, Prof. Ramiro Neves created a research group (MARETEC - Marine and Environmental Technology Research Centre) at Instituto Superior Técnico (Lisbon), continuing the model development in the scope of several PhD theses (e.g. Silva, 1991; Monteiro, 1995; Santos, 1995; Portela, 1996; Martins, 2000; Leitão 2003, Mateus, 2006; Riflet, 2010; Ascione, 2014; Saraiva, 2014), in addition to numerous Master theses and diverse European and international research projects performed by MARETEC and companies created by early MARETEC members (HIDROMOD and

ACTION MODULERS). The open-source philosophy and modular structure allow the collaboration of research centres and companies in favour of model development, which is continually evolving. The new developments are not restricted to the initial sphere of developers, thus researchers from other institutions may also contribute (e.g. Delpey, 2014).

At present state, the MOHID modelling system is based on the finite volume method (structure grid), allowing the use of generic vertical coordinates. The code organisation follows an object oriented strategy that permits the integration of different scales and processes. The MOHID hydrodynamic module solves the three-dimensional Navier-Stokes equations. Before this work, the sediment transport in MOHID was considered separately for non-cohesive and cohesive sediments, neglecting the interactions between different sediment fractions. The advection-diffusion mechanism for non-cohesive sediments was also previously disregarded, as well as the morphological evolution related to cohesive sediments. In the scope of this thesis, a more comprehensive approach was followed that enables the simultaneous assessment of the transport of multiple sediment fractions (non-cohesive and cohesive) and associated morphological evolution. Moreover, model formulations were updated considering the state of art and a more detailed validation was performed. A new module (Sediment) was created and other modules were adapted to include the developments of this work.

## 1.4 Thesis Structure

The structure of this thesis is based on the objectives described above. Chapter 2 presents the application of the MOHID modelling system following a downscaling methodology for the south-eastern Brazilian shelf (regional model) and Paranaguá estuarine system (local model). In Chapter 3, the main factors that influence the cohesive sediment dynamics in an estuarine system composed of large mudflats (Tagus estuary, Portugal) are investigated following a numerical approach. Chapter 4 describes the development and validation of a comprehensive morphological model aiming to predict the three-dimensional sediment transport and bed evolution in natural systems composed of different sediment types. In Chapter 5, the applicability of the developed morphological model is demonstrated in order to study sediment transport and morphological changes in coastal systems under the combined action of waves and currents. These chapters are based on previously published or submitted papers by the author during the time frame of this PhD research. The last chapter (Chapter 6) provides a general conclusion related to the accomplishment of the objectives of this thesis, as well as recommendations for future work.



## Chapter 2 From regional to local scale modelling on the south-eastern Brazilian shelf: Case study of Paranaguá estuarine system

*The material on which this chapter is based has been previously published in Franz G.A.S., Leitão P, Santos A., Juliano M., Neves R., 2016. From regional to local scale modelling on the south-eastern Brazilian shelf: case study of Paranaguá estuarine system. Brazilian Journal of Oceanography, 64(3): 277-294.*

### **Abstract**

The applicability of a numerical model following a downscaling methodology was evaluated for the south-eastern Brazilian shelf (regional model) and Paranaguá estuarine system (local model). This approach permits the simulation of different scale processes, such as storm surges and coastal upwelling, and is suitable for operational forecasting purposes. When large areas are covered by regional models, the tidal propagation inside the domain can be significantly affected by the local tidal potential, mainly where the resonance phenomenon is observed. The south-eastern Brazilian shelf is known for the resonance of the third-diurnal principal lunar tidal constituent (M3), the largest amplitudes being found in the Paranaguá estuarine system. Therefore, the significance of the local tidal potential was assessed in this study for the most important tidal constituents inside the estuarine system (including M3). The model validation was performed with tidal gauge data, Argo float profiles and satellite measurements of Sea Surface Temperature. The methodology described in this study can be replicated for other important estuarine systems located on the south-eastern Brazilian shelf. Furthermore, the numerical model was developed within a perspective of operational nowcast/forecast simulations, useful for several activities such as navigation and response to emergencies (e.g., oil spills).

Keywords: Numerical modelling, Tidal propagation, Resonance phenomenon, Downscaling, South-eastern Brazilian shelf, Paranaguá estuarine system.

## 2.1 Introduction

Coastal circulation is governed by a variety of processes on different temporal and spatial scales, including tidal motion, wind action, oceanic currents, density stratification, internal waves and fresh water discharges. These processes are affected by coastline geometry and shelf topographic features. Particularly in broad shelves, tidal motion is amplified and the response to wind action is more intense (Kantha and Clayson, 2000). Typically, depths at the shelf break are about 200 m, decreasing shoreward, while the shelf width varies between tens and hundreds of kilometres. The bottom friction in shallow depths is important in generating overtides and compound tides (Parker, 1991). When the shelf width is about one-quarter of the tidal wavelength, the phenomenon of resonance amplifies the tidal ranges (Huthnance, 1980).

The great complexity of coastal circulation can be better understood by the application of numerical models. Regional and local models can be nested to simulate processes on different spatial scales, such as storm surges generated mainly by wind action along thousands of kilometres, or the friction and influence of the coastline on the flow, which needs higher resolution numerical grids to be properly solved. Moreover, the computational domain should include both the continental shelf and continental slope to simulate coastal upwelling. This process is one of the main mechanisms behind the nutrient availability in the mixed layer, controlling phytoplankton growth. The downscaling approach was previously applied in the Tagus estuary (Portugal) to study cohesive sediment dynamics (Franz et al., 2014a) and for operational modelling of hydrodynamics and water quality (Franz et al., 2014b). From the point of view of an operational forecast system, a downscaling from regional to local models has proven successful (e.g. Maraldi et al., 2013; Bricheno et al., 2014; Mateus et al., 2012a).

The tidal forcing in regional models is usually given from global tidal atlas, defining amplitudes and phases of tidal constituents at the open boundaries, which are converted into tidal levels. However, regional models usually cover a large area, thus making it important to include the local tidal potential, mainly where the resonance phenomenon is observed (Wijeratne et al., 2012). The local potential interacts with the open boundary tidal forcing, amplifying or attenuating the tidal constituents, depending on the relative phases (Odamaki, 1989; Cummins et al., 2010; Gouillon et al., 2010).

The south-eastern Brazilian shelf is known by the resonance of the third-diurnal principal lunar tidal constituent (M3), with the largest amplitudes found in the Paranaguá estuarine system. Huthnance (1980) was the first to investigate this phenomenon with a semi-analytic model, reinforcing the theory of a damped 'organ-pipe' quarter wave resonance between the coast and the shelf edge. M3

is generated by the third-degree term in the lunar tidal potential, with a period of 8.28 h (Kantha and Clayson, 2000). Due to the usually small amplitudes, M3 is often neglected in numerical modelling studies. Nevertheless, on the south-eastern Brazilian shelf, particularly in the Paranaguá estuary, M3 is one of the most important tidal constituents.

The main goal of this paper is to evaluate the methodology of downscaling with nested models for the south-eastern Brazilian shelf (regional model) and the Paranaguá estuarine system (local model). A novelty of this study is the inclusion of M3 in the local tidal potential. To our knowledge, this is the first attempt to implement a numerical model for the Paranaguá estuarine system following a downscaling from a regional model. This approach allows the definition of realistic values of current velocities and water levels as boundary conditions, taking the effect of storm surges into consideration. When the effect of density on circulation is included (baroclinic mode), realistic values of temperature and salinity can be provided by the regional model, which is able to represent coastal upwelling.

The model was validated with tidal gauges and the significance of the local tidal potential was assessed for the most important tidal constituents, including M3. The importance of bottom friction and grid resolution for tidal propagation along the local model was also investigated. Salinity and temperature results were validated in the regional model domain with floats profiles and Sea Surface Temperature from satellite measurements, verifying the capability to properly provide open boundary conditions for the local model.

This chapter is divided into six sections. A brief description of the study area is given in Section 2.2, followed by a summary of relevant previous studies (Section 2.3). The methodology is described in Section 2.4, addressing the numerical model used, giving a definition of model domains definition and the numerical simulations performed. In Section 2.5 is presented a harmonic analysis of tidal gauges data collected to characterise the tidal propagation inside the Paranaguá estuarine system, beyond the results of the numerical simulations. A discussion of the study's findings is presented in Section 2.6.

## 2.2 Study Area

The geometry features of the south-eastern Brazilian shelf and Paranaguá estuarine system are presented in Figure 2.1. This estuarine system has a surface area of 552 km<sup>2</sup> (without wetlands), 25% of which corresponds to a tidal flat region. The wetlands (mangroves and salt marshes) around the system cover an area of 296 km<sup>2</sup> (Noernberg et al., 2006). It is interconnected to the Cananéia-Iguape estuarine system by a narrow channel. Three inlet channels connect the Paranaguá estuarine

system directly to the shelf sea. The two main channels are located around an Island (Ilha do Mel) at the system's mouth. These channels follow different predominant directions in the two main branches. A narrower branch lies in the east-west direction (Paranaguá bay), with an extension of about 40 km from the mouth. A broader branch lies in the north-south direction (Laranjeiras bay), with an extension of about 30 km from the mouth. The third and least important inlet channel is between two islands (Ilha das Peças and Ilha de Superagüi), connected to the central part of Laranjeiras bay.

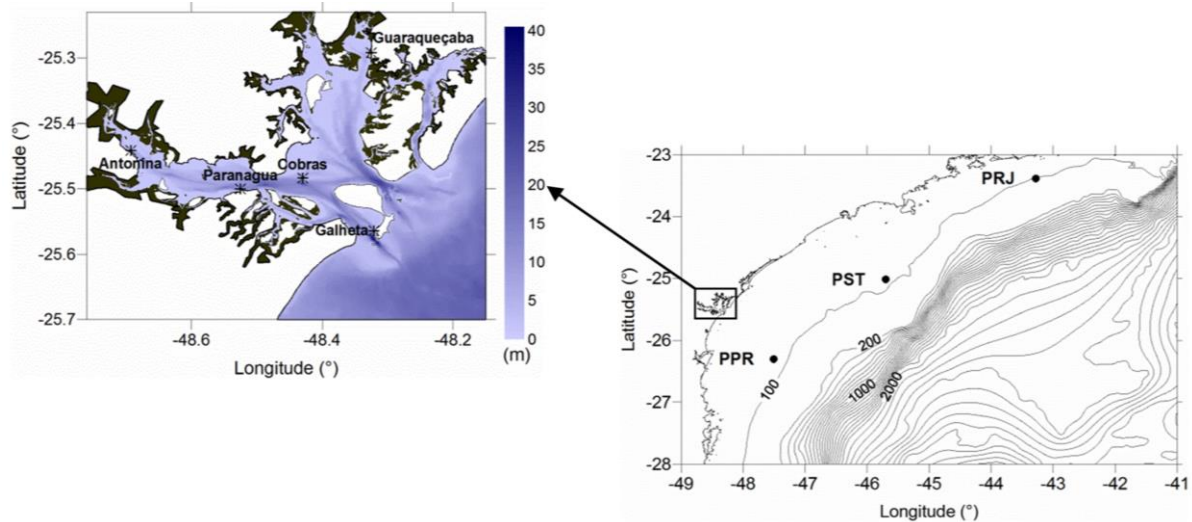


Figure 2.1 – Geometry features of the south-eastern Brazilian shelf (right) and Paranaguá estuarine system (left) with wetlands, showing the tidal gauges sites used for model validation.

The wind over the south-eastern Brazilian shelf is driven by the South Atlantic Convergence Zone (SACZ), with predominant winds in the north-easterly direction, especially in summer. During the winter, the passages of cold fronts are more frequent, significantly changing the wind direction. The circulation at the shelf edge is dominated by the Brazil current (southward), leading to a strong eddy activity in the south-eastern Brazilian shelf. The Brazil current also induces shelf break upwelling, which is reinforced by wind-driven upwelling in the summer (Campos et al., 1995; Campos et al., 2000). Furthermore, internal waves are generated over the shelf break and slope (Pereira and Castro, 2007; Pereira et al., 2007).

### 2.3 Previous Studies

In the late 1970s, oceanographic and meteorological data on the south-eastern Brazilian shelf were measured by the University of São Paulo. The water level and currents at three sites on the shelf (PPR, PST and PRJ in Figure 1) were used to define amplitudes, phases and current ellipses of the nine most important tidal constituents (Q1, O1, P1, K1, N2, M2, S2, K2, M3), as described by

Mesquita and Harari (2003). The extension of the water level record used in the harmonic analysis varied between 12.9 and 31.2 days, with sampling intervals of 15 minutes. Harari and Camargo (1994) used these amplitudes and phases to determine, through linear interpolation, the boundary conditions for a coastal hydrodynamic numerical model (three-dimensional, but barotropic). Following this approach, they were able to draw cotidal charts and surface current ellipses for the main tidal constituents.

In another study, Camargo and Harari (1994) considered wind and pressure fields in the same model to address storm surges in extreme events. At the open boundary, the water level oscillations caused by storm surges were defined proportionally to corresponding observations on coastal tidal gauges. Although this approach has led to satisfactory results in hindcast simulations, it is impracticable in operational modelling systems that are intended to produce forecasts. Furthermore, the model's results showed constraints in the representation of tidal amplitude and phase in the southern part of the shelf, mainly in neap tides and in the mouth of the Paranaguá estuarine system. The three high and low tides observed daily in neap tides were not properly represented by the model. This fact was explained as being due to the lack of non-linear tidal constituents in the model.

Camargo and Harari (2003) used the cotidal amplitude and phase maps from Harari and Camargo (1994) to implement a three-dimensional hydrodynamic model with a horizontal resolution of about 1 km for the Paranaguá estuarine system and neighbouring coast, taking three non-linear tidal constituents into consideration in the simulations (M4, MN4, MS4). Due to the small area covered, the model only reproduced 10 % of the storm surge observed. This constraint can be overcome by coupling the local model to a larger scale model, which is one of the justifications for adopting a downscaling approach.

## 2.4 Material and Methods

### 2.4.1 Numerical model

This study was based on the application of the MOHID water modelling system (Leitão et al., 2008). The hydrodynamic module is the core of MOHID. It is a three-dimensional model that solves the full Navier-Stokes equations, on the basis of the Boussinesq and hydrostatic approximations. The equations are solved numerically using the finite volumes method, with a generic vertical discretization that allows simultaneous implementation of various types of vertical coordinates. MOHID is coupled to GOTM (Global Ocean Turbulence Model), which consists of a set of turbulence-closure models (Buchard et al., 1999; Villarreal et al., 2005).

The open boundary tidal forcing for the hydrodynamic model was defined from FES2012 (Finite Element Solution) tidal atlas (Lefèvre et al., 2002; Lyard et al., 2006; Carrère et al., 2012), which includes 32 tidal constituents distributed on  $1/16^\circ$  grids (amplitude and phase). Other smaller constituents were considered by tidal admittance. The choice of FES2012 was mainly based on the inclusion of the M3 tidal constituent. Furthermore, FES2012 has a better resolution and several more non-linear constituents than the previous version FES2004, which is a great improvement for coastal areas. Normally, the compound tides generated by non-linear effects in shallow waters are rapidly dissipated. A well-known exception is the M4 propagation from the Patagonian shelf towards the Brazilian coast (Pairaud et al., 2008). The tide was propagated into the nested domains using the Flather (1976) radiation scheme, which radiates external gravitational waves over the perturbation produced by other forcing mechanisms, such as the wind and the Coriolis force.

The local tidal potential was included as a force added to the momentum equation. This local forcing interacts with the tidal propagation from the open boundary, which can amplify or attenuate the tidal constituents' amplitude and change their phase (Gouillon et al., 2010). In shelf seas where resonance occurs, as observed in the south-eastern Brazilian shelf for the M3 tidal constituent, the local tidal potential can greatly affect the tide (Wijeratne et al., 2012). MOHID was developed to take into account the second degree tidal potential for the most important long period (Mf, Mm, Ssa), diurnal (K1, O1, P1, Q1) and semidiurnal (M2, S2, N2, K2) tidal constituents, following the method described by Kantha and Clayson (2000). The third-degree tidal potential is usually neglected due to its small contribution. In this study, it was considered so as to take into account the local tidal potential of M3.

The tidal potential level ( $m$ ) is defined as the sum of several terms corresponding to different tidal constituents:

$$\xi(\phi, \theta, t) = \sum_{n=2}^3 \sum_{m=0}^n \sum_j f_j A_j L_m(\theta) \cos(m\phi + \omega_j t + u_j) \quad (2.1)$$

where  $n$  is the degree,  $m$  is the frequency bands (long period, diurnal, semidiurnal, third-diurnal),  $j$  is the specific tidal constituent,  $\phi$  is the longitude,  $\theta$  is the latitude,  $f$  is the elasticity factor,  $t$  is the universal time,  $A$  is the equilibrium tide amplitude,  $\omega$  is the frequency, and  $u$  is the Dodson number, calculated on the basis of Dodson's arguments with an extra term to adjust the phase. For M3, this term involves an additional  $180^\circ$  in the phase (Pugh and Woodworth, 2014). The coefficient  $L_m$  is obtained from the normalized Legendre functions:

$$\begin{aligned}
L_0(\theta) &= \frac{3}{2} \cos^2 \theta - 1 \\
L_1(\theta) &= \sin 2\theta \\
L_2(\theta) &= \cos^2 \theta \\
L_3(\theta) &= \cos^3 \theta
\end{aligned} \tag{2.2}$$

The bottom shear stress ( $\vec{\tau}_b$ ) is calculated using a quadratic formulation and assuming a logarithmic velocity profile (law of the wall):

$$\begin{aligned}
\vec{\tau}_b &= \rho C_D \vec{u}_b |\vec{u}_b| \\
C_D &= \left[ k / \ln \left( \frac{z + z_0}{z_0} \right) \right]^2
\end{aligned} \tag{2.3}$$

where  $\rho$  is the water density,  $C_D$  is the drag coefficient,  $\vec{u}_b$  is the horizontal velocity at the centre of the bottom grid cell,  $k$  is the von Karman's constant (0.4),  $z$  is equal to half of the thickness of the bottom grid cell and  $z_0$  is the bottom roughness length.

A relaxation scheme was implemented in MOHID to avoid the divergence of model's results from a reference solution. In keeping with this approach, a term is added to the equation that defines the property evolution:

$$P^{t+\Delta t} = P^* + (P^{ext} - P^*) \frac{\Delta t}{T_d} \tag{2.4}$$

where  $P$  is a generic property (e.g. velocity components, salinity and temperature),  $P^*$  the property result calculated by the model,  $P^{ext}$  the value of the property in the reference solution,  $\Delta t$  the model time step and  $T_d$  the decay time. The relaxation scheme can be applied as an open boundary condition by assuming a decay time that increases gradually from the boundary to infinity in the inner domain (after a defined number of cells) (see Martinsen and Engedahl, 1987; Engedahl, 1995).

Fields of water level, velocity, temperature and salinity of the MyOcean model (<http://www.myocean.eu/>) were used to constrain the boundary condition via the relaxation scheme in a ten-cell band. The decay time for water level and velocity components was assumed as  $10^5$  s (approximately one day) at the boundary cells and  $10^9$  s inside the domain (after ten cells). The large decay time inside the domain was defined so as to omit the relaxation of the hydrodynamic properties, thus allowing for the tidal propagation and wind action. For the water properties salinity and temperature, the decay time inside the domain was defined as  $3 \times 10^5$  s (approximately three days) to relax the model's results to correspond to the MyOcean solution. Previous simulations have shown that for long period simulations (months) the model results of temperature at the surface

tend to diverge from satellite images measurements when relaxation is not considered. This divergence is probably due to minor errors from different sources (e.g. atmospheric boundary conditions), which after long period simulations can exercise great influence on the model's results.

The atmospheric boundary conditions were provided by the Global Forecast System (GFS) reanalysis (<http://www.emc.ncep.noaa.gov/index.php?branch=GFS>), with  $0.5^\circ$  resolution and 3-hour frequency. The water level oscillations caused by atmospheric pressure fluctuations were estimated on the open boundary based on the inverted barometer effect (Kantha et al., 1994; Canas et al., 2009).

#### 2.4.2 Model Domains

The model was implemented by using a multi-nesting approach and software (Automatic Running Tool) developed at MARETEC that allows automatic simulations within a nowcast/forecast perspective (Ascione et al., 2014; Franz et al., 2014b). Initially, three domains were nested in an online one-way for modelling the Brazilian south-eastern shelf (regional model). Then two other domains were nested in an offline way to study the propagation of the tides into Paranaguá estuarine system (local model). The areas encompassed by each domain are presented in Figure 2.2.

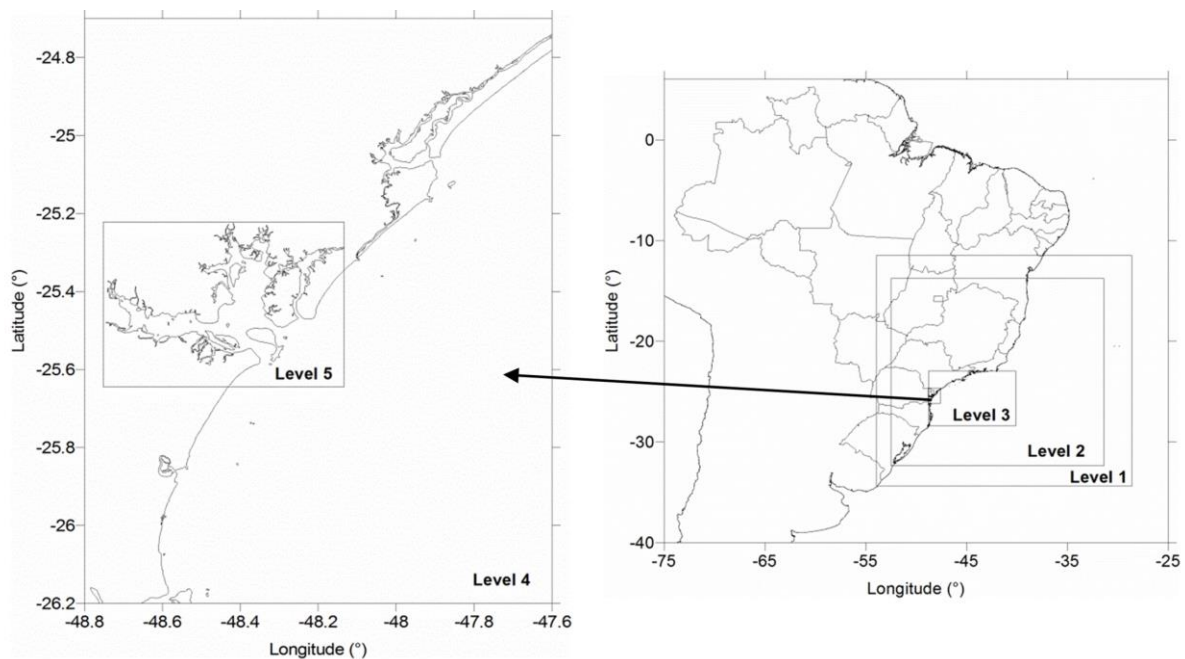


Figure 2.2 – Area covered by the local (left) and regional (right) scale models

The tide levels generated from FES2012 tidal constituents, as well as the water level oscillations caused by the atmospheric pressure, were imposed on the open boundary points of Level 1, while results of MyOcean were imposed in Level 2 for the simulations in baroclinic mode. For the offline

nesting, a spatial window was set in the regional model (Level 3) to save the results every 900 s to provide open boundary conditions for the subsequent nested domain (Level 4), which covers the entire Paraná state coast. Adopting a similar approach, the results of Level 4 were used as open boundary conditions for Level 5, which covers only the Paranaguá estuarine system. The flows of the main rivers (Cachoeira, Nhundiaquara, Tagaçaba, Guaraqueçaba) were defined in Level 5 as constant, based on average values from monitored data (<http://hidroweb.ana.gov.br/>), giving a total flow of  $70 \text{ m}^3\text{s}^{-1}$ .

The bathymetries of the regional model were generated from the GEBCO One Minute Grid, version 2.0 ([www.gebco.net](http://www.gebco.net)). For the local model, the bathymetries were generated by using digitalized nautical charts of the Brazilian Navy. The intertidal zones in the Paranaguá estuary were obtained from Landsat satellite images and included in Level 5 bathymetry with a constant depth of 0.2 m. MOHID is able to represent the intertidal zones by a wetting/drying scheme, as described by Martins et al. (2001). A minimum depth of 0.1 m was defined in this study, below which the cells are considered uncovered. In each time step, the uncovered cells are tracked by the model in order to impose null fluxes of mass and momentum, avoiding numerical instabilities.

Excepting the bi-dimensional domain (Level 1), the vertical discretization of the nested domains adopted the same approach, with Cartesian layers overlapped by Sigma layers. Cartesian layers are suitable in transition zones between the deep ocean and shelf seas, avoiding the generation of artificial currents along the shelf slope, whereas Sigma layers are suitable in shallow and intertidal zones where the flow tends to follow the bathymetry. Level 2 consists of 42 Cartesian layers overlapped by 7 Sigma layers. The number of Cartesian layers decreases in other domains, depending on the maximum depth. The vertical resolution of Cartesian layers was the same as in MyOcean, which minimises errors in the linear interpolation of the MyOcean solution to the MOHID grid, in order to define initial and boundary conditions. The vertical resolution at the surface was about 1 m. The turbulence-closure model  $k-\epsilon$  was used in this study for the calculation of vertical mixing, while the horizontal viscosity coefficients were defined as a function of the grid resolution (characteristic length of non-resolved vortices). The bottom roughness length ( $z_0$ ) was defined as 2.5 mm uniformly. Details about the domains are given in Table 2.1.

Table 2.1 – Features of the domains

Name	Horizontal Cells	Horizontal Resolution	Vertical Layers	Vertical Resolution	Maximum Depth
Level 1	191 x 211	12 km	1	-	5902 m
Level 2	156 x 177	12 km	49	447 m – 1 m	5503 m
Level 3	182 x 288	3 km	47	421 m – 1 m	4552 m
Level 4	132 x 175	600 m	18	7 m – 1 m	50 m
Level 5	385 x 540	120 m	16	5 m – 1 m	38 m

### 2.4.3 Numerical Simulations

The reference year for the simulations performed in this study was 2013. The numerical simulations are described next.

#### Barotropic Model

Firstly, the regional and local models were run in barotropic mode to assess the tidal propagation. Harmonic analysis of the water level results was performed making use of the MATLAB T\_Tide package (Pawlowicz et al., 2002). The main harmonic constituents obtained from the regional model results were compared with those presented in Mesquita and Harari (2003) for three sites on the south-eastern Brazilian shelf (PPR, PST, PRJ in Figure 2.1). For the local model, the main harmonic constituents were compared with those derived from the data analysis of five tidal gauges located in the Paranaguá estuarine system (Figure 2.1), described in section 2.5.1 for Galheta, Paranaguá and Antonina and presented in Camargo and Harari (2003) for Ilha das Cobras and Guaraqueçaba.

The FES2012 solution was also used for purposes of comparison with the regional model's results, as it assimilated altimetry data and can be considered a reliable reference (at least in deep waters). Even though the open boundary tidal forcing was provided by FES2012, this comparison gives further insights into tidal propagation, as the tide is modified along the model domain by other processes (e.g. internal tidal potential and bottom friction), and can be useful to explain some differences between the model's results and tidal gauges data, which could come from the boundary conditions.

The regional model was run for 183 days, considered as a reasonable period for the harmonic analysis of the model's results, taking into account that it is longer than the time required for the separation of S2 and K2 constituents (Foreman, 1996). After the validation of the regional model, the results of the local model (Level 4) were evaluated. Scenarios ignoring the local tidal potential and bottom friction were performed to verify their effects on tidal propagation. Thereafter, Level 5 was run, assessing the effect of increasing grid resolution on model results. Due to the computational time required, the simulations with the local model were run for a shorter period (31 days), and the

inference technique (Pawlowicz et al., 2002) was used to compute the amplitude and phase of K2 inferred from S2, considering the relative differences obtained from tidal gauges data in each location.

A warm-up period of one day was considered for the model simulations, when the water level at the open boundary was gradually imposed until it reached real amplitudes, avoiding numerical instabilities. The results were analysed only after this period. For the scenario in which the local tidal potential was neglected, the regional model was previously run again without considering this force, giving rise to new boundary conditions for the local model.

### **Baroclinic Model**

In a second stage of the study, the regional model was run in baroclinic mode to verify whether it can accurately represent the water density stratification and provide adequate boundary conditions of temperature and salinity for the local model. The results in summer and winter months were validated using Argo floats profiles of temperature and salinity ([www.argo.ucsd.edu](http://www.argo.ucsd.edu)) and Sea Surface Temperature (SST) from satellite microwave sensors produced by Remote Sensing Systems ([www.remss.com](http://www.remss.com)) and sponsored by National Oceanographic Partnership Program (NOPP). The baroclinic model was initialized with MyOcean fields of temperature and salinity. Similarly to the tide level, a warm-up period of one day was considered for the baroclinic force.

## **2.5 Results**

### **2.5.1 Data Analysis**

Data of three tidal gauges (Galheta, Paranaguá, Antonina) provided by the Brazilian Navy was used to characterise the tidal propagation along the narrower branch of the Paranaguá estuarine system, through harmonic analysis using the MATLAB T\_Tide package (Pawlowicz et al., 2002). The most extensive data series period in each tidal gauge was considered, according to Table 2.2. The sum of the amplitudes and relative importance of the main long period (6), diurnal (21), semi-diurnal (19), third-diurnal (5), quarter-diurnal (7) and other shallow water (10) constituents are presented in Table 2.3. The significance of third-diurnal and quarter-diurnal constituents is noticeable. M3 contributes with about 40% of the total third-diurnal constituents' amplitude, while M4 contributes with about 46% of the total quarter-diurnal constituents' amplitude.

Table 2.2 – Coordinates and data series period of the tidal gauges

	<b>Lat</b>	<b>Lon</b>	<b>Initial Date</b>	<b>End Date</b>	<b>Days</b>
<b>Galheta</b>	25° 34'.0 S	48° 19'.0 W	09/05/2001	28/02/2005	1392
<b>Paranaguá</b>	25° 30'.1 S	48° 31'.5 W	01/01/1997	31/12/1999	1095
<b>Antonina</b>	25° 27'.3 S	48° 40'.7 W	02/06/2001	21/06/2002	385

Table 2.3 – Sum of the amplitudes (m) and relative importance of the main tidal constituents in different frequency bands

	<b>Galheta</b>		<b>Paranaguá</b>		<b>Antonina</b>	
<b>Long Period</b>	0.10	6%	0.13	5%	0.25	8%
<b>Diurnal</b>	0.27	17%	0.31	13%	0.36	12%
<b>Semi-diurnal</b>	0.86	53%	1.17	50%	1.45	48%
<b>Third-diurnal</b>	0.19	12%	0.36	15%	0.44	14%
<b>Quarter-diurnal</b>	0.16	10%	0.35	15%	0.49	16%
<b>Others</b>	0.03	2%	0.03	1%	0.06	2%
<b>Total</b>	<b>1.62</b>	<b>100%</b>	<b>2.36</b>	<b>100%</b>	<b>3.05</b>	<b>100%</b>

The importance of storm surges in the Paranaguá estuarine system was verified for the tidal gauges and periods presented in Table 2.2. The hourly data series was subtracted from the water level prediction made for the same period by using T\_Tide package, allowing for the assessment of the maximum positive and negative oscillations caused by storm surges in Galheta (0.88 m and -1.09 m), Paranaguá (1.63 m and -0.83 m) and Antonina (1.26 m and -1.32 m). The oscillations range is of the same order of magnitude as that of the tide.

## 2.5.2 Barotropic Model

### Regional model

Amplitude charts for M2, S2 and M3 from the regional model's results (Level 2) are presented in Figure 2.3, as well as the differences with respect to the FES2012 solution. The amplitude differences from FES2012 are generally smaller than 1 cm. In shallow waters, the M2 amplitudes in model's results tend to be higher than FES2012. A remarkable amplification of M3 is observed along the shelf in the direction of the Paranaguá estuarine system, presenting larger amplitudes (about twice) than FES2012.

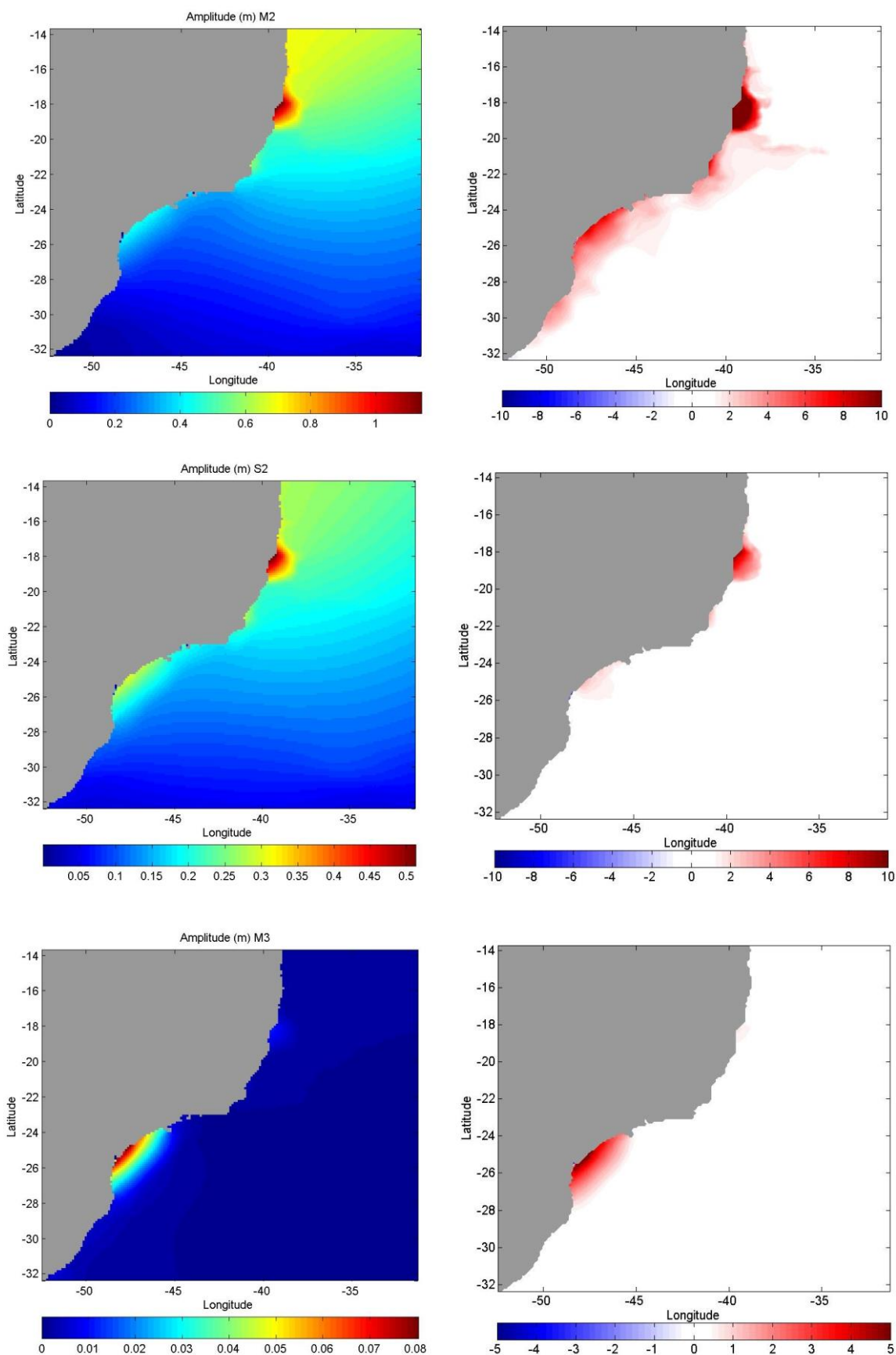


Figure 2.3 – Amplitudes (m) of M2, S2 and M3 tidal constituents from model results (left) and differences (cm) from FES2012 tidal solution (right)

Figure 2.4 shows amplitudes and phases from model results and data of the three most important diurnal (O1, K1, Q1) and semidiurnal (M2, S2, N2) tidal constituents, besides M3, at three sites on the south-eastern Brazilian shelf (PPR, PST, PRJ). In addition, data from FES2012 were included as a reference. The M2 constituent presented larger amplitudes (4 – 8 cm) than observed in the data, even in the FES2012 solution (1 – 5 cm), suggesting that these differences arose in part thanks to the boundary conditions. However, the M2 amplitudes obtained from the local model results (shown in next section) agreed well with the data analysis of tidal gauges inside the estuarine system, probably due to the increase in the resolution of the nested grids.

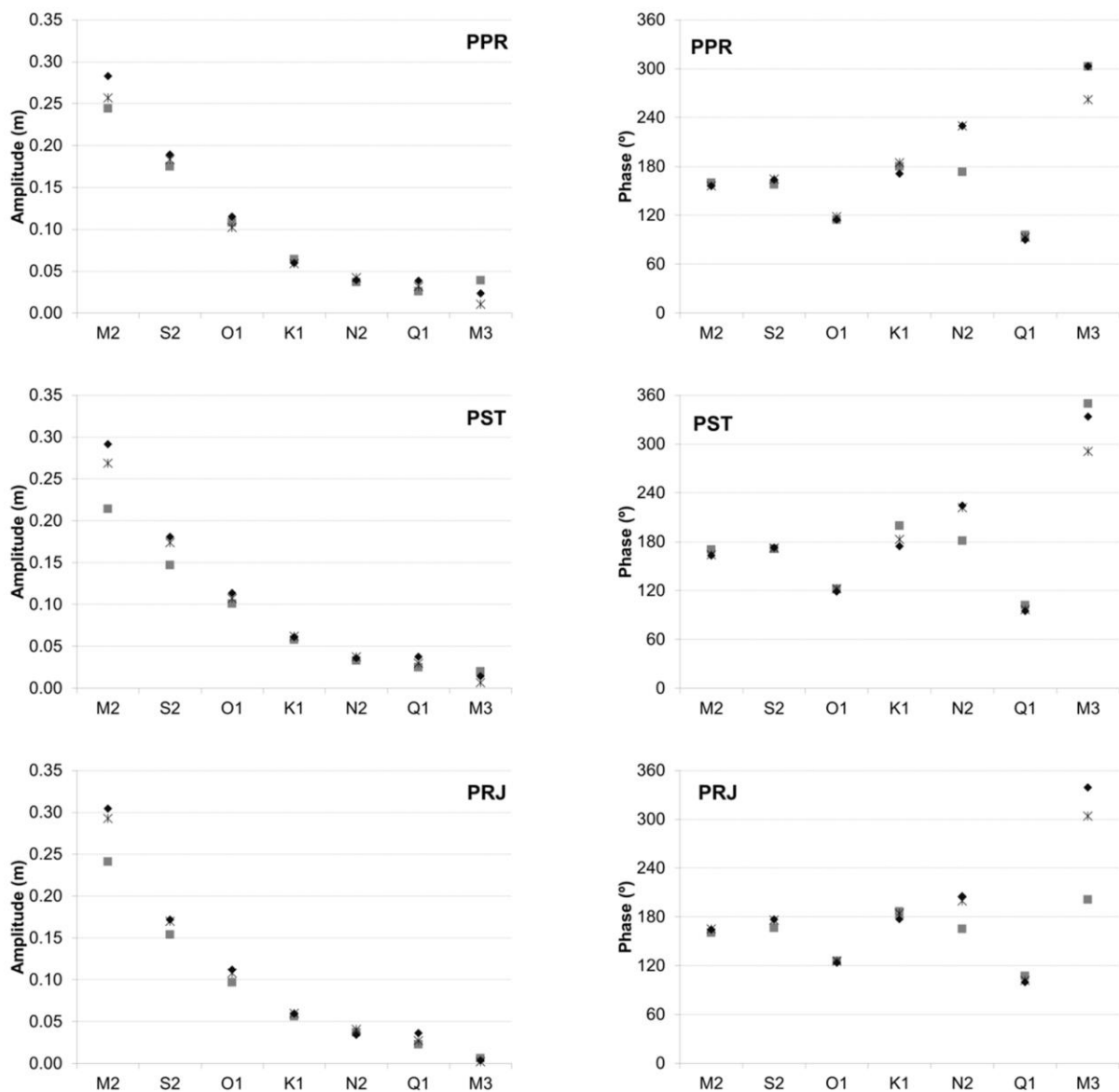


Figure 2.4 – Amplitudes and phases of the three most important diurnal and semidiurnal tidal constituents on the south-eastern Brazilian shelf. ■ Data \*Fes2012 ♦ Model

The model's results for S2 amplitudes are slightly higher than data's (1 – 3 cm), as well as those of FES2012. A similar pattern is observed for N2 phases, which showed the largest phase differences between the constituents analysed (40° - 56°); with the exception of M3 in PRJ, where phase data differ greatly both from those of other stations and FES2012. M3 amplitudes from the model's results at these three sites are in general twice the value of FES2012, decreasing the relative differences of the data. M3 phases are well represented by the model, mainly at the site where M3 is more prominent (PPR). The relative differences for amplitude and absolute differences for phase between model's results and tidal gauge data on the shelf are presented in Table 2.4.

Table 2.4 – Relative differences for amplitude (%) and absolute differences for phase (°) between model's results and tidal gauge data on the shelf

<b>Tidal Gauges</b>	<b>M2</b>	<b>S2</b>	<b>O1</b>	<b>K1</b>	<b>N2</b>	<b>Q1</b>	<b>M3</b>
<b>PPR</b>	15.9%	7.9%	6.5%	-7.0%	6.2%	47.7%	-40.0%
	-3.7°	6.0°	-0.1°	-8.5°	56.3°	-5.7°	0.6°
<b>PST</b>	36.1%	22.9%	12.5%	5.0%	9.1%	49.6%	-28.0%
	-7.2°	1.6°	-3.3°	-24.9°	43.2°	-6.9°	-15.9°
<b>PRJ</b>	26.3%	11.6%	15.4%	6.4%	-7.0%	57.8%	-40.0%
	3.9°	10.4°	-1.9°	-9.6°	40.2°	-7.4°	137.6°

### **Local model**

The six most important tidal constituents observed in five tidal gauges located in the Paranaguá estuarine system (Figure 2.1) were investigated for the scenarios described in section 2.4.3. Figure 2.5 shows the results of amplitudes and phases compared with data. According to the amplitudes obtained from the tidal gauges data, the M3 constituent is among the fifth most important at the estuary mouth (Galheta) and is the third most important in the intermediate zone (Ilha das Cobras), with higher amplitudes than all the diurnal constituents. In the upper parts of the estuarine system, the amplitudes of overtides and compound tides become larger, due to an increase in the importance of the nonlinear terms in the momentum and continuity equations. The first overtide of M2 (M4) is the third most important constituent in Antonina and Guaraqueçaba, whereas the MS4 constituent, a compound tide of M2 and S2, becomes the sixth most important. The importance of the local tidal potential and bottom friction for tidal propagation is clearly observed by comparing the reference scenario with the scenarios that neglected these forces. The differences observed between the reference scenario and others scenarios are less significant for the diurnal constituents, showing a weaker influence from the bottom friction and local tidal potential.

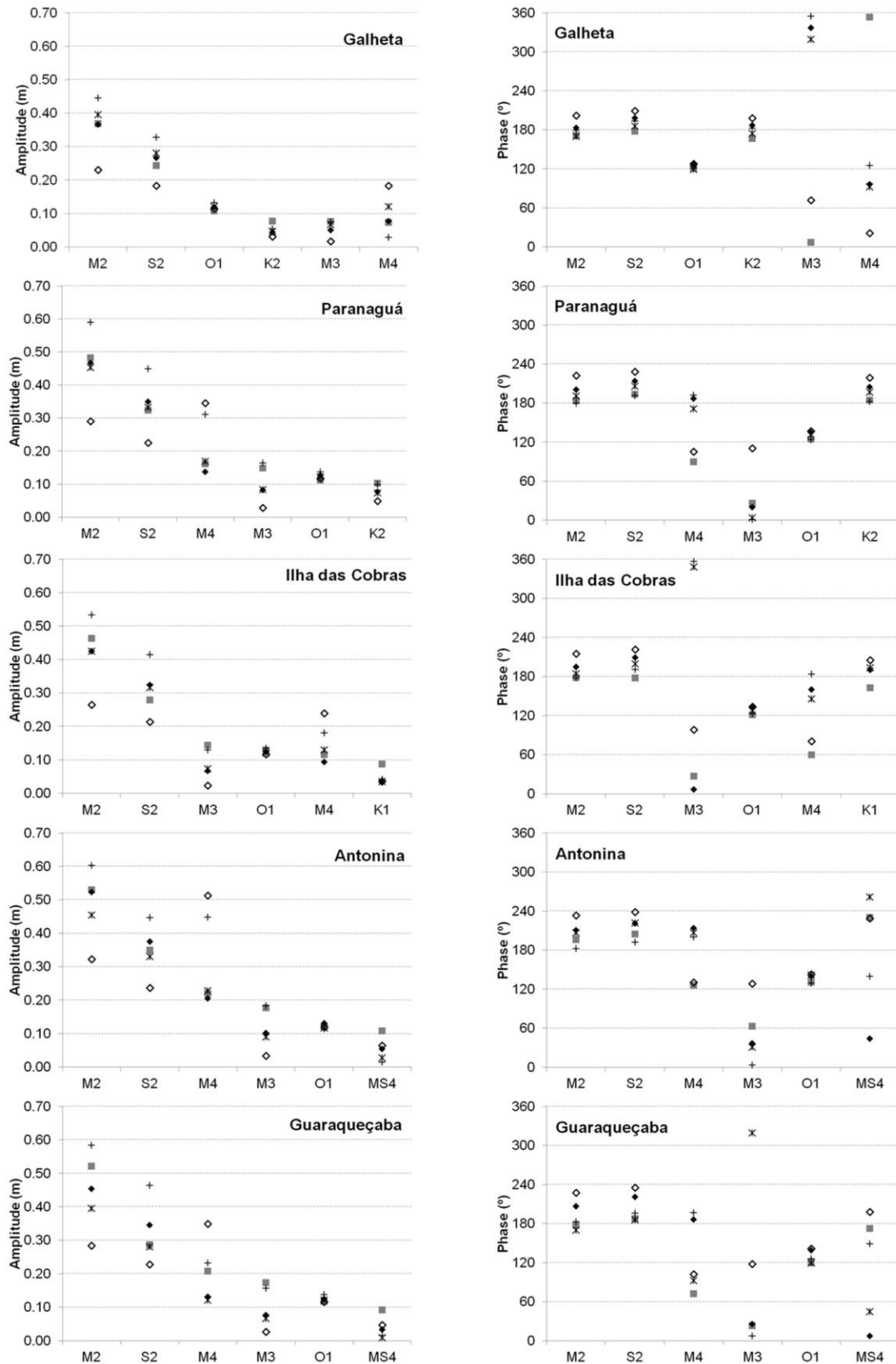


Figure 2.5 – Amplitudes and phases of the most important tidal constituents in the tidal gauges located at Paranaguá estuary. ■ Data ♦ Reference (rugosity  $2.5 \times 10^{-3}$  m) + Without friction (rugosity  $1.0 \times 10^{-11}$  m) ◇ Without local tidal potential \* Enhanced grid resolution (Level 5)

The relative differences for amplitude and absolute differences for phase between the different scenarios and tidal gauge data are presented in Table 2.5, taking the five most important constituents in the Paranaguá estuarine system into consideration. The results confirmed the importance of the local tidal potential in the proper simulation of the tidal propagation in local models through downscaling from a large scale domain. M2, S2 and M3 presented significantly smaller amplitudes when compared with data and the reference scenario, which means that the local tidal potential interacts positively with the open boundary tidal forcing, amplifying these constituents. The opposite was ascertained for M4, with attenuated amplitudes. As M4 is not generated from the tidal potential, the differences observed in its amplitudes and phases are derived from differences obtained in M2 when the local tidal potential is ignored. The results suggest that the M4 wave propagated from the open boundary conditions interacts negatively with the M4 generated locally when the local tidal potential of M2 is taken into account.

M3 amplitudes become 30% to 40% closer to data in the reference scenario than in the scenario that ignores the local tidal potential. However, a relative error of between -34% and -56% is still found. These errors are in the same order of magnitude (-40%) as that found in the tidal gauges on the shelf shown in Table 2.4, indicating that they arose outside the estuarine system in the regional model. A considerable improvement when considering the local tidal potential was also observed in tidal phase, especially for M3. The exception was M4, which presented better phase results for the scenario without this force.

As expected, the scenario in which the bottom friction was ignored presented higher amplitudes for the linear constituents than did the reference scenario. The nonlinear M4 constituent also presented higher amplitudes in this scenario (Galheta is the only exception). Thus, it may be stated that the nonlinear friction term in the momentum equation is not greatly important for M4 generation along the Paranaguá estuarine system. This is in agreement with other studies that attributed greater importance to the nonlinear continuity term for M4. On the other hand, the bottom friction is important for the MS4 constituent, increasing its amplitudes two times in Guaraqueçaba and four times in Antonina.

M3 amplitudes show a better fit with data in the scenario ignoring bottom friction than in the reference scenario, with differences of the order of 1 cm. However, the other most important constituents, namely M2, S2 and M4, presented much larger differences in amplitudes. This means that M3 amplitudes in the model cannot be fitted to data by only adjusting the bottom roughness length, as the other constituents would be overestimated. Thus, the error might arise from other sources, such as the open boundary conditions from FES2012.

Table 2.5 – Relative differences for amplitude (%) and absolute differences for phase (°) between the different scenarios and tidal gauge data inside the Paranaguá estuarine system

Tidal Gauge	Scenario	M2	S2	M4	M3	O1
Galheta	Reference	-0.7%	9.6%	6.3%	-34.2%	11.1%
		12.2°	20.4°	103.2°	-29.3°	6.1°
	Without Local Tidal Potential	-37.4%	-24.7%	151.8%	-76.8%	6.3%
		30.7°	31.6°	28.2°	65.2°	7.1°
	Without Friction	20.9%	34.5%	-61.3%	-2.8%	22.4%
	7.8°	15.4°	131.7°	-12.1°	-0.2°	
	Enhanced Grid Resolution	7.4%	15.3%	66.2%	-12.6%	12.2%
		-0.9°	7.7°	99.4°	-47.2°	-1.5°
Paranaguá	Reference	-3.1%	8.2%	-15.2%	-45.2%	14.1%
		17.0°	20.6°	97.7°	-6.3°	10.6°
	Without Local Tidal Potential	-39.9%	-30.4%	113.9%	-81.1%	5.8%
		38.6°	34.8°	16.1°	84.6°	12.9°
	Without Friction	22.3%	38.8%	92.3%	9.8%	22.8%
	-4.4°	-1.7°	102.9°	-25.2°	-0.6°	
	Enhanced Grid Resolution	-6.0%	2.9%	4.8%	-44.3%	9.2%
		7.3°	12.7°	81.9°	-22.5°	6.7°
Ilha das Cobras	Reference	-8.4%	16.2%	-18.6%	-53.8%	-4.2%
		16.5°	31.5°	100.5°	-20.4°	10.8°
	Without Local Tidal Potential	-42.8%	-23.3%	108.9%	-83.8%	-10.2%
		36.7°	43.9°	21.1°	71.2°	12.3°
	Without Friction	15.0%	48.9%	57.5%	-10.2%	3.5%
	-0.8°	13.4°	123.8°	-30.0°	1.3°	
	Enhanced Grid Resolution	-8.4%	13.3%	12.3%	-49.1%	-6.8%
		5.9°	21.9°	86.0°	-38.4°	6.0°
Antonina	Reference	-1.2%	7.6%	-7.0%	-42.6%	9.0%
		14.0°	17.0°	88.2°	-26.2°	8.8°
	Without Local Tidal Potential	-39.2%	-32.2%	133.0%	-80.8%	-0.2%
		36.8°	34.6°	4.5°	65.5°	12.4°
	Without Friction	13.7%	27.8%	103.2%	3.6%	-4.5%
	-14.2°	-12.4°	74.3°	-59.4°	-1.5°	
	Enhanced Grid Resolution	-14.2%	-5.3%	3.8%	-49.0%	-2.7%
		10.0°	17.1°	80.7°	-31.9°	11.2°
Guaraqueçaba	Reference	-12.8%	20.4%	-36.7%	-55.8%	6.1%
		29.0°	33.6°	114.4°	2.7°	18.6°
	Without Local Tidal Potential	-45.3%	-20.4%	68.2%	-84.7%	-1.4%
		49.6°	48.0°	30.3°	95.6°	21.5°
	Without Friction	12.2%	61.8%	11.8%	-9.4%	16.4%
	5.4°	9.0°	124.5°	-15.2°	5.9°	
	Enhanced Grid Resolution	-24.0%	-2.1%	-41.8%	-61.4%	2.6%
		-7.7°	-1.8°	20.7°	-63.2°	-0.8°

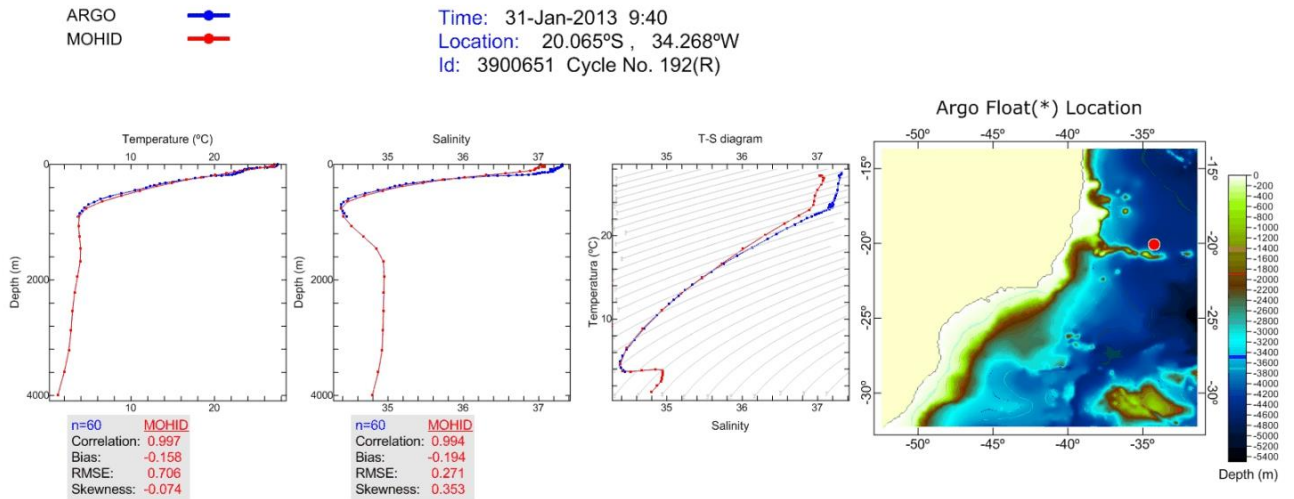
The improvement in grid resolution from 600 m to 120 m (Level 5) presented the largest differences from the reference scenario in the upper zones (Antonina and Guaraqueçaba), where the amplitudes of the main constituents (M2 and S2) decreased significantly. This outcome may be explained by the inclusion of the intertidal zones in Level 5, which enlarged the area for tidal propagation. The amplitudes can be adjusted in the future by considering a drag coefficient for water flow in mangroves zones. However, an improvement was obtained in M2 and S2 phases in the Laranjeiras bay (Guaraqueçaba). This effect may be a consequence of a better characterization of estuarine channels. The mean absolute error of amplitudes and phases for the different scenarios is presented in Table 2.6.

Table 2.6 – Mean absolute error of amplitudes (cm) and phases (°) for the five most important tidal constituents

		<b>Scenario</b>	<b>M2</b>	<b>S2</b>	<b>M4</b>	<b>M3</b>	<b>O1</b>
<b>Mean Absolute Error</b>	Reference		2.6	3.6	2.8	6.9	1.0
			17.7°	24.6°	100.8°	17.0°	11.0°
	Without Local Tidal Potential		19.4	7.9	17.1	11.8	0.6
			38.5°	38.6°	20.0°	76.4°	13.2°
	Without Friction		7.8	12.4	10.2	1.1	1.6
			6.5°	10.4°	111.4°	28.4°	1.9°
	Enhanced Grid Resolution		5.9	2.2	3.3	6.8	0.8
			6.4°	12.2°	73.7°	40.6°	5.2°

### 2.5.3 Baroclinic model

The validation of salinity and temperature in the regional model domain (Level 2), with Argo floats profiles, is shown in Figure 2.6 and Figure 2.7 for a summer and winter period, respectively. For instance, comparisons between profiles measured by individual floats and simulated by the model at the same location are shown, besides the T-S diagram that identifies the different water masses. The density stratification was adequately simulated by the model. Statistics for a 30-day period in summer and winter considering all the Argo floats are also shown, with Pearson's correlation coefficient very close to 1 and, in general, a small Bias and RMSE for both temperature and salinity.



MOHID vs Argo floats Total floats for Temperature: 42 Run\_1: 02-Jan-2013 to 31-Jan-2013  
 Total floats for Salinity: 41

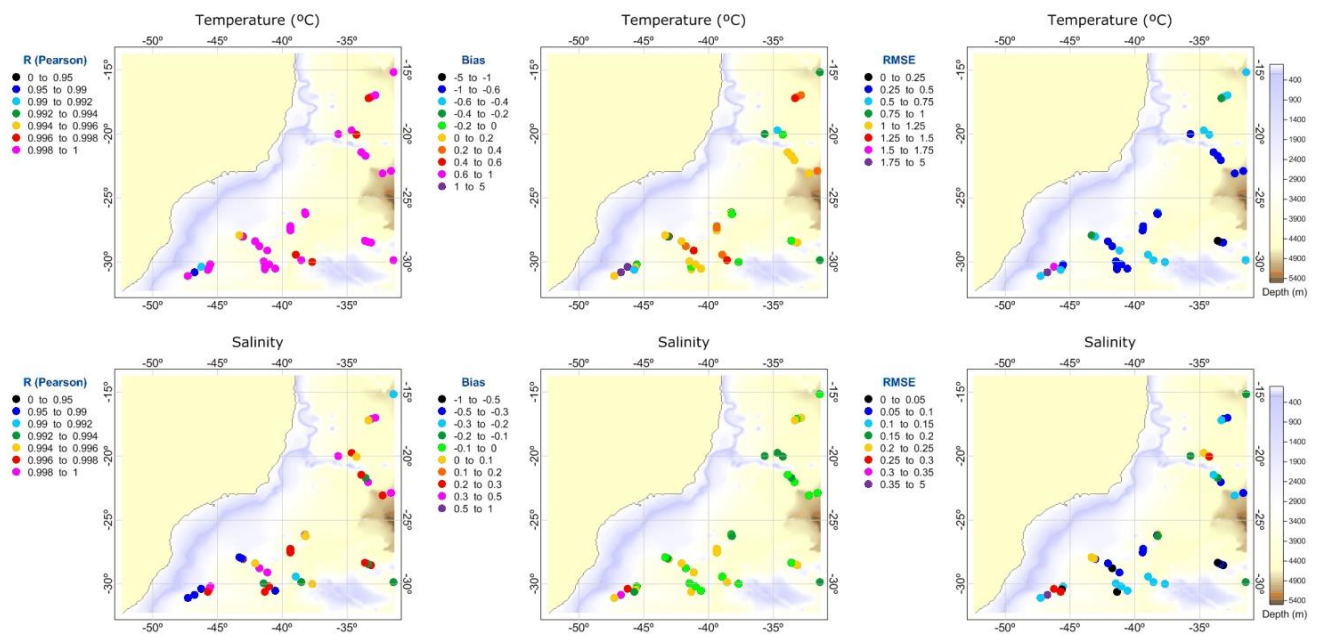


Figure 2.6 – Salinity and temperature results compared with Argo floats profiles in summer (above). Statistics between results and Argo floats profiles in January 2013 (below).

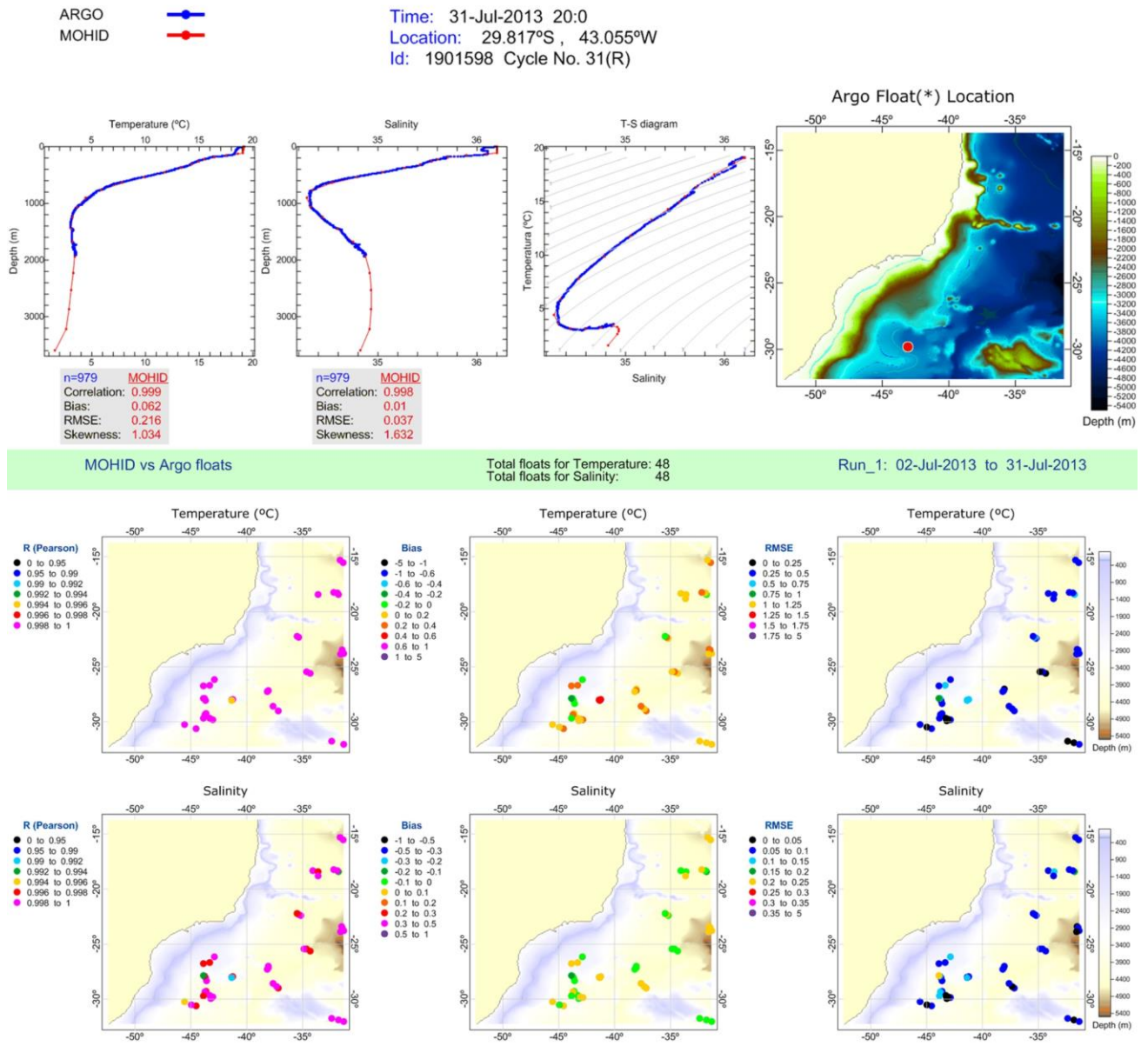


Figure 2.7 – Salinity and temperature results compared with Argo floats profiles in winter (above). Statistics between results and Argo floats profiles in July 2013 (below).

SST results are compared with satellite measurements in Figure 2.8. It is possible to observe the southward heat transport due to the Brazil current, which is also responsible for upwelling along the shelf break. The strong flows from Rio de la Plata also influence the temperatures observed near the coast in the southern part of the domain. Figure 2.9 shows the validation performed for 30 days in summer (January) and winter (July), with generally strong correlation and small Bias and RMS. The major differences in relation to measurements were found near the coast, possibly due to the lack of interaction between the shelf sea and estuarine systems in the regional model.

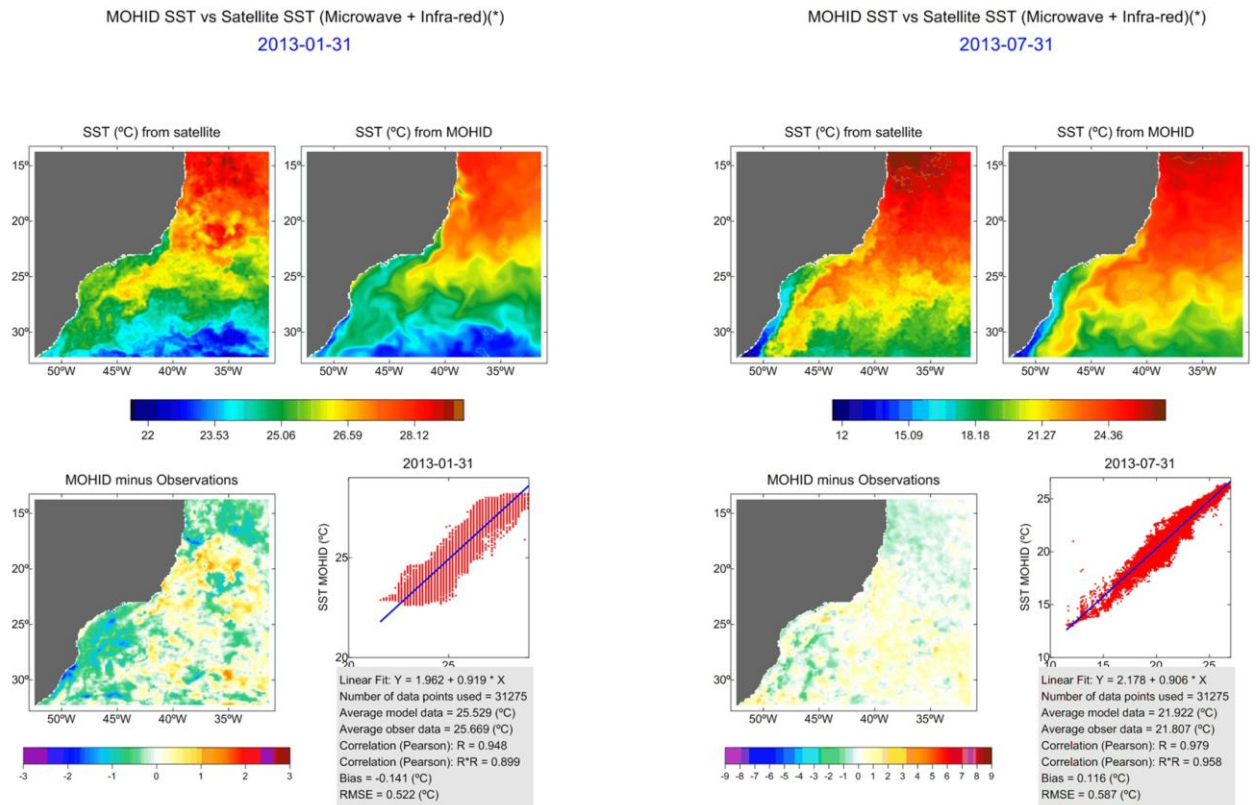


Figure 2.8 – SST (°C) results compared with satellite measurements in summer (left) and in winter (right).

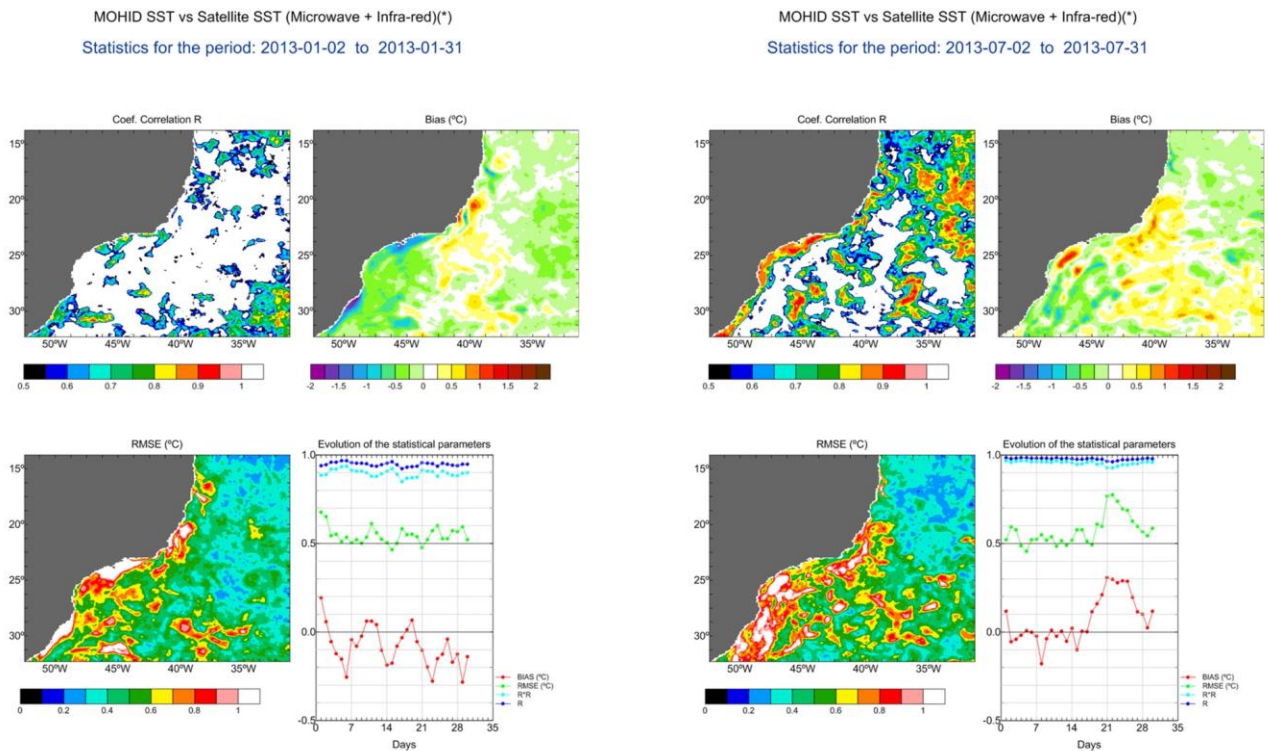


Figure 2.9 – Statistics between SST (°C) results and satellite measurements in January 2013 (left) and July 2013 (right).

## 2.6 Discussion

We demonstrated that the methodology of downscaling with nested models is applicable to the south-eastern Brazilian shelf and the Paranaguá estuarine system, representing an important progress compared to previous studies (e.g. Camargo and Harari, 2003). The results confirmed the importance of the local tidal potential to properly simulate the tidal propagation in local models, following a downscaling from a large scale domain. The validation of temperature and salinity with Argo floats profiles, as well as SST with satellite measurements, indicated that the regional model can represent the patterns observed on south-eastern Brazilian shelf, such as the upwelling process caused by the Brazil current. Thus, the regional model is capable of providing adequate boundary conditions for the local model.

The inclusion of the M3 term in the local tidal potential contributed significantly for a better representation of its amplitudes and phases in the model domain. This outcome agrees with the conclusions of other modelling studies in areas where tidal resonance is observed (e.g. Wijeratne et al., 2012). Taking 100 m as an average depth for the shelf, the wavelength for M3 is approximately 933 km. When the shelf width is about one-quarter of the wavelength (233 km for M3), resonance phenomena may occur. This condition is satisfied in the broader parts of the south-eastern Brazilian shelf. The M3 resonance is also seen in the Great Australian Bight.

The differences between the harmonic constituents found in model results and data arose in part because of the open boundary tidal forcing. The constant development of a more accurate global tidal atlas will contribute to a further improvement in the model results of tidal propagation. Future studies are needed to validate water temperature and salinity in the Paranaguá estuarine system, which depends on a representative set of local data's becoming available. Furthermore, the results of the local model can be used to provide boundary conditions for the regional model in a two-way nesting, allowing an improvement in the results of water temperature and salinity near the coast. The simulation of storm surges also needs to be addressed in future studies, in view of the importance of these events for the water level oscillations observed in this estuarine system, found to be of the same order of magnitude as the tide amplitude.

The methodology described in this study can be replicated for other important estuarine systems, such as Guanabara Bay and Santos Bay, located on the south-eastern Brazilian shelf, by using the results of the same regional model as open boundary conditions. The numerical model developed for the Paranaguá estuarine system with a high grid resolution (120 m) can be used for the investigation of important questions, such as the transport of sediments and water quality. Furthermore, the model was developed with a view to future nowcast/forecast simulations, useful

for several activities, such as navigation and response to emergencies (e.g., oil spills). Two harbours are located in the Paranaguá estuarine system (those of Paranaguá and Antonina); the harbour of Paranaguá is one of the most important Brazilian harbours in terms of financial turnover.

Finally, we have confirmed that the application of a numerical modelling system adopting a downscaling approach is capable of simulating processes of different spatial scale on the south-eastern Brazilian shelf, providing accurate boundary conditions to the Paranaguá estuarine system. This thus represents a valuable tool and significant progress for modelling studies in this area.

# Chapter 3 Modelling of cohesive sediment dynamics in tidal estuarine systems: case study of Tagus estuary, Portugal

*The material on which this chapter is based has been previously published in Franz, G., Pinto, L., Ascione, I., Mateus, M., Fernandes, R., Leitão, P., Neves, R., 2014. Modelling of cohesive sediment dynamics in tidal estuary systems: case study of Tagus estuary, Portugal. Estuarine, Coastal and Shelf Science 151, 34-44.*

## **Abstract**

Cohesive sediment dynamics in estuarine systems is a major issue in water quality and engineering problems. Numerical models can help to assess the complex dynamics of cohesive sediments, integrating the information collected in monitoring studies. Following a numerical approach, we investigated the main factors that influence the cohesive sediment dynamics in an estuarine system composed of large mudflats (Tagus estuary, Portugal). After a spin up period of the bottom layer and considering the combined effect of waves and currents on the bottom shear stress, the dynamics of cohesive sediment during the fortnightly and daily erosion-sedimentation cycle was properly reproduced by the model. The results of cohesive suspended sediments were validated with data from sixteen monitoring stations located along the estuary and turbidity data measured by two multiparametric probes. The hydrodynamics were previously validated by harmonic analysis and with ADCP data. Although tidal currents are the major cause of cohesive sediment erosion, the results suggest that wind waves also play an important role. The simulated sediment mass involved in the fortnightly tidal cycle was in the same order of magnitude of the annual load from the rivers, as observed in previous studies based on field data.

Keywords: modelling; hydrodynamics; cohesive sediments; estuarine dynamics; Portugal, Tagus estuary

### 3.1 Introduction

Cohesive sediments (CS) are a concern for water quality in coastal areas, estuaries, and lagoons since many contaminants and pollutants can be absorbed onto sediments. Furthermore, the turbidity caused by suspended sediments reduces light penetration in the water, affecting photosynthesis and food availability. CS also represents a concern to engineering problems, such as siltation of harbours and marinas, as well as dredging in navigation channels. CS consist of fine inorganic (clays, silts and very fine sands) and organic particles (e.g. detritus) (Hayter and Mehta, 1986). They differ from non-cohesive sediments (sands, gravels and pebbles) by the importance of electrochemical forces acting between the particles, that cause the flocculation and consolidation processes.

CS dynamics in estuarine systems depends on different forcing as currents, waves and river flows. Numerical models can be a useful tool to understand the complex factors that affect CS dynamics. The Tagus estuary is the main estuarine system in Portugal and one of the largest European estuaries, characterised by large mudflats. Previous CS modelling studies in this system were mainly focused on model implementation and sensitivity analyses (e.g. Portela and Neves, 1994; Barros, 1996; Portela, 1997; Vaz et al., 2011). In these studies, the effect of waves in the CS resuspension was neglected and the lack of field data compromised a reliable model validation. This lack of knowledge motivated our attempt to carry out a more comprehensive cohesive sediment modelling study in the Tagus estuary, including the verification of the wave effects on sediment resuspension and a reliable validation of model results. The MOHID water modelling system can be used in the study of CS dynamics (Cancino and Neves, 1999a, b). However, recent applications of the MOHID system for the Tagus estuary showed the need to improve the model setup to increase the cohesive suspended sediment (CSS) concentrations, mainly in periods of low river flow.

In order to investigate the main factors that influence the CS dynamics in estuarine systems and to develop a consistent methodology for modelling studies, this chapter addresses the following research questions: (1) What is the contribution of the CS mass available at the bottom and the CS mass input from the rivers for the CSS concentrations? (2) What is the significance of the tidal currents and wind waves for CS dynamics?

To answer these questions, different scenarios were carried out with the MOHID model applied to the Tagus estuary and considering 2012 as the reference year, the driest year observed in the last decade. First, a method to calculate the combined effect of waves and currents on the bottom shear stress was implemented in the MOHID model code. To assess the wave effect on sediment erosion two scenarios were considered (with and without waves). The importance of the sources of sediment to CSS concentrations was addressed considering a scenario with a properly CS bottom

mass spin up versus a scenario with a null CS bottom mass. Furthermore, the annual CSS load from the Tagus river was calculated and compared with the mass involved in the Tagus estuary fortnightly erosion-sedimentation cycle. The deposition zones were analysed, as well as the CS flux exported from the estuary to the ocean.

This chapter is divided into seven sections. A briefly general description of the CS dynamics, mainly in estuarine systems, is given in Section 3.2. In Section 3.3 the Tagus estuary is described, focusing on the hydrodynamics and sediment dynamics. In Section 3.4 the model setup is discussed, describing the downscaling approach with nested grids, the formulations and simplifications assumed in the CS dynamics simulations, and the initial and boundary conditions adopted. The field data used to validate the model is described in Section 3.5. In Section 3.6 the hydrodynamics and CSS validation are presented, beyond the results of the scenarios carried out to answer the research questions. In Section 3.7 the model results are discussed in the light of the scientific literature and the research questions are addressed, approaching the main factors affecting the CS dynamics and the findings achieved that can be used in future modelling studies.

## 3.2 Cohesive sediment dynamics

CS dynamics is influenced by currents, waves and inputs from the watershed. In a tidal estuarine system, currents are mainly generated by tides, carrying CSS upstream during flood tide and downstream during ebb tide. The maximum sediment deposition occurs in the slack period when the velocity intensities and, consequently, the bottom shear stress are smaller. The maximum sediment erosion occurs in the transition between high and low tides when velocities are higher (van Rijn, 2012).

In estuarine systems, the concentration of suspended sediments depends on the fortnightly tidal cycle, due to the differences in velocity peaks observed in spring and neap tides. Furthermore, in spring tides the water reaches the intertidal areas that are usually dry in neap tides, allowing the erosion of deposited sediments. The wave action also contributes to an increase in the bottom shear stress and can be sufficient to cause erosion. The waves can reach different parts of the intertidal zone depending on the tidal cycle, remobilizing the CS trapped in low velocities areas (Whitehouse et al., 2000).

CS are transported in suspension primarily as flocculated material (Droppo, 2001). The collision between particles coupled with the cohesion mechanisms are the essential forces of flocculation (Krone, 1962). Since the size of the sediment flocs is much larger than the size of individual particles, flocculation significantly increases the suspended sediment settling velocity (Migniot, 1968).

Individual particle sizes, suspended sediment concentrations, water turbulence and salinity are the main parameters affecting the flocculation. The effect of salinity on sediment flocculation was demonstrated in laboratory tests (Krone, 1962; Migniot, 1968; Portela et al., 2013). However, *in situ* measurements do not reveal any marked effect of salinity on sediment flocculation (Burt, 1984; Puls and Kuehl, 1986; van Leussen, 1988; Hamm and Migniot, 1994). Soulsby et al. (2013) based on a large data-set of floc size and settling velocity from *in situ* measurements of Northern European estuaries assumed that the effect of particles mineralogy, biological content and water salinity can be neglected when compared with the effects of turbulence and suspended sediment concentration.

High suspended sediment concentrations increase the probability of collisions between the particles and the formation of flocs, resulting in higher settling velocity. However, at sediment concentrations higher than  $20 \text{ kg m}^{-3}$  the settling velocity decreases. At these high concentrations, which occur near the bottom, the suspended sediments become a fluid mud, with a viscosity several hundred times larger than that of clear water (Whitehouse et al., 2000). The upward flux of water expelled from the fluid mud reduces the settling velocity of the flocs, which is referred to as hindered settling (Hayter and Metha, 1986). Deposited flocs are compacted under the effect of gravity, increasing particle cohesion and resistance to erosion. This process, called consolidation, includes stages at different time scales (from days to years) depending on the sediment density. A medium consolidated stage (1 month) has a wet density between  $1150\text{-}1250 \text{ kg m}^{-3}$  and it is still sailable for ships. A highly consolidated stage occurs only after 1 year with a wet density between  $1250\text{-}1350 \text{ kg m}^{-3}$  (van Rijn, 2012). Clays are responsible for the overall cohesion – 5-10% of clay minerals (by dry weight) in the bottom sediments induce the cohesiveness behaviour (Raudkivi, 1990). This behaviour does not allow the bed load transport of cohesive sediments, as occurs for non-cohesive sediments (van Ledden, 2003).

### 3.3 Study area

The Tagus estuary (Figure 3.1) is one of the largest estuaries in Europe, with a total area of approximately  $368 \text{ km}^2$  and an average volume of around  $2700 \text{ hm}^3$ , delimited according to the Water Framework Directive (WFD) (2000/60/EC). The width varies between 2 km in the estuary channel and 17 km in the upper zone, and the average and maximum depths are about 5 m and 40 m, respectively. The tidal propagation distance in the Tagus estuary is approximately 80 km. The intertidal zone occupies a total area of  $146 \text{ km}^2$ , mainly composed of tidal flats (64%) and salt marshes (13%) (Nogueira et al., 2012). The tidal flats are composed of a clay percentage larger than 10%, which gives cohesive characteristics to the sediments (Freire, 2003). Caçador and Duarte (2012)

based on sediments collected at two sampling sites in the Tagus estuary found that silt and clay were the main constituents of the estuary salt marshes, with sand accounting for less than 5%.

The most complete study on tidal propagation inside the Tagus estuary was carried out by the Portuguese Hydrographic Institute (Lemos, 1972), based on water level measurements at 16 stations over a period of several months. The tidal components extracted by harmonic analyses from these measurements are the main information used to characterise tidal propagation inside the estuary. The semidiurnal tidal components generated by the gravitational attraction of the moon (M2) and sun (S2) are the most important, with an amplitude of 1.16 m and 0.41 m at Lisbon, respectively, producing two tidal cycles per day. The 25 minutes difference between the M2 and S2 periods (12h25min and 12h, respectively) is responsible for the fortnightly spring/neap tidal cycle. The Tagus estuary is classified as mesotidal, with an average tidal height between 2.0 m in the mouth and 2.6 m in the upper zone, varying between 1.0 m in neap tides and 4.0 m in spring tides.

The main studies on the Tagus estuary hydrodynamics were performed in the context of PhD theses (e.g. Portela, 1996; Martins, 2000; Leitão, 2003; Neves, 2010) and were discussed in scientific papers (Âmbar e Backhaus, 1983; Vale and Sundby, 1987; Barros, 1996; Fortunato et al., 1997, 1999; Jouanneau et al., 1998; Valente and Silva 2009; Vaz et al., 2009; Canas et al., 2009; Dias et al., 2013). The tide is the main mechanism forcing the flow in the estuary, determining current directions and water level variations. The average tidal prism is about  $600 \times 10^6 \text{ m}^3$  and the average freshwater volume entering the estuary during a tidal cycle is typically 2% of the tidal prism. The tide is amplified inside the estuary as a consequence of depth reduction and high current velocities. In the upper estuary, the tide amplitude is reduced due to friction. The ebb tides are longer than floods in the upper zones but shorter near the estuary mouth, because of the relative importance of inertial and friction effects. The maximum velocities are reported in the mouth, with  $2 \text{ m s}^{-1}$  in the spring tides ebb. In the intermediate estuary and main channels, the maximum velocities are approximately  $1 \text{ m s}^{-1}$ , decreasing in the shallower upper estuary. As a consequence of high velocities, the distance travelled by a particle during a flood or ebb tide is about 15 km.

The wind plays a secondary role in the Tagus estuary hydrodynamics, although it can be important for contaminant transport at the water surface. The wind effect is proportional to the length of its action line, referred to as “fetch”. In the Tagus estuary, the dominant wind is from the NW and the fetch can reach 20 km in the upper estuary zones. Wind waves have high frequency and small amplitudes inside the estuary, but can increase the turbulence and trigger fine sediment resuspension in shallow zones.

The Tagus river is the estuary's main freshwater source, with an annual average flow of about  $300 \text{ m}^3 \text{ s}^{-1}$ , according to data from an upstream hydrometric station (Almourol) for the period between 1973 and 2012 (<http://snirh.apambiente.pt>). The estuary stratification is strongly related to the river flow and tidal cycle. The estuary is well mixed in spring tides and low river flow, but it can be stratified under high river flow.

Several studies have inferred the importance of light limitation in the phytoplankton productivity due to high suspended sediment concentrations in this nutrient rich system (e.g. Gameiro et al., 2007, 2011). Thus, it is fundamental to consider the CS dynamics in ecological modelling studies, as the phytoplankton growth depends on the availability of light in the water (Mateus and Neves, 2008; Vaz et al., 2011; Mateus et al., 2012b). CS are also important to other environmental and economic issues in the Tagus estuary. In recent years, an important case of siltation involving cohesive sediments was documented in a marina located in the Tagus estuary (Bettencourt et al., 2011; Portela et al., 2013). Furthermore, heavy metals and other contaminants adsorbed on CS tend to accumulate in the salt marshes of the Tagus estuary (Vale, 1990; Salgueiro and Caçador, 2007; Duarte et al., 2008, 2010; Caçador et al., 2009; Caçador and Duarte, 2012).

According to Vale and Sundby (1987), the amount of sediment involved in the Tagus estuary fortnightly erosion-sedimentation cycle corresponds to a full year's input of suspended sediment during ordinary flow conditions. The estimated suspended sediment mass varied between  $0.27 \times 10^5 \text{ t}$  at neap tides and  $3.9 \times 10^5 \text{ t}$  at spring tides, while the Tagus river annual average load was  $4 \times 10^5 \text{ t}$ . However, a suspended sediment load from the Tagus river of  $1 \times 10^6 \text{ t}$  was estimated over a 10-day period in the 1979 catastrophic flood (Vale, 1981). Vale and Sundby (1987), based on measurements along the estuary, showed that the maximum turbidity zone was absent at neap tides, but at spring tides covered nearly the entire estuary. Maximum concentrations were always found in the upper estuary. Through remote sensing data analysis from the Modis-Aqua satellite, Valente and Silva (2009) showed that the turbidity plume from the Tagus river was visible at spring tides and less visible at neap tides.

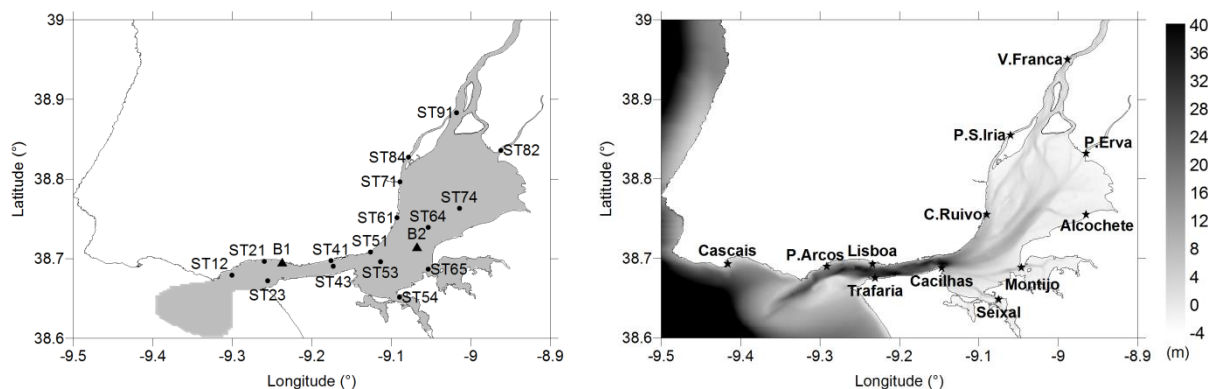


Figure 3.1- Tagus estuary area according to the WFD (2000/60/EC) (darker area) and the location of the monitoring stations (left). Bathymetry (m) of the Tagus estuary relative to the hydrographic zero (2.08 meters below the mean sea level in Cascais). Negative depths represent the intertidal zones that can be above water in low tides. Locations of the tide gauges used to verify the model results are also shown (right).

### 3.4 Model Setup

To perform this study the MOHID water modelling system (Leitão et al., 2008) was used. The Tagus estuary model was implemented by using a downscaling approach, described by Mateus et al. (2012b). Three domains were nested in an online one-way to properly represent the tidal forcing at the ocean boundary. The first domain has a grid resolution of  $0.06^\circ$ , covering the entire West Iberia coast ( $33.5^\circ$  N –  $49.9^\circ$  N,  $1.0^\circ$  W –  $13.5^\circ$  W). This domain was forced only with the FES2004 (Finite Element Solution) tidal atlas (Lefèvre et al., 2002; Lyard et al., 2006), considering the fourteen most important harmonic constituents. The second domain was used to smooth down the changes between grid resolution of the first and third domains, minimising numerical instabilities. This domain has a grid resolution of  $0.02^\circ$ , covering part of the Portuguese coast ( $36.0^\circ$  N –  $39.9^\circ$  N,  $8.5^\circ$  W –  $10.5^\circ$  W). The bathymetries of these first two domains were generated from the ETOPO 2' database (<http://www.ngdc.noaa.gov/mgg/global/etopo2.html>). The last domain includes the Tagus estuary and part of the nearest coast ( $38.5^\circ$  N –  $39.1^\circ$  N,  $8.7^\circ$  W –  $9.6^\circ$  W) and has a variable resolution, with  $0.002^\circ$  (200 m) inside the estuary. The bathymetry was generated by using data collected during several bathymetric surveys and provided by the Portuguese Hydrographic Institute (Figure 3.1).

In order to assess the model performance in extreme conditions, a very dry year (2012) was chosen for the simulations. An extensive validation of the model results was possible due to the large set of monitored data available in 2012, including 6 months data from two automatic stations installed in the estuary. The locations of the tide gauges and monitoring stations used in this study are presented in Figure 3.1. The model spin up was performed by simulating the reference year several times until the results reached the observed average CSS concentrations. Two scenarios were

simulated to verify the differences in the CS dynamics, one taking account of the action of the waves and the other one without doing so.

Due to the low river inflow during 2012, the estuary was well mixed through most of the year and a vertically integrated model can be used to represent the system in this conditions. This approach enabled running a long period with a reasonable computational cost. The MOHID executable used for the simulations was built with OpenMP (Open Multi-Processing) directives and the simulations were carried out using a computer with 6 cores, which enabled running a 1- year simulation period in approximately 2 days.

### 3.4.1 Cohesive Sediment Transport

The MOHID system assumes that the transport of cohesive sediment occurs only in suspension. Thus, the transport depends only on the advection-diffusion equation, with a settling velocity included in the vertical advection. The settling velocity  $W_s$  ( $\text{ms}^{-1}$ ) is calculated considering the effect of sediment concentration  $C$  ( $\text{kg m}^{-3}$ ) on flocculation and the hindered settling effect above a concentration  $C_{HS}$  (of about  $20 \text{ kg m}^{-3}$ ), based on the formulation proposed by Nicholson and O'Connor (1986):

$$\begin{aligned} W_s &= K_1 C^m \text{ for } C < C_{HS} \\ W_s &= K_1 C_{HS}^m [1.0 - K_2 (C - C_{HS})]^{m_1} \text{ for } C > C_{HS} \end{aligned} \quad (3.1)$$

where  $K_1$  ( $\text{m}^4 \text{kg}^{-1} \text{s}^{-1}$ ) and  $K_2$  ( $\text{m}^3 \text{kg}^{-1}$ ) depend on sediment mineralogy and the exponents  $m$  and  $m_1$  depend on particle size and shape. Mehta (1986) and van Rijn (1993) suggested values for  $m$  in the range between 1 and 2. Nicholson and O'Connor (1986) determined the following values for the parameters:  $K_1=0.006$  ( $\text{m}^4 \text{kg}^{-1} \text{s}^{-1}$ ),  $K_2=0.01$  ( $\text{m}^3 \text{kg}^{-1}$ ),  $m=1$  and  $m_1=5$ . The exponent  $m_1$  is usually taken as 4.65 for small particles, based on Dyer (1986).

The CSS is considered a conservative property, consequently, the total mass in the model domain can change only due to river inputs, fluxes across the bottom and fluxes to the ocean. The exchange between the water column and the bottom is calculated with the Partheniades' erosion formula (Partheniades, 1965) described in Eq. 3.2 and Krone's deposition formula (Krone, 1962) described in Eq. 3.3.

$$\begin{aligned} \frac{\partial M_E}{\partial t} &= E \left( \frac{\tau}{\tau_E} - 1 \right) \text{ for } \tau > \tau_E \\ \frac{\partial M_E}{\partial t} &= 0 \text{ for } \tau < \tau_E \end{aligned} \quad (3.2)$$

$$\begin{aligned}\frac{\partial M_D}{\partial t} &= CW_s \left(1 - \frac{\tau}{\tau_D}\right) \text{ for } \tau < \tau_D \\ \frac{\partial M_D}{\partial t} &= 0 \text{ for } \tau > \tau_D\end{aligned}\quad (3.3)$$

where  $\tau$  is the bed shear stress ( $\text{Nm}^{-2}$ ),  $\tau_E$  is a critical shear stress for erosion ( $\text{Nm}^{-2}$ ),  $E$  is the erosion rate ( $\text{kg m}^{-2}\text{s}^{-1}$ ) and  $\tau_D$  is the critical stress for deposition ( $\text{Nm}^{-2}$ ).

The CS are eroded when the bottom shear stress exceeds a critical value for erosion, but are deposited when the bottom shear stress falls below a critical shear stress for deposition. Freire (2003) determined in a laboratory experiment the critical values of erosion and deposition for bottom CS based on samples collected in the Tagus estuary intertidal zone. For shear stresses above  $0.4 \text{ Nm}^{-2}$ , the CS was eroded and the deposition was more important for shear stresses below  $0.2 \text{ Nm}^{-2}$ . The erosion rate is usually taken as  $5 \times 10^{-5} \text{ (kg m}^{-2}\text{s}^{-1})$  based on Mulder and Udink (1991). The method developed by Soulsby and Clarke (2005) was implemented in the MOHID system to calculate the bottom shear stresses due to combined waves and currents effect. The previously methods implemented were only appropriate for non-cohesive sediments.

The bottom roughness length was based on hydrodynamic model calibration. The Tagus estuary's intertidal zones are constituted mainly of cohesive sediments (Freire, 2003). Thus, the bottom roughness length in these areas was set to a different value based on particle diameter – bottom CS are usually smooth (van Ledden, 2003). The horizontal diffusion coefficients were defined as a function of the grid resolution ( $\sim \Delta x/100$ ). The model parameters used in this study are described in Table 3.1.

Table 3.1 - Parameters used in the calculation of the cohesive sediment transport

Name	Value	Units
Hindering settling concentration	4	$\text{kg m}^{-3}$
$K_1$	0.006	$\text{m}^4 \text{kg}^{-1} \text{s}^{-1}$
$K_2$	0.01	$\text{m}^3 \text{kg}^{-1}$
$m$	1	
$m_1$	4.65	
Erosion rate	$5 \times 10^{-5}$	$\text{kg m}^{-2} \text{s}^{-1}$
Critical shear stress for erosion	0.4	$\text{N m}^{-2}$
Critical shear stress for deposition	0.2	$\text{N m}^{-2}$
Bottom roughness length	$2.5 \times 10^{-3}$	m
Intertidal bottom roughness length	$3.3 \times 10^{-7} \text{ m}$	m
Horizontal diffusion coefficients	5.0	$\text{m}^2 \text{s}^{-1}$

The salinity effect on flocculation was neglected – the concentration effect was assumed to be sufficient to predict the settling velocities. Therefore, it was assumed that the bottom layer of unconsolidated sediments (fluff layer) is the only source of sediments to the water column by erosion and the only sink due to sedimentation. The erosion of consolidated sediments and the consolidation process were neglected in this study.

### **3.4.2 Initial Conditions**

The bottom layer of unconsolidated sediments was initialized with a uniform mass of  $100 \text{ kg m}^{-2}$  inside the Tagus estuary's delimited area and a null mass outside the estuary. This initialization resulted in a total sediment mass of  $3.5 \times 10^7 \text{ t}$ , two orders of magnitude higher than the mass involved in the Tagus estuary fortnightly erosion-sedimentation cycle. Previous simulations with lower initial mass showed that the model could not converge to an equilibrium solution in terms of suspended sediment concentrations. The initial CS concentration in the water column was set to  $100 \text{ mg L}^{-1}$  inside the estuary and a null concentration outside. The next simulations were initialized with the results of bottom sediment mass and CSS concentrations obtained from the previous simulation.

### **3.4.3 Boundary Conditions**

#### **Ocean**

The tide was propagated from the larger domains to the Tagus estuary domain with the Flather (1976) radiation scheme, which radiates external gravitational waves over the perturbation produced by other mechanisms, such as the wind and the Coriolis force. The CSS concentration at the ocean boundary of the Tagus estuary domain was assumed as null.

#### **Atmosphere**

The atmospheric boundary conditions were provided by the Weather Research and Forecasting model (WRF), implemented with nested grids of 9 km for Portugal and a 3 km in a square domain with approximately  $200 \times 200 \text{ km}$  in an area centred in Lisbon (Trancoso, 2012). Initial and boundary conditions to WRF were provided by the Global Forecast System (GFS) with  $0.5^\circ$  resolution. The results from WRF with 3 km resolution were interpolated to the Tagus estuary model grid.

#### **Discharges**

The lack of recent data about the CSS load in the Tagus river is a restriction to sediment modelling. Herein, a relation (Eq. 3.4) was determined from data (94 samples) of total suspended sediment flow  $Q_{SS}$  ( $\text{kg s}^{-1}$ ) and water flow  $Q$  ( $\text{m}^3 \text{ s}^{-1}$ ) measured in Ómnias sedimentology station between 1984 and 1992 (<http://snirh.apambiente.pt>).

$$Q_{ss} = 0.0043Q^{1.45} \quad r^2 = 0.74 \quad (3.4)$$

The Tagus river inflow was set in the model with hourly data from the Almourol hydrometric station (<http://snirh.apambiente.pt>), which has instantaneous water levels and a flow curve equation valid for the year 2012. This was a very dry year with an average flow of  $83 \text{ m}^3 \text{ s}^{-1}$ . The CSS river load was defined by using water flow data and Eq. 3.4, resulting in an hourly data series. The inputs from the other two most important rivers in the system, Sorraia and Trancão, were defined by using monthly average values based on monitored data (<http://snirh.apambiente.pt>). The total suspended sediment load to the Tagus estuary in 2012 was estimated to be  $1.39 \times 10^5 \text{ t}$ , with 95% ( $1.32 \times 10^5 \text{ t}$ ) coming from the Tagus river (Figure 3.2). In the average year, the suspended sediment load was approximately  $6 \times 10^5 \text{ t}$  (Figure 3.2).

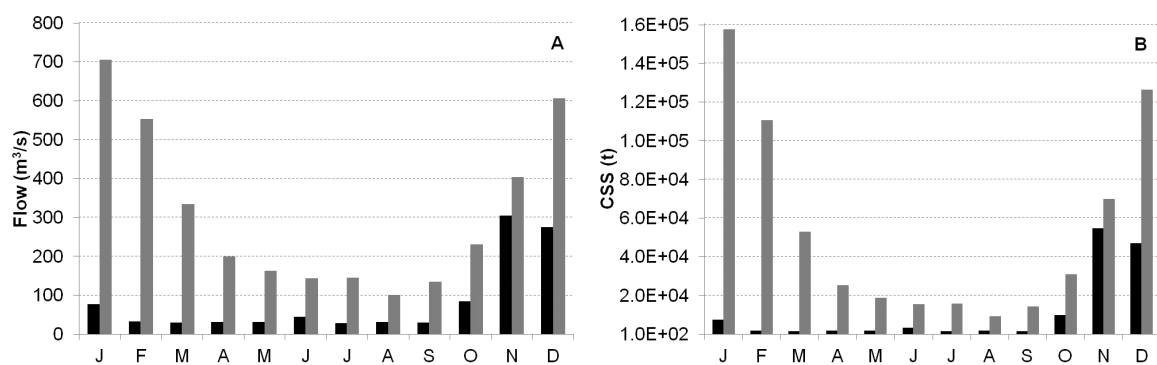


Figure 3.2 - Monthly average Tagus river flow (A) and CSS load (B) in 2012 (black) and in an average year (grey).

### 3.4.4 Waves

A fetch-based wave generation model was used to predict the significant wave height and wave period inside the Tagus estuary. The fetch model implemented in the MOHID system is based on Seymour (1977) and Kang et al. (1982). The fetch wave model uses as input the fetch distances, water depth, wind velocity and direction in each grid cell. The fetch distances were calculated for sixteen directions. As wave propagation is not considered explicitly, this model is only adequate for areas where the ocean swell is blocked. This is the case of the Tagus estuary due to the geometry of the inlet channel, where only local wind waves are generated.

## 3.5 Field data

To verify the tide propagation into the Tagus estuary model, the tidal components obtained by harmonic analysis of the water level results and tide gauges data from Lemos (1972) were compared, making use of the MATLAB T\_Tide package (Pawlowicz et al., 2002). The hydrodynamic model results were also compared with velocity data from the Acoustic Doppler Current Profiler

(ADCP) installed in the buoy B2 (Figure 3.1) from July 2012 onward by the wastewater treatment company SIMARSUL. The ADCP was installed at a depth of 1.8 m, with a blanking zone of 0.5 m and 2 m spacing between cells. As the ADCP only measured velocities at depths below 2.3 m (1.8m+0.5m), the surface velocities were assumed to be nearly the same as those measured at the first cell, based on the small differences between the values measured in the first and second cells. The data from the ADCP were vertically integrated to be directly comparable with the bi-dimensional model results. The minimum depth at the buoy location is about 12.5 m, which results in five cells always with data plus the cell assumed for the surface.

Simulated CSS concentrations were validated against data of sixteen stations monitored by the wastewater treatment companies SIMTEJO and SIMARSUL (Figure 3.1). These stations have been monitored since 2004, with more than forty surface samples in each station measured until 2012. However, the monitored frequency was low to assess fortnightly and daily variation in the CSS concentrations, with few samples per year distributed in different months. To overcome this constraint, data of turbidity measured by two multiparametric probes were compared against simulated CSS. These probes were installed in July of 2012 on the buoys B1 and B2 (Figure 3.2) at a depth close to 1 m. As the turbidity is directly related to the suspended sediment concentration and the turbidity data was stored every twenty minutes, it was possible to verify the fortnightly and daily variation in the model results.

## 3.6 Results

### 3.6.1 Hydrodynamics

Main tidal components amplitudes and phases in the Tagus estuary (M2 and S2) are presented in Figure 3.3. The tide amplitude is amplified throughout the estuary until the upper area, where it decreases due to bottom friction. The results of amplitude and phase are in general very accurate, but the accuracy tends to decrease along the estuary. The grid resolution of 200 m is not sufficient to represent the geometry of the small channels in the upper area of the estuary, which is possibly the reason for these larger differences. The largest errors occurred at V. Franca station, with -0.22 m of amplitude and 12.7° of phase for the M2 and -0.08 m of amplitude and 12.4° of phase for the S2.

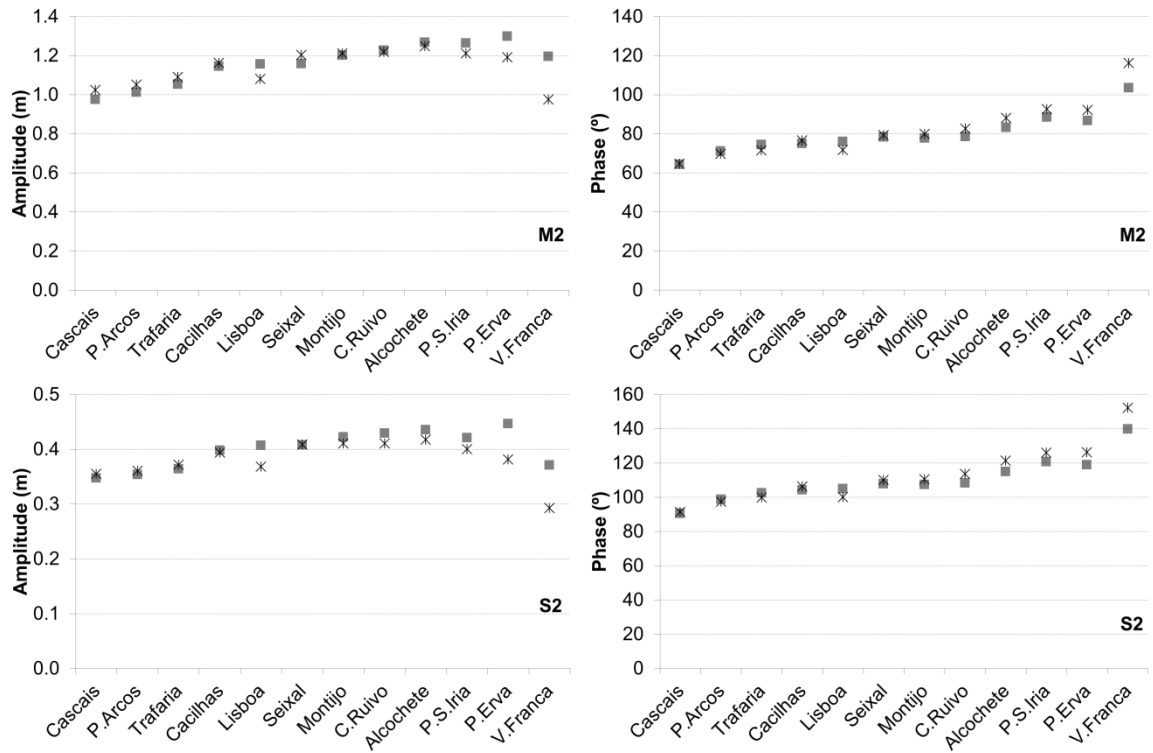


Figure 3.3 - Comparison between the harmonic analysis for data (■) and model results in 2012 (\*) for the two most important tidal components in the Tagus estuary

The velocity modulus results showed a good correlation with data measured by the ADCP installed in the buoy B2 (Figure 3.4). The Root Mean Square Error (RMSE) was  $0.20 \text{ m s}^{-1}$  for a six-month time series. The comparison of water level and velocities (Figure 3.4c, Figure 3.4d) shows that velocity intensities have a large oscillation caused by the tidal cycle. The higher velocity intensities occur on the ebb tides when the water level decreases, with peak values in the order of  $1.0 \text{ m s}^{-1}$  in the spring tide and  $0.4 \text{ m s}^{-1}$  in the neap tide at this location.

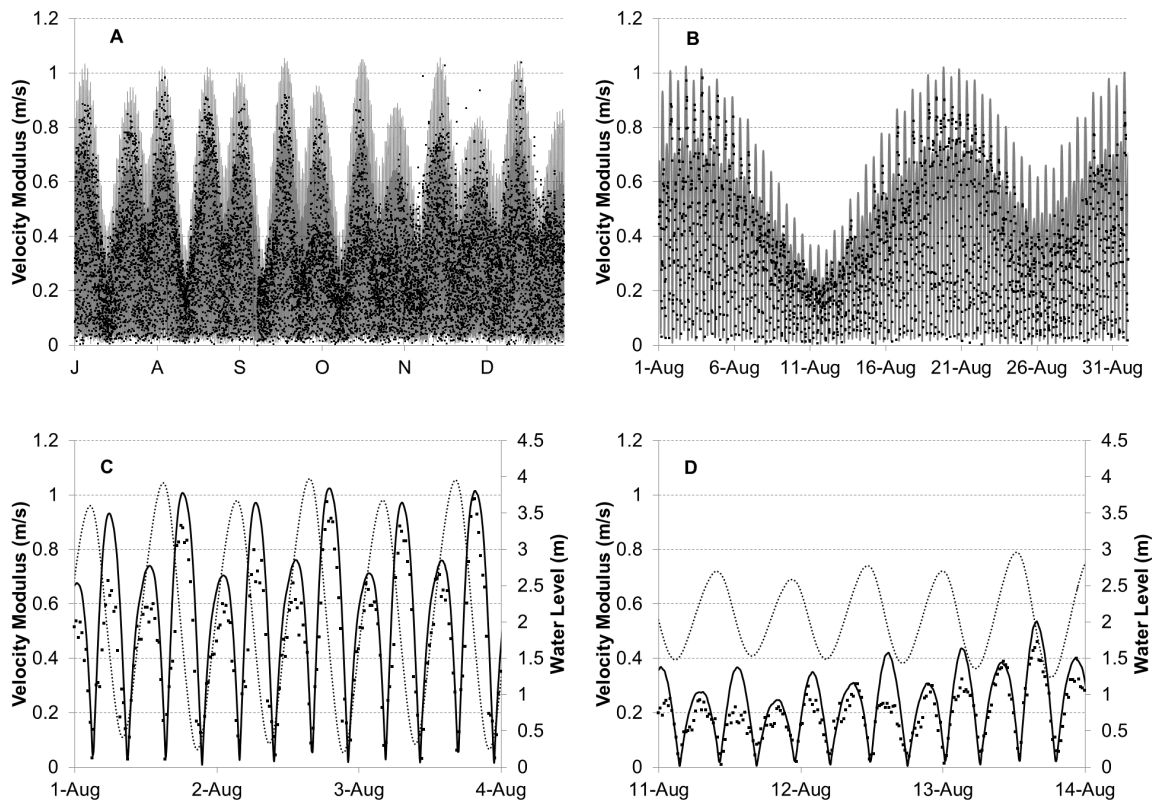
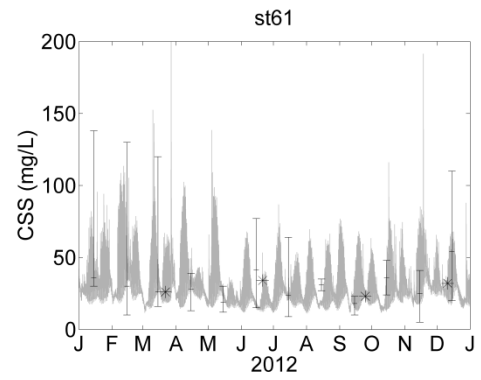
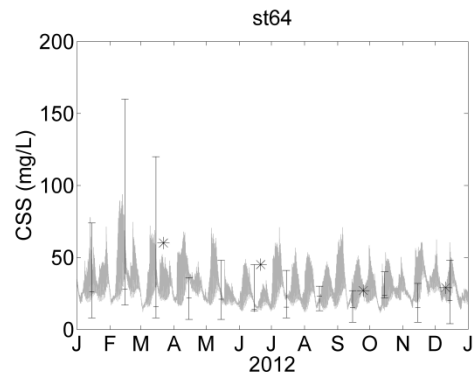
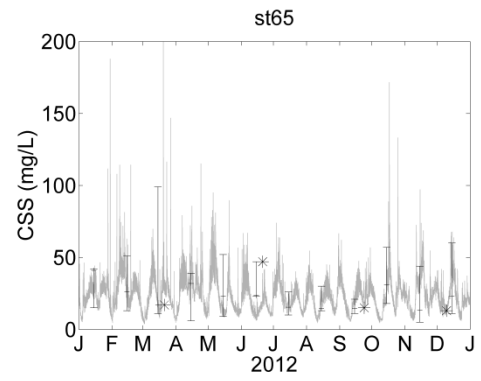
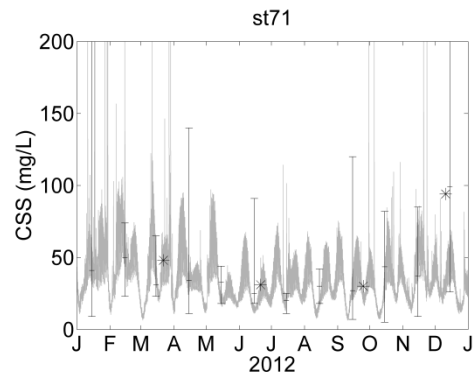
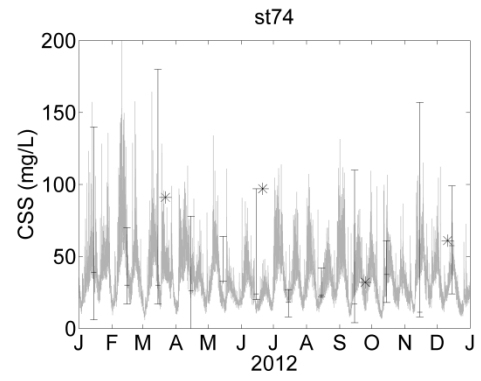
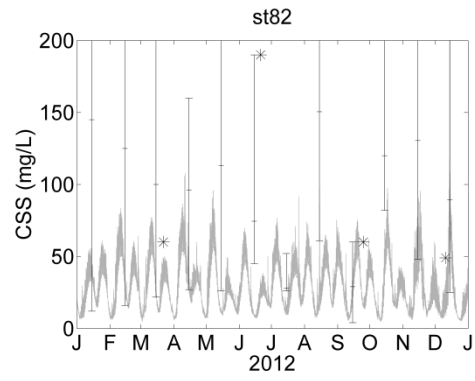
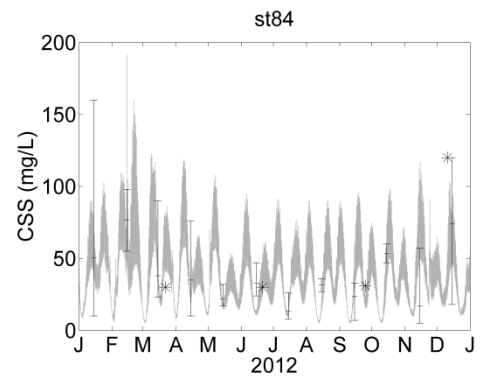
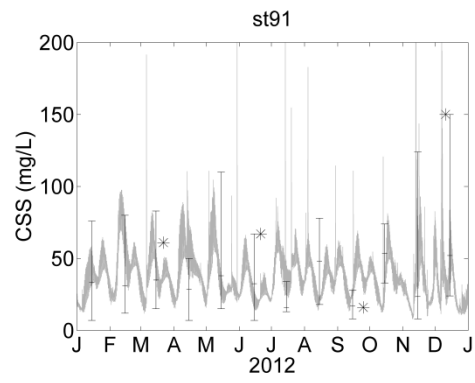


Figure 3.4 - Comparison between the velocity modulus results (—) and data (■) measured by the ADCP installed on buoy B2 for the period between July and December of 2012 (A), with detail to the August month (B). The water level (...) is plotted to show the effect of tide on velocity in a spring tide (C) and a neap tide (D)

### 3.6.2 Cohesive Suspended Sediment

The model reached the observed suspended sediment concentrations along the Tagus estuary after two years of simulation and the third year results were compared against monitored data in Figure 3.5 (stations locations are presented in Figure 3.1). Due to the few samples measured during the reference year, the statistical values (maximum, median and minimum) calculated from the monthly data series were displayed in the graphs for a more representative comparison. In general, the model successfully represented the observed suspended sediment distribution throughout the estuary. The concentrations during spring tides often exceed  $50 \text{ mg L}^{-1}$  in the stations located in shallow areas near the intertidal zones, while in the deeper areas near the mouth of the estuary the concentrations were always less than  $50 \text{ mg L}^{-1}$ , in agreement with measurements.



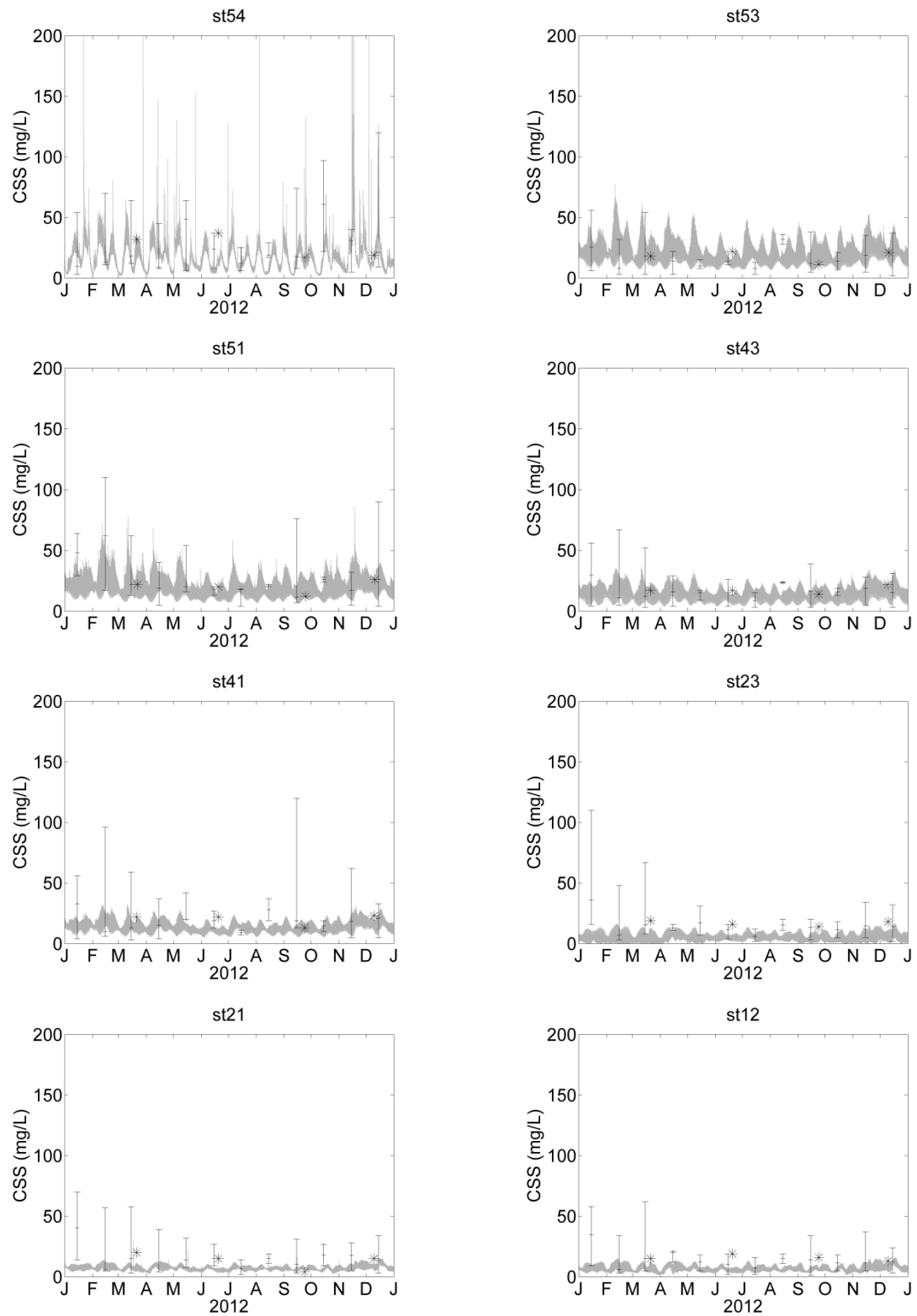


Figure 3.5 - Comparison of simulated (—) cohesive suspended sediment (CSS) concentrations and measured data in the reference year (2012) (\*) and the maximum, median and minimum of the monthly data series between 2004 and 2012 (†)

To verify the fortnightly and daily CSS variation, we compared model results with turbidity data measured on buoys B1 and B2 (Figure 3.6). The fortnightly variation observed in the turbidity data is clearly seen in the simulated CSS at the B2 location, with peak values at spring tides. However, at buoy B1 the model results never reached the peaks observed in the turbidity data. This tendency can also be found in Figure 3.5 for the stations located near the estuary mouth (ST12, ST21 and ST23). The model results at these stations did not reach the maximum observed in the monthly data series but are close to the median values. This is possibly due to the lack of horizontal diffusion in vertically integrated models – the velocity profile variations and density currents effects are not considered.

To investigate whether an equilibrium state was reached, we continued the simulations with and without waves for two more years and the annual average suspended mass in the total area of the Tagus estuary for the five simulated years was calculated (Figure 3.7A). For the scenario with waves, the annual average mass decreased about  $1 \times 10^5$  t in the second year,  $2 \times 10^4$  t in the third year and less than  $1 \times 10^4$  t in the subsequent years. On average, the suspended mass was approximately 30% larger in the simulation with waves after the spin up period. The CSS mass during the third simulated year is shown in Figure 3.7B for both scenarios. The fortnightly erosion-sedimentation cycle is clearly observed. For the simulation without waves the CSS mass varied between  $1.2 \times 10^4$  t during neap tides and  $6.2 \times 10^4$  t during spring tides, while for the simulation with waves this variation was between  $2.0 \times 10^4$  t during neap tides and  $1.0 \times 10^5$  t during spring tides. The total CS flux exported to the ocean in the third simulated year was  $7.2 \times 10^5$  t. To test the importance of bottom initialization, the third year for the scenario with waves was simulated again with a zero initial mass of sediment in the fluff layer. The results (Figure 3.7C) showed that without bottom initialization the mass in suspension was one order of magnitude smaller and the model was unable to reproduce the fortnightly erosion-sedimentation cycles.

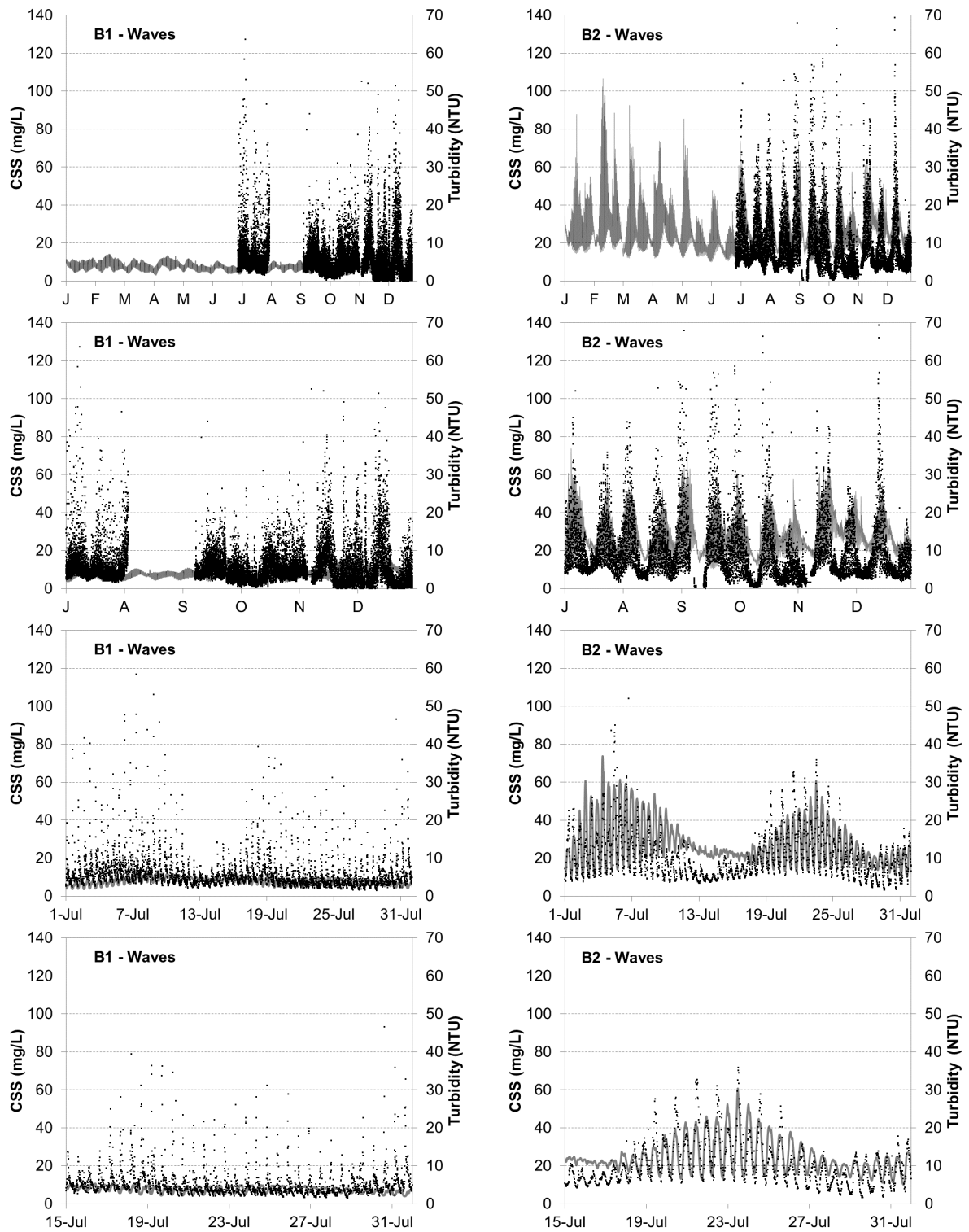


Figure 3.6 - Simulated (—) cohesive suspended sediment (CSS) concentrations ( $\text{mg L}^{-1}$ ) and turbidity data (•) measured by multiparametric probes installed in the buoys B1 and B2 between June and December 2012

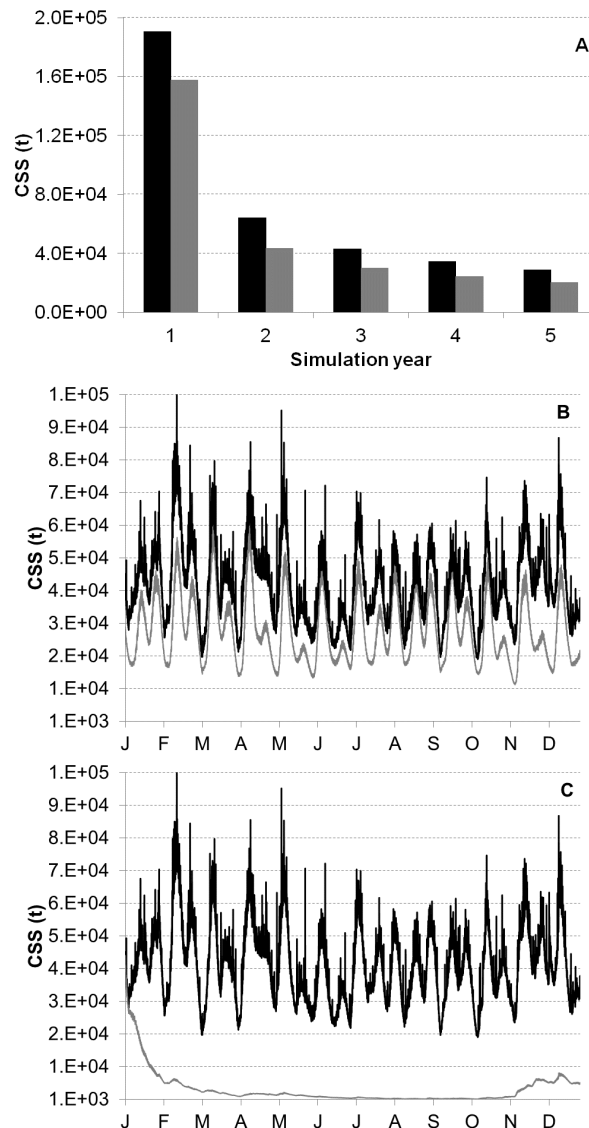


Figure 3.7 - Cohesive suspended sediment (CSS) mass (t) in the Tagus estuary delimited area for the five simulated years (A), during the third simulated year (B) - with waves (black) and without waves (gray) and comparison between the third simulated year with (black) and without (gray) bottom initialization (C)

### 3.6.3 Bottom Sediment

The initial and the final bottom unconsolidated sediment mass in each simulated year are presented in Figure 3.8. The bottom was initialized with a constant sediment mass of  $100 \text{ kg m}^{-2}$ . A large area of the estuary was completely eroded in the first year (Figure 3.8B). After, the bottom presented minor modifications (Figure 3.8C and Figure 3.8D). At the end of the third year, 76% of the initial mass still remained on the estuary bottom. This means that a large fraction of the sediments initially present in the channels was reallocated to the intertidal zone.

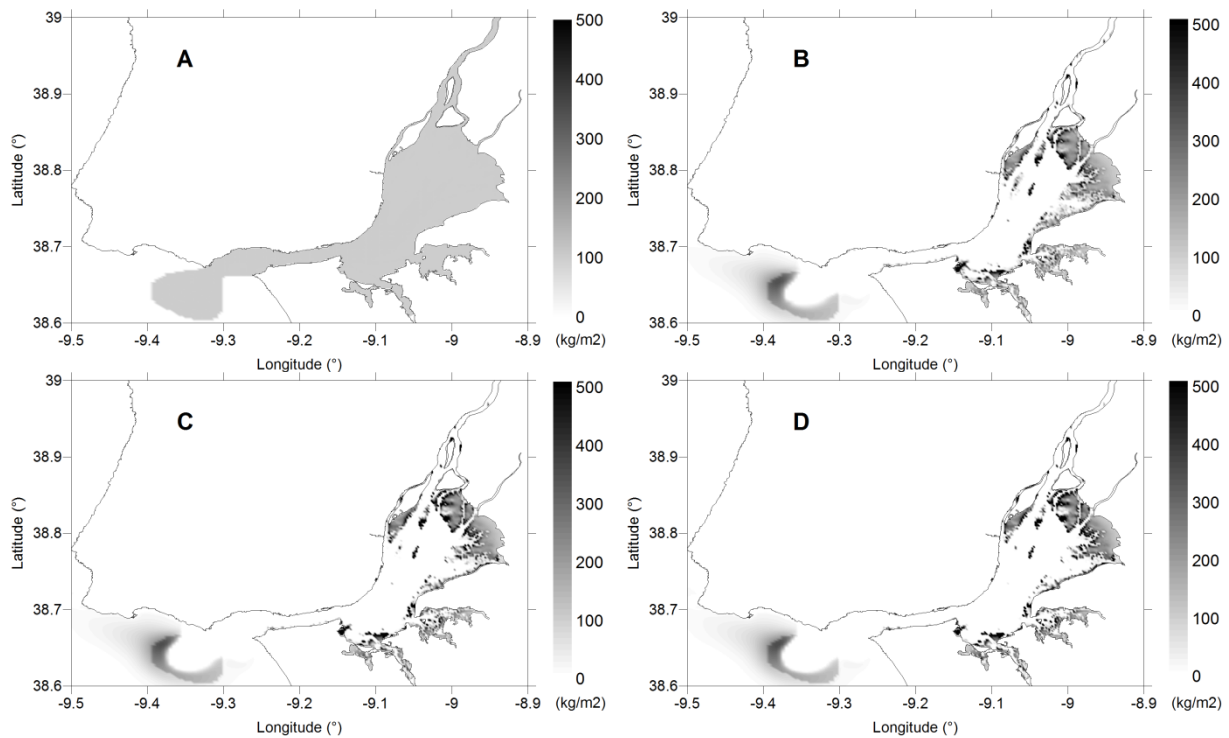


Figure 3.8 - Initial (A) and final bottom sediment mass ( $\text{kg m}^{-2}$ ) after the first (B), second (C) and third (D) year of simulation

### 3.7 Discussion and Conclusions

The model results show that with a proper bottom spin up the model was capable of reproducing the general observed CSS concentrations during the fortnightly and daily erosion-sedimentation cycle along the Tagus estuary, even in a very dry year. The CS, initially uniformly distributed on the bottom, was transported mostly by tidal currents to the tidal flats and salt marshes and was deposited in these areas during slack water of high tides. Without wave action, the bottom CS remained in the intertidal zones due to low velocities in these areas. The inclusion of waves in the simulations was important to trigger CS resuspension in the intertidal zones during windy periods. During ebb tide, these sediments could be carried out of the intertidal zones. However, the tidal currents carried the CS back to these areas, completing a cycle. These results agree with the known cohesive sediment dynamics in estuaries (Whitehouse et al., 2000). Consequently, we can state that the method of Soulsby and Clarke (2005) used in this study is reliable and can be useful to properly calculate the bottom shear stresses due to the combined effect of waves and currents in future studies.

Although the tidal currents are the main factor to the CS erosion, the results suggest that wind waves play an important role in the CS dynamics in the Tagus estuary. According to the model results, the wind waves increased the CSS annual average mass by approximately 30%. However, without a correct bottom initialization, the model was unable to reproduce the CSS mass observed in

the fortnightly erosion-sedimentation cycle. This finding implies that the main contribution for CSS in the Tagus estuary is the mass available at the bottom and the input of the rivers is less important for the normally observed CSS concentrations. The amount of suspended sediment involved in the fortnightly erosion-sedimentation cycle was in the order of magnitude of the annual Tagus river input ( $\sim 10^5$  t), as described by Vale and Sundby (1987).

The salinity effect on flocculation and the consolidation process were neglected in this study. The simulation results indicate that the salinity effect on flocculation can be neglected in CS modelling studies, considering that it is small when compared with the effect of CSS concentrations, as observed by Burt (1984), Puls and Kuehl (1986), van Leussen (1988), Hamm and Migniot (1994) and Soulsby et al. (2013). Therefore, the model was capable of reproducing the mass involved in the fortnightly erosion-sedimentation cycle only considering a bottom layer of unconsolidated sediments. Thus, the implied error of neglecting the erosion of consolidated sediments and the consolidation process seems to be unimportant. Also, the hindered settling was insignificant in this case, since simulated CSS concentrations never reached the range when this effect starts to be relevant.

The model's results agree with the known patterns of bottom sediment distribution in the Tagus estuary (Freire, 2003; Caçador and Duarte, 2012). The estuary channels are composed mostly of sand and the cohesive sediments deposited in this zone are quickly washed away by tidal currents. On the other hand, the intertidal zones are composed mainly of CS. A significant part of the exported sediments to the ocean was deposited on the shelf near the mouth of the Tagus estuary, as verified by Jouanneau et al. (1998). The sediment balance calculated by the Tagus estuary model in 2012 was negative ( $5.8 \times 10^5$  t), which means that the flux to the ocean was higher than the inputs from the rivers. The negative sediment balance indicates that the Tagus estuary loses CS to the ocean in low river flow conditions, as observed in 2012. The bottom sediments can be replenished mainly in extreme flows, as described by Vale (1981). These events are less frequent due to the presence of many dams along the Tagus river, which store a great part of the sediments that would supply the estuary. The reduction in the suspended sediment mass can be a potential risk of future algal blooms because light availability is considered the main limitation factor to the phytoplankton growth in the Tagus estuary due to the high turbidity.

We can conclude that the model reached a state of equilibrium after the spin up period, taking into account that the sediment load of a very dry year was considered in the simulations. Although the annual average mass in suspension decreased approximately  $1 \times 10^4$  t per year after the spin up period, the suspended sediment load from the Tagus river estimated in 2012 ( $1.3 \times 10^5$  t) was almost

five times less than an average year ( $6 \times 10^5$  t). In the future, the initialized bottom layer obtained in this study will be used in a three-dimensional model, adding processes that cannot be addressed by vertically integrated models. This will allow us to verify if the suspended sediment peaks observed in the stations located near the estuary mouth can be reached in three-dimensional mode, as they were not properly represented in the vertically integrated model. Also, the importance of density currents to the sediment balance in the Tagus estuary and the turbulence effect on flocculation will be assessed. In order to improve the prediction of the wave's effect in the CS dynamics, a propagation wave model will be implemented, accounting for ocean swell and wind waves.

## Chapter 4 Development and validation of a morphological model for multiple sediment classes

*The material on which this chapter is based has been previously published in Franz, G., Leitão, P., Pinto, L., Jauch, E., Fernandes, L., Neves, R., 2017. International Journal of Sediment Research, in press.*

### **Abstract**

The complexity of sediment dynamics in aquatic systems can be better understood by applying numerical models. The development of a comprehensive morphological model is presented in this paper. The model aims to predict the sediment transport and bed evolution in natural systems composed of different sediment types. The morphological model was implemented in MOHID, a modelling system that solves the three-dimensional hydrodynamics and advection-diffusion transport of suspended sediments. Multiple sediment classes were taken into account (non-cohesive and cohesive) considering the effects of sediment mixtures and bed consolidation on resistance to erosion. To represent bottom stratigraphy, the bottom column can be divided into several layers. The key points of the simulated processes are discussed in this paper. Model results are assessed in six test cases through comparison with analytic solutions or experimental data. The outcomes demonstrate the model's capacity to simulate the transport dynamics of non-cohesive and cohesive sediments. The speed up of morphological changes by an acceleration factor permitted modelling bed evolution for long time periods. Moreover, a test case for the Tagus Estuary demonstrated the model's capacity for generating realistic sediment distribution based on the local hydrodynamic conditions. Limitations in the availability of bed composition data can be overcome by considering a warm-up run to provide realistic initial conditions for further predictions of morphological developments.

Keywords: sediment transport; sand-mud mixtures; morphodynamics; large-scale models; MOHID modelling system

## 4.1 Introduction

Numerical models allow the diverse processes with different spatial and temporal scales involved in sediment transport to be assessed. Large-scale processes (e.g., tidal motion) are well simulated by numerical models with relatively coarse grid resolutions, whereas small-scale processes (e.g., consolidation and bed load transport) require extremely high grid resolutions to be resolved in detail. Although the detailed reproduction of small-scale processes can be feasible (e.g., Toorman, 1999; Amoudry & Liu, 2010), it is computationally impractical for models aiming to study sediment transport and bed evolution in natural environments. Thus, empirical or simplified physical relations are necessary to represent small-scale (sub-grid) processes in large-scale morphological models, which greatly contribute to models uncertainty. Additional important restrictions of morphological models arise from ignoring the effects of sediment mixtures and consolidation on resistance to erosion (Amoudry & Souza, 2011). Taking into account these issues, a morphological model is developed within the *Modelo Hidrodinâmico* (MOHID – acronym to hydrodynamic model in Portuguese) (Leitão, 2003; Leitão et al., 2008) to predict the three-dimensional sediment transport and bed evolution for different sediment types.

MOHID modelling system has been developed by the Marine and Environmental Technology Research Centre (MARETEC) at the Instituto Superior Técnico (IST) since the early 1990s. Subsequently, MOHID started to be developed and applied by other research centres and companies to solve a broad range of processes (e.g., Santoro et al., 2013, Delpey et al., 2014, Brito et al., 2015, Franz et al., 2016, Fernandes et al., 2016), as an outcome of the open-source philosophy and modular structure. The MOHID hydrodynamic module solves the three-dimensional Navier-Stokes equations, considering the Boussinesq and hydrostatic approximations. The equations are solved through the finite volume method, with a generic vertical discretization that allows implementing different types of vertical coordinates. MOHID is coupled to the Global Ocean Turbulence Model (GOTM), which consists of a set of turbulence-closure models (Buchard et al., 1999; Villarreal et al., 2005). A new module (Sediment) was developed and other modules were adapted to include the developments of this work. The sediment transport and morphological evolution are computed “online” with the hydrodynamics. In other words, bathymetry changes immediately affect hydrodynamic calculations, which in turn modify the sediment transport.

In this paper, the morphological model developed to simulate the dynamics of sediments in natural systems is described, considering the effects of mixed size fractions and consolidation on sediment motion. The concepts applied to the morphological model development are briefly discussed in Section 4.2, followed by the description of the mathematical equations and numerical

implementation (Section 4.3). The model results are assessed for six test cases by comparison with analytic solutions or experimental data (Section 4.4). The chapter is concluded in Section 4.5 with an overview of topics for further development of the model.

## 4.2 Background

Sediment transport in aquatic systems results from the interactions between turbulent flows and sediment particles. The mineralogical grains that compose natural sediments are classified according to their diameters into clay ( $< 0.004$  mm), silt ( $0.004 - 0.063$  mm), sand ( $0.063 - 2$  mm), and gravel ( $2 - 64$  mm). In practice, bottom sediments are complex combinations of different grain sizes, as well as organic particles, shells fragments, living organisms, etc. Sediment particles are often divided into two classes: cohesive (clay, silt, and organic particles) and non-cohesive (sand and gravel). They differ by the importance of electrochemical forces acting among particles. These forces originate the processes of flocculation and consolidation.

Cohesive sediments (commonly called mud) are transported in suspension primarily as flocculated material. Collisions between particles, with consequent formation of flocs, are more probable in high concentrations. Thus, mud concentration and water turbulence are the main parameters affecting flocculation in natural systems, such as estuaries (Soulsby et al., 2013). Flocculation significantly increases settling velocities. However, above a certain concentration settling velocities start to decrease due to hindering effects (Kynch, 1952; Winterwerp, 2002).

The development of a matrix structure takes place when the mud concentration exceeds the gel point. The self-weight of the sediment matrix starts a gradual expulsion of interstitial water (first step of consolidation). The matrix continually collapses until the excess pore pressure is completely dissipated. A further step of consolidation occurs due to the deformable behaviour of mud particles. The consolidation increases the bed density and, consequently, the resistance to erosion. Four states of mud can be distinguished based on mass concentration or dry density: suspended, fluid mud, recently deposited, and settled. These states can be associated with different settling regimes: flocculation, hindered, permeability, and effective-stress (Winterwerp, 2002; Chauchat et al., 2013). Below the gel point, segregation of sand and mud may occur (e.g., Torfs et al., 1996). Once the gel point is reached, sand particles get trapped in the mud matrix and segregation is restricted.

The transport of sand particles can be divided into suspended and bed load, which consists of gliding, rolling, and saltating particles in frequent contact with the bed. The initiation of motion takes place when the immersed particle weight is overcome by drag and lift forces, associated with turbulent flows. The critical bed shear stress for erosion of uniform sand was determined by Shields

(1936), resulting in higher values for larger particle diameters. However, in unimodal sand mixtures, the entire range of grain sizes becomes mobile at nearly the same bed shear stress, which corresponds approximately to the Shields curve value for the mixture median diameter (Wilcock, 1993; van Rijn, 2007c). Thus, in sand mixtures, smaller size fractions require higher bed shear stresses to be set into motion, whereas larger size fractions are set into motion at smaller bed shear stresses. This behaviour is explained by the hiding of smaller particles by larger particles, as well as a greater exposure of larger particles in a sand mixture than in uniform bed material.

Sand particles are in contact with each other in non-cohesive beds (mud contents below about 30% by dry weight). Nevertheless, mud particles can fill the spaces between sand grains, increasing their resistance to removal (Mitchener & Torfs, 1996; Panagiotopoulos et al., 1997). If the mud content exceeds about 30%, a matrix of mud particles is formed which incorporates the sand grains. Thus, the bed starts to have a cohesive behaviour that increases the resistance to erosion and prevents bed load transport from occurring (van Ledden, 2003). At high mud contents (above about 50%), the bed becomes fully cohesive and sediments are eroded in clusters. In this case, the critical bed shear stress of the mixture is independent of the sand grain sizes (Panagiotopoulos et al., 1997).

### 4.3 Numerical model

The morphological model was developed to simulate the dynamics of sediment in natural systems, considering the effects of mixed size fractions on sediment motion. To represent bottom stratigraphy, the bottom column can be divided into several layers. The consolidation of cohesive sediment can increase the bed density, affecting the resistance to erosion, the thickness of the sediment column and the bathymetry. As cohesive sediment form flocs, the diameter of individual particles becomes irrelevant for their transport. Therefore, cohesive sediment was assigned as a unique class, considering flocculation as a function of suspended sediment concentration and turbulence. In contrast, the number of sand classes is unlimited.

#### 4.3.1 Layers description

Four compartments were distinguished for modelling the different processes involved in sediment dynamics (Figure 4.1): water column, fluid mud layer, active layer, and settled layers. The bottom column is composed of the active layer (bottom upper layer) and settled layers. The fluid mud layer acts as an interface between the water column and the active layer. The simulated processes associated with the different compartments are described in the following subsections and schematized in Figure 4.2.

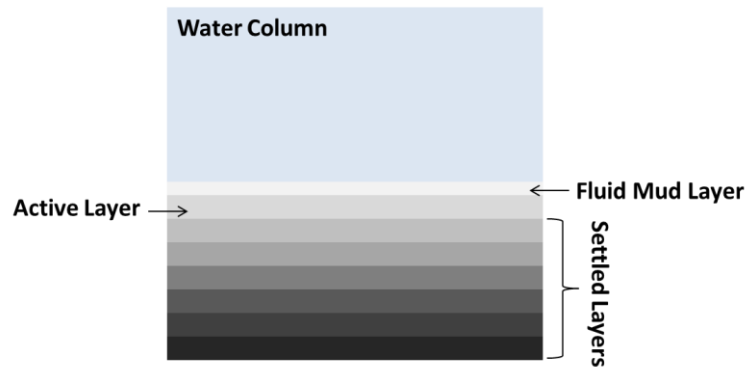


Figure 4.1 – Four compartments used for modelling sediment dynamics. The different colours in the settled layers represent sediment stratigraphy.

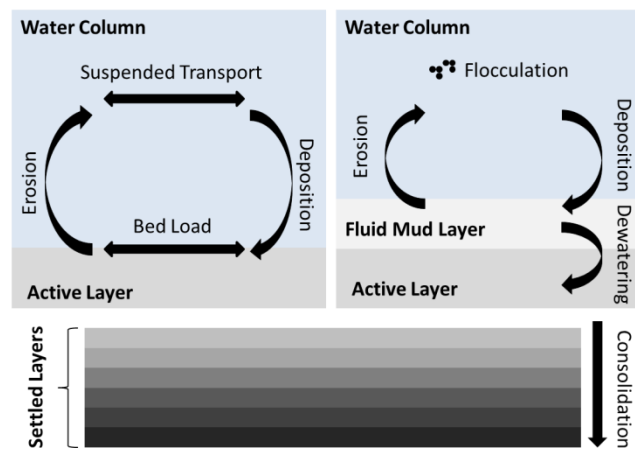


Figure 4.2 - Processes associated with the different model compartments.

### Water column

In the water column, sand and mud particles are carried in suspension by currents and turbulent vortices (advection/diffusion). The mud settling is determined by the flocculation regime. While mud is previously deposited in the fluid mud layer, sand is deposited directly on the active layer.

### Fluid mud layer

The fluid mud layer permits the model to consider the concentration effects on settling velocities (hindered settling) of mud particles that usually occur in a thin layer near the bottom. Otherwise, these hindering effects could only be simulated in the water column with very high vertical grid resolutions, which is computationally impractical for large scale models. In estuarine systems, fluid mud can be found in periods of slack water, being easily washed out when the intensity of tidal currents starts to increase. At this stage of model development, the fluid mud layer was assumed to be a thin interface between the water column and bottom. The development of a persistent fluid mud, which can be found in some aquatic systems, was neglected here. Thus, the movement of fluid mud due to gravity was ignored.

### Active layer

The active layer represents the bottom upper layer that is exposed to the action of currents and waves. Therefore, the active layer thickness is modified by erosion and deposition processes. In the case of net scour, the active layer can be merged to the first settled layer when the minimum user-defined thickness is reached. In the case of net aggradation, a new active layer is created when the maximum user-defined thickness is reached. The effects of grain hiding and exposure in a sand mixture were considered, as well as the increase in the resistance to removal of sand particles due to mud content in non-cohesive and cohesive beds. The consolidation process was disregarded in the active layer, as the effective-stress due to self-weight is taken as zero at the bed surface.

### Settled layers

The settled layers allow the bottom column stratigraphy to be represented. Consolidation takes place when the settled layers present cohesive behaviour. If a settled layer becomes the new active layer, the resistance to erosion will depend on the degree of consolidation. In the case of net aggradation, the last layer is disregarded when the maximum number of settled layers defined by the user is reached.

### 4.3.2 Suspended sediment transport

The transport of suspended sediment in the water column is calculated by solving the three-dimensional advection-diffusion equation for sand (Eq. 4.1a) and mud particles (Eq. 4.1b).

$$\begin{aligned} & \frac{\partial c_s^{(l)}}{\partial t} + \frac{\partial u c_s^{(l)}}{\partial x} + \frac{\partial v c_s^{(l)}}{\partial y} + \frac{\partial (w - w_s^{(l)}) c_s^{(l)}}{\partial z} \\ & - \frac{\partial}{\partial x} \left( \varepsilon_x \frac{\partial c_s^{(l)}}{\partial x} \right) - \frac{\partial}{\partial y} \left( \varepsilon_y \frac{\partial c_s^{(l)}}{\partial y} \right) - \frac{\partial}{\partial z} \left( \varepsilon_z \frac{\partial c_s^{(l)}}{\partial z} \right) = 0 \end{aligned} \quad (4.1a)$$

$$\begin{aligned} & \frac{\partial c_m}{\partial t} + \frac{\partial u c_m}{\partial x} + \frac{\partial v c_m}{\partial y} + \frac{\partial (w - w_m) c_m}{\partial z} \\ & - \frac{\partial}{\partial x} \left( \varepsilon_x \frac{\partial c_m}{\partial x} \right) - \frac{\partial}{\partial y} \left( \varepsilon_y \frac{\partial c_m}{\partial y} \right) - \frac{\partial}{\partial z} \left( \varepsilon_z \frac{\partial c_m}{\partial z} \right) = 0 \end{aligned} \quad (4.1b)$$

where  $t$  is the time (s);  $x$ ,  $y$ , and  $z$  are the horizontal and vertical directions (m);  $c_s^{(l)}$  and  $c_m$  are the mass concentration ( $\text{kg m}^{-3}$ ) of the sand fraction ( $l$ ) and mud, respectively;  $u$ ,  $v$ , and  $w$  are the flow velocity components ( $\text{m s}^{-1}$ );  $\varepsilon_x$ ,  $\varepsilon_y$ , and  $\varepsilon_z$  are the horizontal and vertical eddy diffusivities ( $\text{m}^2 \text{s}^{-1}$ ); and  $w_s^{(l)}$  and  $w_m$  are the settling velocity of the sand fraction ( $l$ ) and mud ( $\text{m s}^{-1}$ ), respectively.

Deposition/erosion fluxes can occur between the water column and the bottom. The net flux of sediment can change the bathymetry and, consequently, the hydrodynamics. On the other hand, changes in hydrodynamics can modify the deposition/erosion fluxes and sediment transport. Settling velocities of sand and mud particles are calculated following different methodologies, described in the following subsections.

### 4.3.3 Sand settling velocity

The settling velocity of the different sand fractions is computed following van Rijn (1993):

$$w_s^{(l)} = \frac{(\rho_r - 1)gd^{(l)2}}{18\nu}, 63 \mu m < d^{(l)} \leq 100 \mu m$$

$$w_s^{(l)} = \frac{10\nu}{d^{(l)}} \left[ \left( 1 + \frac{0.01(\rho_r - 1)gd^{(l)3}}{\nu^2} \right)^{0.5} - 1 \right], 100 \mu m < d^{(l)} \leq 1000 \mu m$$

$$w_s^{(l)} = 1.1[(\rho_r - 1)gd^{(l)}]^{0.5}, 1000 \mu m < d^{(l)} \quad (4.2)$$

where  $\rho_r$  is the relative density of sand ( $\rho_s / \rho_w$ ), in which  $\rho_s$  and  $\rho_w$  are the sand particle density and water density ( $\text{kg m}^{-3}$ ), respectively;  $g$  is the acceleration of gravity ( $\text{m s}^{-2}$ );  $d^{(l)}$  is the representative diameter of sand class ( $l$ ) (m); and  $\nu$  is the kinematic viscosity of water ( $\text{m}^2 \text{s}^{-1}$ ). When only one sand class is considered, the settling velocity should be computed for a representative diameter, which may be considerably smaller than the median diameter ( $d_{50}$ ) of the bed material.

### 4.3.4 Mud settling velocity

The settling velocity of mud flocs ( $w_m$ ) was based on the assumptions of a two-class floc population (microflocs and macroflocs) in quasi-equilibrium with the flow (Soulsby et al., 2013):

$$w_m = \max[rw_M + (1 - r)w_\mu; 0.0002] \quad (4.3a)$$

$$w_M = \min \left[ B_M (\bar{s}_{e\mu} - 1) \left( \frac{\varepsilon \bar{d}_\mu^4}{\nu^3} \right)^{0.166} g c^{2.672k} \left( \frac{\nu}{\varepsilon} \right)^{1/2} \exp \left[ - \left( \frac{u_{*SM}}{u_* \xi^{1/2}} \right)^N \right]; 0.005 \right] \quad (4.3b)$$

$$w_\mu = \min \left[ B_\mu (s - 1) \left( \frac{\varepsilon d_1^4}{\nu^3} \right)^{0.39} g \left( \frac{\nu}{\varepsilon} \right)^{1/2} \exp \left[ - \left( \frac{u_{*S\mu}}{u_* \xi^{1/2}} \right)^n \right]; 0.001 \right] \quad (4.3c)$$

where  $w_M$  is the macrofloc settling velocity ( $\text{m s}^{-1}$ );  $w_\mu$  is the microfloc settling velocity ( $\text{m s}^{-1}$ );  $\varepsilon$  is the total kinetic energy (TKE) dissipation rate ( $\text{m}^2 \text{s}^{-3}$ );  $u_*$  is the shear velocity ( $\text{m s}^{-1}$ );  $\xi = 1 - z / h$ , where  $h$  is the water depth (m) and  $z$  is the height above the bed (m); and  $c$  is the dimensionless concentration ( $c_m / \rho_w$ ). The remaining coefficients were calibrated by Soulsby et al. (2013) against a

large dataset of in-situ observations of floc size and settling velocities from Northern European estuaries, resulting in:  $B_M = 0.860$ ,  $k = 0.0825$ ,  $u_{*SM} = 0.067 \text{ m s}^{-1}$ ,  $N = 0.463$ ,  $B_\mu = 0.363$ ,  $u_{*S\mu} = 0.025 \text{ m s}^{-1}$ ,  $n = 0.66$ ,  $s = 2.6368$ ,  $d_1 = 10^{-5} \text{ m}$ ,  $\bar{s}_{e\mu} = 1.15$ , and  $\bar{d}_\mu = 10^{-4} \text{ m}$ . The relative concentration of microflocs and macroflocs ( $r$ ) is determined only as function of the mud concentration:

$$\begin{aligned} r &= 0.1 && \text{when } \log_{10}(c_m) < 0 \\ r &= 0.1 + 0.221\log_{10}(c_m) && \text{when } 0 \leq \log_{10}(c_m) < 4.07 \\ r &= 1 && \text{when } \log_{10}(c_m) \geq 4.07 \end{aligned} \quad (4.4)$$

The settling velocities of microflocs and macroflocs are related to floc size and density via the Kolmogorov microscale as a function of sediment concentration and turbulent shear stress. The formulae are written in terms of the dissipation rate of turbulent kinetic energy ( $\varepsilon$ ). Thus, the foregoing equations are suitable for models that apply  $\kappa$ - $\varepsilon$  turbulence closure. To avoid overestimated values, maximum settling velocities for microflocs ( $1 \text{ mm s}^{-1}$ ) and macroflocs ( $5 \text{ mm s}^{-1}$ ) were set based on data presented in Soulsby et al. (2013) for the Tamar and Gironde estuaries.

#### 4.3.5 Initiation of sediment motion

The motion of bottom sediments is controlled primarily by the frictional force exerted by currents and waves per unit area of the bed, which is called bed shear stress. In the absence of waves, the bed shear stress ( $\vec{\tau}_b$ ) is related only to current velocity following the quadratic friction law ( $\vec{\tau}_b = \rho_w C_D \vec{u} |\vec{u}|$ ). The drag coefficient ( $C_D$ ) is calculated by assuming a classic logarithmic profile  $C_D = [k/\ln(z/z_0)]^2$ , where  $k = 0.41$  is the von Kármán's constant,  $z$  is the distance above the bed, and  $z_0$  is the bed roughness length. The overall resistance to flow is related to the total bed shear stress, while only the skin friction contribution acts directly on bottom sediment grains (Einstein, 1950). Incipient motion occurs when the grain-related bed shear stress ( $\tau'_b$ ) becomes higher than a critical value ( $\tau'_b > \tau_e$ ).

#### Critical shear stress of a pure sand bed

The equation for the critical shear stress of sand fractions ( $\tau_e^{(l)}$ ) on a pure sand bed was based on the critical Shields parameter ( $\theta_{D*}$ ) modified by van Rijn (2007a):

$$\tau_e^{(l)} = g(\rho_s - \rho_w) d^{(l)} \theta_{D*}^{(l)} \eta^{(l)} \quad (4.5a)$$

where:

$$\begin{aligned}
\theta_{D_*}^{(l)} &= 0.115D_*^{-0.5} & D_* \leq 4 \\
\theta_{D_*}^{(l)} &= 0.14D_*^{-0.64} & 4 < D_* \leq 10 \\
\theta_{D_*}^{(l)} &= 0.04D_*^{-0.1} & 10 < D_* \leq 20 \\
\theta_{D_*}^{(l)} &= 0.013D_*^{0.29} & 20 < D_* \leq 150 \\
\theta_{D_*}^{(l)} &= 0.055 & 150 < D_*
\end{aligned} \tag{4.5b}$$

in which  $D_* = d^{(l)}[(\rho_r - 1)g/v^2]^{1/3}$  is the dimensionless particle diameter, and  $\eta^{(l)}$  is the hiding/exposure factor of sand class ( $l$ ) in a mixture.

The  $\eta^{(l)}$  factor is computed through the equation of Wu et al. (2000), which relates the bed-material gradation with hiding and exposure probabilities:

$$\eta^{(l)} = \left( P_{exp}^{(l)} / P_{hid}^{(l)} \right)^{-0.6} \tag{4.6a}$$

$$P_{hid}^{(l)} = \sum_{j=1}^L f^{(j)} \frac{d^{(j)}}{d^{(l)} + d^{(j)}} \tag{4.6b}$$

$$P_{exp}^{(l)} = \sum_{j=1}^L f^{(j)} \frac{d^{(l)}}{d^{(l)} + d^{(j)}} \tag{4.6c}$$

where  $P_{hid}^{(l)}$  and  $P_{exp}^{(l)}$  are the hiding and exposure probabilities of sand class ( $l$ ), respectively;  $L$  is the total number of sand classes; and  $f^{(j)}$  is the fraction of the sand class  $j$  present in the active layer.

### Critical shear stress of a sand-mud bed

The mud content ( $p_m$ ) affects the critical shear stress of sand particles differently in non-cohesive and cohesive beds. When mud is incorporated in a pure sand bed, the spaces between sand grains starts to be filled up, increasing their resistance to removal. If the mud content overcomes a threshold value ( $p_{m1}$ ), the bed starts to have a cohesive behavior and the critical shear stress increases at a greater rate (Panagiotopoulos et al., 1997). This threshold value is calculated as  $p_{m1} = \alpha d_{50,s}$ , where  $d_{50,s}$  is the weighted average diameter of all sand classes, and  $\alpha$  is a tuning parameter that varies between  $1 \times 10^3 \text{ m}^{-1}$  and  $3 \times 10^3 \text{ m}^{-1}$ . The maximum values for  $p_{m1}$  are in the range of 0.2 to 0.4 (Le Hir et al., 2011).

#### Non-cohesive bed

For sand particles in a non-cohesive bed, the effect of mud content on the critical shear stress is obtained following van Ledden (2003):

$$\tau_{e,s}^{(l)} = (1 + p_m)^\beta \tau_e^{(l)} \quad \text{if } p_m \leq p_{m1} \quad (4.7)$$

where  $\beta$  is a calibration coefficient. The critical shear stress of mud particles in a non-cohesive bed is considered to be equal to the minimum critical shear stress of the sand fractions,  $\tau_{e,m} = \min[\tau_{e,s}^{(l)}]$ , where the subscripts  $m$  and  $s$  indicate mud and sand, respectively. The rationale behind this statement is that, when a sand particle is moved, the mud particles trapped in the gaps are washed out.

#### Cohesive bed

The critical shear stress of mud particles in a cohesive bed is computed based on the equation of Mitchener and Torfs (1996), which covers mixed beds and consolidated beds up to bulk densities of  $1800 \text{ kg m}^{-3}$ :

$$\tau_{e,m} = 0.015(\rho_B - 1000)^{0.73} \quad (4.8)$$

where  $\rho_B = 1000\phi + 2650(1 - \phi)$  is the bulk density; and  $\phi$  is the porosity of a sand-mud mixture, computed considering the fractional packing model of Koltermann and Gorelick (1995). The porosity depends on the dry density of cohesive sediments, which is modified by the consolidation process, as presented in Section 4.3.9.

The critical shear stress of sand particles in a cohesive bed is computed considering a transition between the initial and full cohesive behaviour (Eq. 4.9). This transition was observed in experimental studies (e.g. Panagiotopoulos et al., 1997). In fully cohesive beds, above mud contents ( $p_{m2}$ ) of 0.5 to 0.7, the critical shear stress is equal for the entire range of sand fractions and mud.

$$\tau_{e,s}^{(l)} = \frac{(p_{m2} - p_m)}{(p_{m2} - p_{m1})} \left( (1 + p_{m1})^\beta \tau_e^{(l)} - \tau_{e,m} \right) + \tau_{e,m} \quad \text{if } p_{m1} < p_m \leq p_{m2} \quad (4.9a)$$

$$\tau_{e,s}^{(l)} = \tau_{e,m} \quad \text{if } p_m > p_{m2} \quad (4.9b)$$

### 4.3.6 Bed load

The dimensionless bed load transport rate ( $\Phi^{(l)}$ ) for each sand class ( $l$ ) is given by the general expression (Soulsby & Damgaard, 2005; Amoudry & Souza, 2011):

$$\Phi^{(l)} = k_{\Phi 1} \theta^{k_{\Phi 2}} \left( \theta - \theta_{cr}^{(l)} \right)^{k_{\Phi 3}} f^{(l)} \text{ for } \theta \geq \theta_{cr}^{(l)} \quad (4.10a)$$

$$\Phi^{(l)} = 0 \text{ for } \theta < \theta_{cr}^{(l)} \quad (4.10b)$$

where  $\theta = \tau'_b / [g(\rho_s - \rho_w)d^{(l)}]$  is the non-dimensional bed shear stress;  $\theta_{cr}^{(l)} = \tau'_{e,s} / [g(\rho_s - \rho_w)d^{(l)}]$  is the non-dimensional critical shear stress;  $f^{(l)}$  is the fraction of the sand class  $l$  present in the active layer; and  $k_{\Phi 1}$ ,  $k_{\Phi 2}$  and  $k_{\Phi 3}$  are calibration coefficients that allow different equations for bed load transport found in the literature (Table 4.1) to be represented.

Table 4.1 – Coefficients for the bed load equation based on different sources

Source	$k_{\Phi 1}$	$k_{\Phi 2}$	$k_{\Phi 3}$
<b>Meyer-Peter and Müller (1948)</b>	8	0	1.5
<b>Wilson (1966)</b>	12	1.5	0
<b>Fernandez Luque and van Beek (1976)</b>	5.7	0	1.5
<b>Ribberink (1998)</b>	11	0	1.65
<b>Soulsby and Damgaard (2005)</b>	12	0.5	1
<b>Kleinhans and Grasmeyer (2006)</b>	1	0	1.5

Adapted from Amoudry and Souza (2011)

The bed load transport rate ( $q^{(l)}$ ) in mass units ( $\text{kg m}^{-1}\text{s}^{-1}$ ) for each sand class ( $l$ ) is equal to:

$$q^{(l)} = \rho_s \Phi^{(l)} \left[ g(\rho_r - 1) d^{(l)3} \right]^{1/2} \quad (4.11)$$

#### Cohesive effect

The bed load transport is considered to decrease linearly with mud content in cohesive beds until the bed becomes fully cohesive (Eq. 4.12). In this case, the bed load transport is assumed to be nil. This approach avoids a large spatial discontinuity in the bed load transport for a small change in the mud content.

$$q_b^{(l)} = q^{(l)} \text{ for } p_m \leq p_{m1} \quad (4.12a)$$

$$q_b^{(l)} = \frac{(p_{m2} - p_m)}{(p_{m2} - p_{m1})} q^{(l)} \text{ for } p_m > p_{m1} \quad (4.12b)$$

$$q_b^{(l)} = 0 \text{ for } p_m \geq p_{m2} \quad (4.12c)$$

### Bed slope effect

Bed slope affects the magnitude and direction of bed load transport. The bed load components parallel to the velocity components ( $u_b$  and  $v_b$ ) at the near bottom layer are adjusted to consider the bed slope effect (Eq. 4.13), based on the works of Bagnold (1966) and Ikeda (1982).

$$q_{bu}^{(l)} = \alpha_s (q'_{bu}{}^{(l)} - \alpha_n q'_{bv}{}^{(l)}) \quad (4.13a)$$

$$q_{bv}^{(l)} = \alpha_s (q'_{bv}{}^{(l)} + \alpha_n q'_{bu}{}^{(l)}) \quad (4.13b)$$

where

$$q'_{bu}{}^{(l)} = \frac{u_b}{(u_b^2 + v_b^2)^{1/2}} q_b^{(l)} \quad (4.14a)$$

$$q'_{bv}{}^{(l)} = \frac{v_b}{(u_b^2 + v_b^2)^{1/2}} q_b^{(l)} \quad (4.14b)$$

$$\alpha_s = 1 + \alpha_{bs} \left( \frac{\tan(\vartheta)}{\cos\left(\tan^{-1}\left(\frac{\partial z_b}{\partial s}\right)\right) \left(\tan(\vartheta) - \frac{\partial z_b}{\partial s}\right)} - 1 \right) \quad (4.15a)$$

$$\alpha_n = \alpha_{bn} \left( \frac{\tau_{e,s}^{(l)}}{\tau_b} \right)^{0.5} \frac{\partial z_b}{\partial n} \quad (4.15b)$$

in which  $q'_{bu}{}^{(l)}$  and  $q'_{bv}{}^{(l)}$  are the bed load components before the adjustment due to the bed slope effect;  $\alpha_s$  and  $\alpha_n$  are the bed slope adjustment factors in the longitudinal ( $s$ ) and transversal ( $n$ ) directions, respectively;  $\alpha_{bs}$  and  $\alpha_{bn}$  are tuning parameters defined by default as 1.0 and 1.5, respectively;  $\vartheta$  is the internal angle of friction of bed material; and  $z_b$  is the distance from the bed to a reference height (e.g., the hydrographic zero). The longitudinal ( $\partial z_b / \partial s$ ) and transversal ( $\partial z_b / \partial n$ ) bed slopes relative to the bed load transport vector before the adjustment are calculated as:

$$\frac{\partial z_b}{\partial s} = \frac{\partial z_b}{\partial x} \frac{q'_{bu}{}^{(l)}}{|q_b^{(l)}|} + \frac{\partial z_b}{\partial y} \frac{q'_{bv}{}^{(l)}}{|q_b^{(l)}|} \quad (4.16a)$$

$$\frac{\partial z_b}{\partial n} = -\frac{\partial z_b}{\partial x} \frac{q'_{bv}{}^{(l)}}{|q_b^{(l)}|} + \frac{\partial z_b}{\partial y} \frac{q'_{bu}{}^{(l)}}{|q_b^{(l)}|} \quad (4.16b)$$

The maximum longitudinal bed slope is assumed to be equal to  $0.9 \tan(\vartheta)$ .

### 4.3.7 Erosion and deposition

The erosion and deposition processes are managed differently for sand and mud. Mud is firstly deposited in the fluid mud layer, where concentrations are in the hindering settling regime range, below the gel point. Mud can easily be eroded to the water column and sand particles can pass through the fluid mud layer directly to the bottom (hindering settling of sand particles was neglected). In the active layer, mixtures of different sand fractions and mud may occur. The critical shear stress of sand particles is affected by hiding and exposure effects, as well as by the mud content. In fully cohesive beds, the sediment is eroded in clusters. Thus, the erosion flux of sand particles is calculated similarly to mud. The deposition fluxes are always solved implicitly for numerical stability.

#### Fluid mud layer

The exchange of mud between the water column and the fluid mud layer is calculated based on Ariathurai-Partheniades' erosion formula (Ariathurai & Arulanandan, 1978) and Krone's deposition formula (Krone, 1962). Mud is eroded from the fluid mud layer when the total (grain and form related) bed shear stress ( $\tau_b$ ) exceeds the critical value for erosion ( $\tau_{e,fl}$ ), but are deposited when  $\tau_b$  falls below a critical value for deposition ( $\tau_d$ ). The erosion ( $E_m$ ) and deposition ( $D_m$ ) fluxes are calculated as:

$$E_m = E_0 \left( \frac{\tau_b}{\tau_{e,fl}} - 1 \right) \quad \text{for } \tau_b \geq \tau_{e,fl} \quad (4.17a)$$

$$E_m = 0 \quad \text{for } \tau_b < \tau_{e,fl} \quad (4.17b)$$

$$D_m = c_m w_m \left( 1 - \frac{\tau_b}{\tau_d} \right) \quad \text{for } \tau_b \leq \tau_d \quad (4.18a)$$

$$D_m = 0 \quad \text{for } \tau_b > \tau_d \quad (4.18b)$$

where  $E_0$  is the erosion constant ( $\text{kg m}^{-2} \text{s}^{-1}$ ). Assuming values for  $\tau_d$  smaller than  $\tau_{e,fl}$  means that deposition and erosion are mutually exclusive. This hypothesis may fail to reproduce field data (Sanford & Halka, 1993). A continuous deposition approach, similar to that commonly used for sand, can be applied by defining an infinitely large  $\tau_d$ .

### Active layer

The net upward flux of suspended sand ( $F_z = wc_s - w_s c_s + \overline{w'c'_s}$ ) depends on the suspended sand concentration ( $c_s$ ), vertical velocity ( $w$ ), sand settling velocity ( $w_s$ ), and vertical diffusive flux ( $w'c'_s$ ). Evaluating the upward flux at a small distance above bed ( $\delta$ ), the vertical velocity  $w$  can be neglected. Assuming steady state ( $F_\delta = 0$ ), the concentration of suspended sediment will reach an equilibrium condition ( $c_{\delta e} = \overline{w'c'_s}/w_s$ ). Considering that the disequilibrium remains mild, the same relation holds for unsteady state as well (Garcia & Parker, 1991). Therefore, the net upward flux at a small distance above bed is given by  $F_\delta = w_s(c_{\delta e} - c_\delta)$ , where  $w_s c_{\delta e}$  can be considered as the erosion flux and  $w_s c_\delta$  as the deposition flux.

The equilibrium concentration ( $c_{\delta e}$ ) can be estimated by empirical equations available in the literature (Garcia & Parker, 1991). A main conflict in the available relations is the definition of the reference level ( $\delta$ ) - the distance above bed where  $c_{\delta e}$  is determined. Above  $\delta$ , the transport of sediment particles is assumed to be in suspension. A value for  $\delta$  of two grain diameters of the bed material was suggested by Einstein (1950), which was assumed by others researchers (e.g., Engelund & Fredsoe, 1976). Other relations adopt  $\delta$  as function of the equivalent roughness height ( $k_s$ ) or a fraction of depth (e.g., Smith & McLean, 1977; van Rijn, 1984). Amoudry and Liu (2010) verified the equilibrium concentration equations derived for different  $\delta$  values against the results of a sheet flow model, finding a good agreement for the Zyserman and Fredsoe (1994) equation for  $\delta = 2d$ . On the other hand, a significant disagreement was found for the magnitude and phase of the van Rijn (2007b) equation results ( $\delta \geq 1cm$ ), justified by  $\delta$  being in the suspended region. Further above the bed, sediment particles are kept in suspension by turbulence instead of grain-grain collisions. Therefore, the equilibrium concentration is computed following the equation of Zyserman and Fredsoe (1994):

$$c_{\delta e}^{(l)} = \frac{0.331 (\theta - \theta_{cr}^{(l)})^{1.75}}{1 + \frac{0.331}{0.46} (\theta - \theta_{cr}^{(l)})^{1.75}} \quad (4.19)$$

The deposition flux ( $D_s^{(l)}$ ) of the different sand classes is a function of the settling velocity and concentrations in the near bed layer:

$$D_s^{(l)} = w_s^{(l)} c_s^{(l)} \quad (4.20)$$

For consistency in the net upward flux calculations, deposition and erosion fluxes must be computed at the same distance above the bed. Thus, to compute the erosion flux of sand classes ( $E_s^{(l)}$ ), the equilibrium concentration is extrapolated to the middle of the near bed layer following the Rouse profile (Rouse, 1937):

$$c_e^{(l)} = c_{\delta e}^{(l)} \left[ \frac{\delta^{(l)}(h-z)}{z(h-\delta^{(l)})} \right]^b \quad (4.21)$$

$$E_s^{(l)} = w_s^{(l)} c_e^{(l)} \quad (4.22)$$

where  $\delta^{(l)}$  is the reference level ( $\delta^{(l)} = 2d^{(l)}$ );  $h$  is the water depth,  $b = w_s^{(l)}/(0.4u_*)$  and  $z$  is the distance above bed. The hypothesis assumed is that the net upward flux in the middle of the near bed layer is equal to the net upward flux at the bed.

The erosion and deposition rates of mud in the active layer (Eqs. 4.23 and 4.24) are calculated similarly as for the fluid mud layer. However, the critical erosion shear stress in the active layer is higher than in the fluid mud layer and the erosion flux in the active layer ( $E_{m,a}$ ) is multiplied by the mud content ( $p_m$ ). In fully cohesive beds, as clusters are eroded instead of individual particles, the erosion flux of sand particles is also computed with Eq. 4.23, considering the sand class percentage instead of the mud content.

$$E_{m,a} = E_0 \left( \frac{\tau_b}{\tau_{e,m}} - 1 \right) p_m \quad \text{for } \tau_b \geq \tau_{e,m} \quad (4.23a)$$

$$E_{m,a} = 0 \quad \text{for } \tau_b < \tau_{e,m} \quad (4.23b)$$

$$D_{m,a} = D_0 \left( 1 - \frac{\tau_b}{\tau_d} \right) \quad \text{for } \tau_b \leq \tau_d \quad (4.24a)$$

$$D_{m,a} = 0 \quad \text{for } \tau_b > \tau_d \quad (4.24b)$$

here  $D_{m,a}$  is the deposition rate of mud in the active layer and  $D_0$  is the deposition constant, considered as the deposition rate in still water just before reaching gelling concentrations. Based on data on concentrations and settling velocities in the hindered settling regime (summarized in Winterwerp, 2002), values of  $D_0$  are in the range of  $10^{-4}$  to  $10^{-2} \text{ kg m}^{-2} \text{ s}^{-1}$ .

### 4.3.8 Bed evolution

The mass balance in the active layer for each sand class ( $M_s^{(l)}$ ) and mud ( $M_m$ ) can be expressed by:

$$\frac{1}{A} \frac{\partial M_s^{(l)}}{\partial t} + \frac{\partial q_{bu}^{(l)}}{\partial x} + \frac{\partial q_{bv}^{(l)}}{\partial y} = E_s^{(l)} - D_s^{(l)} \quad (4.25a)$$

$$\frac{1}{A} \frac{\partial M_m}{\partial t} = E_{m,a} - D_{m,a} \quad (4.25b)$$

in which  $A$  is the horizontal area of the grid cell. A first order upwind scheme is applied to solve Eq. 4.25a. As bed load transport is only considered for sand particles, the mass balance for mud is a simple balance between erosion and deposition fluxes (Eq. 4.25b). The boundary condition at open points can be set as a null gradient or null value. After the mass balance calculation, the bed evolution is computed as:

$$\Delta z_b = \frac{\Delta M}{A \rho_s (1 - \phi)} \quad (4.26)$$

where  $\Delta M$  is the total sediment mass variation. The bathymetry is updated with a specific time step, which can be set as equal or as a multiple of the morphological model time step. In the latter case, the bathymetry increment is accumulated.

The rate of morphological changes can be speed-up through the multiplication of sediment fluxes by an acceleration factor. Thus, the simulation of the bed evolution for long time periods can be computationally feasible, which would be impractical otherwise. The upper value for the acceleration factor will vary according to the system dynamics. A factor in the range of 10 to 100 can usually be safely applied (Lesser, 2009), whereas higher factors can be applied in less dynamic systems.

### 4.3.9 Consolidation

Methods with different complexity levels have been proposed in the literature for simulating the consolidation process, from the simple division of the sediment column into layers characterised by different densities or shear strengths, to more comprehensive approaches that describe the sedimentation of highly concentrated suspended sediments and self-weight consolidation (Toorman, 1999; Grasso et al., 2015). These approaches require calculating the hydraulic permeability and effective stress, demanding high spatial and temporal resolutions to satisfactorily represent the

fluid-bed interface (Van & Pham Van Bang, 2013; Chauchat et al., 2013). Currently, this degree of detail seems computationally infeasible, when considering modelling sediment transport and morphological processes in large-scale domains, such as estuarine systems.

The approach applied here is based on the assumption that consolidation effects can be approximated by a first-order equation (Sanford, 2008), increasing the dry density of cohesive sediments ( $\rho_{dry}$ ):

$$\frac{d\rho_{dry}}{dt} = \left(\frac{\rho_1 - \rho_{dry}}{\rho_1 - \rho_0}\right) [k_{c1}(\rho_1 - \rho_{dry}) - k_{c2}(\rho_\infty - \rho_{dry})] + k_{c2}(\rho_\infty - \rho_{dry}) \text{ if } \rho_{dry} < \rho_1 \quad (4.27a)$$

$$\frac{d\rho_{dry}}{dt} = k_{c2}(\rho_\infty - \rho_{dry}) \text{ if } \rho_{dry} \geq \rho_1 \quad (4.27b)$$

where  $\rho_0$  is the initial dry density,  $k_{c1}$  is the consolidation rate for the permeability regime,  $k_{c2}$  is the consolidation rate for the effective stress regime,  $\rho_1$  is the dry density in which the permeability regime ends, and  $\rho_\infty$  is the maximum possible dry density. The increase of  $\rho_{dry}$  due to consolidation affects the sediment porosity and the resistance to erosion, as well as the sediment column thickness.

## 4.4 Test cases

Six test cases were simulated to verify the model equations and numerical implementation in the MOHID modelling system. The results were compared with analytical solutions or experimental data, assessing the model's capacity to simulate the suspended and bed load transport, effects of consolidation, morphological evolution, and sediment distribution in real systems.

### 4.4.1 Steady uniform flow

In this test case, the model results under equilibrium flow conditions are compared with existing analytical solutions for velocity and suspended sediment concentrations. A uniform open channel with dimensions of 100 m length by 1 m width by 10 m depth was defined as the model domain. A constant depth-mean velocity of 1 m s<sup>-1</sup> was imposed at the upstream boundary, whereas boundary conditions of a null gradient were defined for sediment concentrations. The k- $\epsilon$  turbulence-closure model was used and morphological changes were not allowed to occur. The horizontal grid resolution was defined as 1 m. Four simulations were done to evaluate model results with a different number of evenly distributed vertical layers (10, 20, 40, and 80 layers).

The computed profiles converged when increasing the number of layers and resulted in close agreement with the analytical solutions (Figure 4.3), even when considering only 10 vertical layers. Assuming the logarithmic profile, the analytical solution for velocity is  $u(z) = u_* / k \ln(z/z_0)$ , where

the shear velocity  $u_* = k\bar{u}/[\ln(h/z_0) - 1 + z_0/h]$ ,  $k = 0.41$  is the von Kármán's constant,  $z_0$  is the bed roughness length, and  $\bar{u}$  is the depth-mean velocity. Considering a constant settling velocity and a parabolic sediment mixing profile, the Rouse profile (Rouse, 1937) is a solution for the advection diffusion equation under equilibrium conditions. This test case demonstrated that the model is able to simulate the transport of suspended sediment.

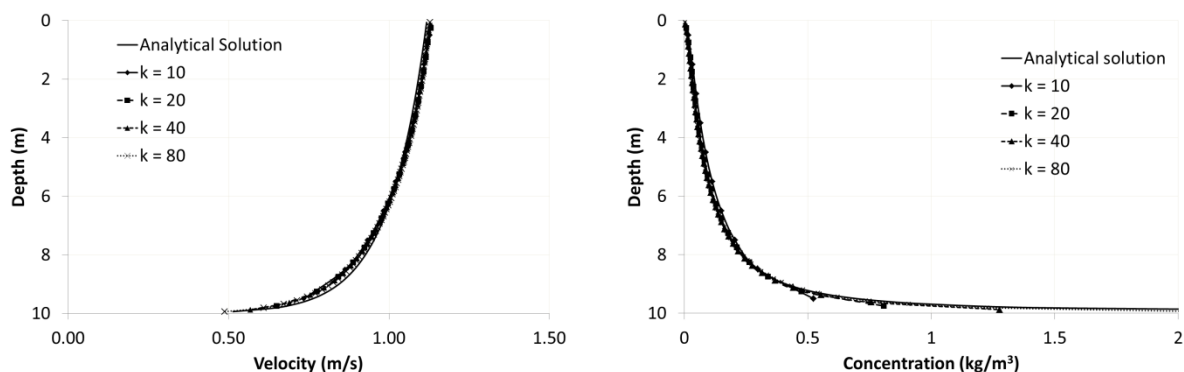


Figure 4.3 – Equilibrium profiles of velocity (left) and suspended sediment concentration (right) computed by using different numbers ( $k$ ) of vertical layers compared with analytical solutions.

#### 4.4.2 Bed load for non-cohesive sand-mud mixtures

The bed load formulation for non-cohesive sand-mud mixtures was verified with data from the experimental analysis of Murray (1977). The experiment was performed considering a coarse sand fraction ( $d_{50} = 0.8$  mm) with 0%, 10%, and 18% of mud content. The simulation results were compared with the results found by Murray (1977) for bed load transport rate versus bed shear stress (Figure 4.4). The coefficients for the dimensionless bed load transport equation (Eq. 4.10) were defined as  $k_{\phi_1} = 8$ ,  $k_{\phi_2} = 0.35$ , and  $k_{\phi_3} = 1.5$ , based on the range of values found in the literature (Table 4.1) and the results of calibration. Realistic results for the different mixtures were achieved with a coefficient  $\beta$  of 2.2 in the critical shear stress equation (Eq. 4.7), indicating the model's capacity to simulate the effects of mud content on sand transport.

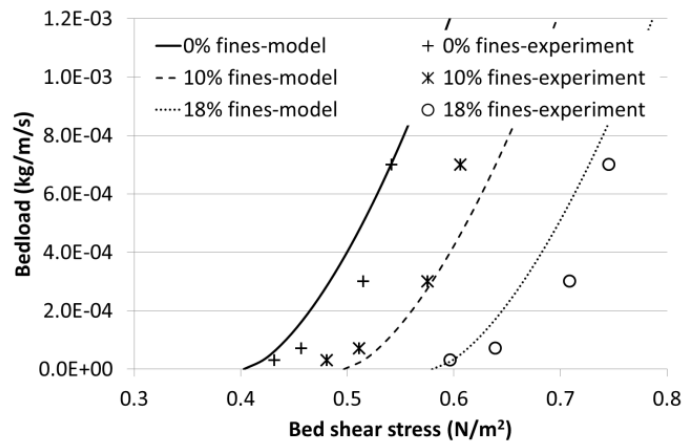


Figure 4.4 – Bed load for non-cohesive sand-mud mixtures. Results of bed load transport versus bed shear stress for different mud content compared with the experimental analysis of Murray (1977).

#### 4.4.3 Consolidation column

In this test case, the experiment performed by Toorman and Berlamont (1993) in a 2 m deep settling column was simulated to test the method used for simulating the consolidation process. The initial bulk density of the slurry was  $1050 \text{ kg m}^{-3}$ , being measured again after 0.11, 0.92, and 14 d. For the simulation, the bottom column was uniformly divided into 20 layers composed of mud with an initial dry density of  $80.3 \text{ kg m}^{-3}$  (bulk density of  $1050 \text{ kg m}^{-3}$ ). The parameters used for simulating the density increase (Eq. 4.27) were defined as  $k_{c1} = 0.9 \text{ d}^{-1}$ ,  $k_{c2} = 0.002 \text{ d}^{-1}$ ,  $\rho_1 = 220 \text{ kg m}^{-3}$ , and  $\rho_\infty = 650 \text{ kg m}^{-3}$ , based on Sanford (2008) and model calibration.

The model was capable of properly representing the top and average bulk densities measured during the experiment (Figure 4.5), as well as the decrease in the bottom column height due to water expulsion. However, more complex approaches are needed to represent the density fronts in detail, which could greatly increase the computational effort, becoming impractical for modelling studies in real environments. The experiment duration was extended to assess the consolidation effects after longer periods. The bulk densities obtained after a period of 1 year and 10 years were in accordance to those cited in the literature for consolidated mud (e.g., van Rijn, 2012).

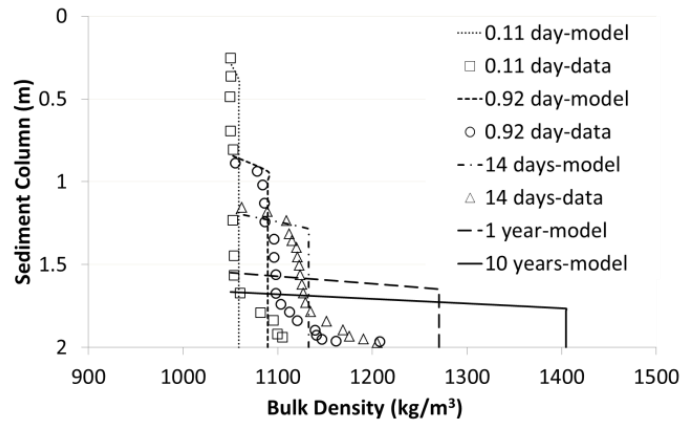


Figure 4.5 – Consolidation of cohesive sediments in a 2 m deep settling column. Model results of bulk density for 0.11, 0.92, and 14 days compared with the experimental data of Toorman and Berlamont (1993). The experiment duration was extended to assess model results after longer periods (1 year and 10 years).

#### 4.4.4 Trench migration

In this test case, the migration of a trench in a flume was simulated, according to the experiments described in van Rijn (1987). The flume dimensions were 30 m length by 0.5 m width by 0.39 m depth (apart from the trench location). The trench geometry is presented in Figure 4.6 for a side slope of 1:3. Another two experiments were performed for trenches with side slopes of 1:7 and 1:10. A constant flow velocity ( $0.51 \text{ m s}^{-1}$ ) was imposed upstream of the trench. The bed was composed of well-sorted sand ( $d_{50} = 160 \text{ }\mu\text{m}$  and  $d_{90} = 200 \text{ }\mu\text{m}$ ). The effective bed roughness was determined as  $k_s = 0.025 \text{ m}$  by analysing near-bed velocities upstream of the trench. The settling velocity was estimated to be in the range of  $0.011$  to  $0.015 \text{ m s}^{-1}$ , based on the size of suspended sediment particles and water temperature. Profiles of velocity and sediment concentration were measured at the beginning of the experiment. The trench migration downstream was determined after 15 h.

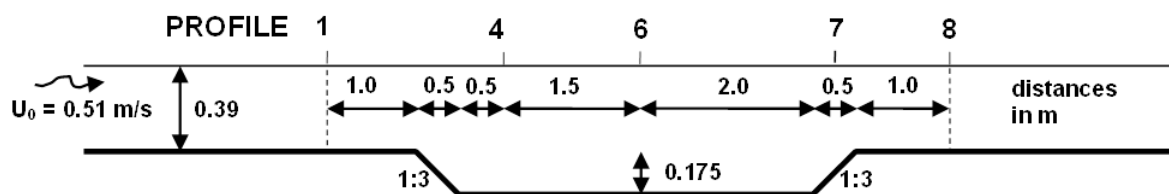


Figure 4.6 - Geometry of the flume and trench including the locations of the different measured profiles (adapted from van Rijn, 1987)

A two-dimensional in the vertical (2DV) model was implemented to simulate these experiments, with a grid resolution of 0.1 m in the horizontal and 15 sigma layers evenly distributed in the vertical. The simulations were done with one class of sand ( $d_{50} = 160 \mu\text{m}$ ) and a representative settling velocity of  $0.013 \text{ m s}^{-1}$ . The  $k-\epsilon$  turbulence-closure model was used to compute the vertical viscosity, with the MOHID default parameterization. The bed roughness length was obtained by the expression  $z_0 = k_s / 30$  (0.833 mm). At first, the model was warmed-up considering the bed as motionless. The results of velocity and sediment concentration after the warm-up were compared with experimental data (Figure 4.7). Afterwards, the bed was allowed to evolve, considering the bed load equation of Meyer-Peter and Müller (1948). To evaluate the morphological acceleration scheme, four simulations were done with different acceleration factors (1, 20, 100, and 300). Thus, the simulation time was reduced from 15 h to 45, 9, and 3 min, representing a significant computational gain without larger effects on the model results (Figure 4.8A).

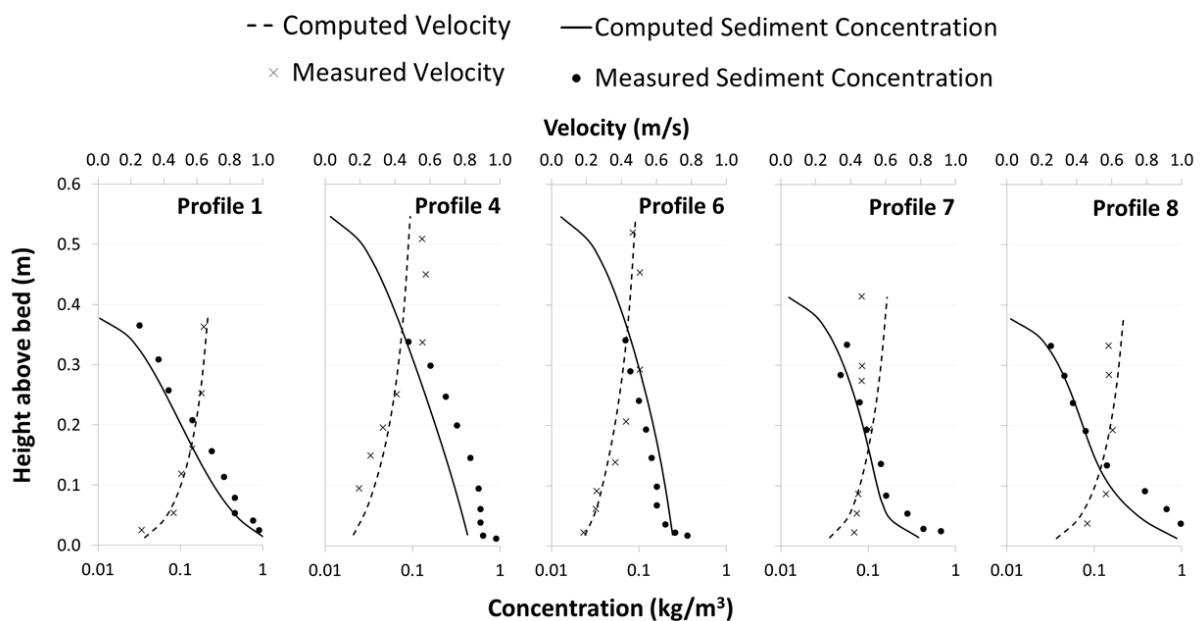


Figure 4.7 - Measured and computed profiles of velocity and sediment concentration at the beginning of the experiment (before bed changes)

The observed trench migration was well represented by the model. However, an overestimation on trench filling up to 4 cm was verified, which can be associated with inaccuracies observed in the velocity profiles. At the end of the trench, computed velocities near the bed were lower than measured values (Figure 4.7), causing an underestimation of erosion and, consequently, lower sediment transport. Further simulations demonstrated that the bed load was the main cause responsible for the trench migration, whereas the suspended sediment transport was the main cause responsible for the trench filling (Figure 4.8B). A better parameterization of the  $k-\epsilon$  turbulence-closure model may contribute to improved results. Despite these issues, the overall model results are similar to those obtained by applications of other morphological models for the same experiment (Lesser et al., 2004; Warner et al., 2008; Pinto et al., 2012).

The experiments for the trenches with side slopes of 1:7 and 1:10 were also simulated and bed level results compared with measured data (Figure 4.8C and Figure 4.8D). To assess model sensitivity, different simulations were done considering the bed load equation of Meyer-Peter and Müller (1948) and the bed load equation of Soulsby and Damgaard (2005). Minor changes were observed in these experiments. Nevertheless, these differences could become important for longer simulations. The trench filling overestimation in these simulations reduced to up 3 cm, indicating that the model may respond better in smoother slopes, which are most common in nature for movable beds.

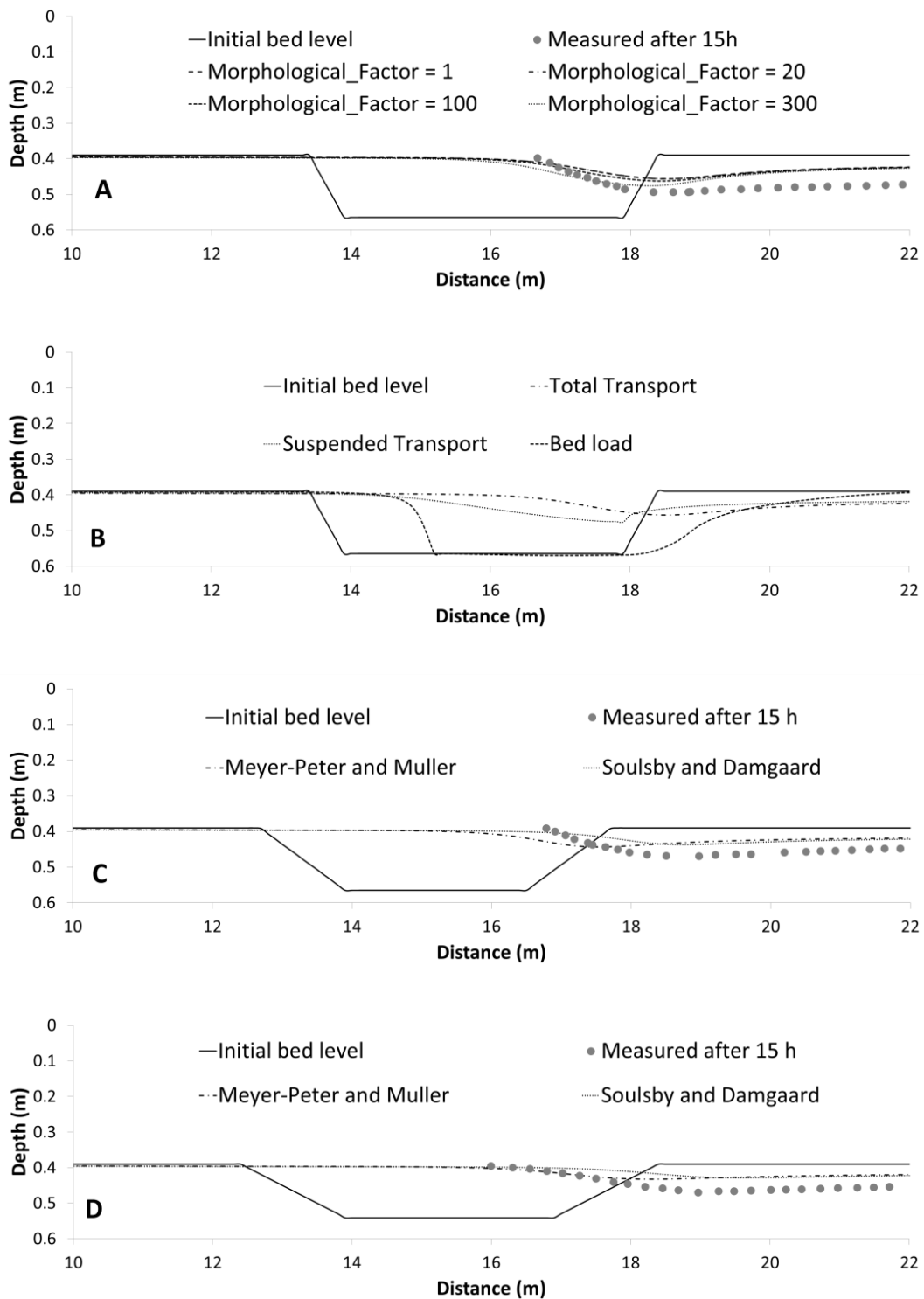


Figure 4.8 – Trench migration in a flume. Figure 4.8A - Results with morphological acceleration factors varying from 1 to 300. Figure 4.8B - Contribution of bed load and suspended load to the final bed profile. Figure 4.8C and Figure 4.8D - Results for the trenches with side slopes of 1:7 and 1:10, respectively, considering the bed load equation of Meyer-Peter and Müller (1948) and the bed load equation of Soulsby and Damgaard (2005).

#### 4.4.5 Schematic estuary

The morphological evolution of a schematic estuary was simulated to evaluate the model performance in terms of expected patterns and numerical robustness. The model was run for 3 years with an acceleration factor of 100, representing 300 years of morphological evolution. The initial bathymetry was defined as uniform (1 m deep), with the exception of the upper estuary (intertidal zone), where constant discharges ( $500 \text{ m}^3 \text{ s}^{-1}$ ) were placed on both sides. The tidal level was imposed at the open boundary by defining the principal lunar semi-diurnal ( $M_2$ ) tidal constituent typical of a mesotidal coast (1 m of amplitude). The model domain encompasses an area of 2 km x 5 km, with a horizontal grid resolution of 100 m x 100 m and five sigma layers evenly distributed in the vertical. The bottom sediments were composed of five sand classes uniformly distributed, with diameters of 0.2, 0.6, 1.0, 1.4, and 1.8 mm. The bottom column was initialized with a 100 m thick layer to allow erosion until an equilibrium condition was reached.

The initial and resulting bathymetries after a period of 10, 100, 200, and 300 years of morphological evolution are shown in Figure 4.9. The results present the expected patterns with the development of channels and bathymetry stabilisation in equilibrium with the hydrodynamics. The velocity vectors represent the middle of an ebb tide. At first, peak intensities greater than  $2 \text{ m s}^{-1}$  were obtained in the most constrained zone representing the inlet channel, decreasing to values lower than  $1 \text{ m s}^{-1}$  after the bathymetry stabilisation.

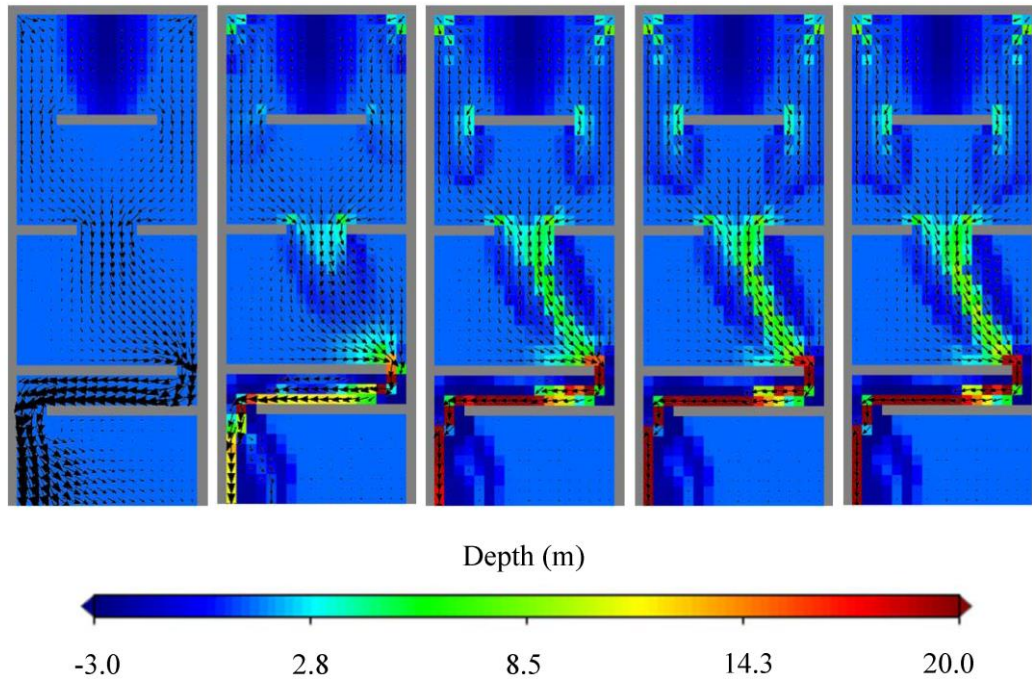


Figure 4.9 – Morphological evolution of a schematic estuary. The initial and resultant bathymetries after a period of 10, 100, 200, and 300 years are shown from the left to right. The initial bathymetry was defined as uniform (1 m deep), with the exception of the upper estuary. Negative depths represent intertidal zones that may be covered in high tides and uncovered in low tides. Channels with maximum depths near 20 m were generated for the given hydrodynamic conditions and sand diameters.

#### 4.4.6 Sediment distribution in the Tagus Estuary

In this test case, the model's capability for generating realistic sediment distributions was investigated. The availability of bed composition data is usually a constraint for the application of morphological models. This limitation can be overcome by considering a warm-up run in which sediment fractions are distributed according to the local hydrodynamic conditions. The computed sediment distribution can be used as the initial condition for further predictions of morphological developments (Van der Wegen et al., 2011). The simulation was performed for the Tagus Estuary, considering a two-dimensional depth-averaged (2DH) model previously applied to study cohesive sediment dynamics (Franz et al., 2014a).

The initial distribution of cohesive sediments was obtained from the results presented in Franz et al. (2014a). The cohesive sediments were considered to be at first in the fluid mud layer, depositing into the active layer with a rate of  $10^{-3} \text{ kg m}^{-2} \text{ s}^{-1}$ . In this study, five fractions of sand with diameters of 0.1 (very fine), 0.2 (fine), 0.4 (medium), 0.8 (coarse), and 1.5 mm (very coarse) were included. The sand fractions, from the finest to the coarsest, were initially distributed in the bottom column in five

layers with 1.0 m of thickness. Maximum and minimum values for layer thickness were defined as 1.1 and 0.1 m, respectively. An additional layer, initially empty, was included in bottom geometry to allow segregation of sediments in depositional zones.

The model was run for a 30 day period considering a morphological acceleration factor of 100. Although bed level changes were not allowed during this simulation, the morphological acceleration factor was useful to speed up the changing rate of bed composition. The sediment transport was affected by the interactions among sediment fractions and the consolidation process. The results were compared with field data presented in Canário and Vale (2007). In general, the simulated sediment distribution is in accordance with the observed patterns (Figure 4.10). Differences may be related to the horizontal grid resolution (200 m x 200 m) and limitations of a 2DH model. As the waves' action was disregarded in this study, the bed composition in the adjacent coastal zone cannot be evaluated. This test case showed the model potential to generate realistic sediment distributions in natural systems with limited data.

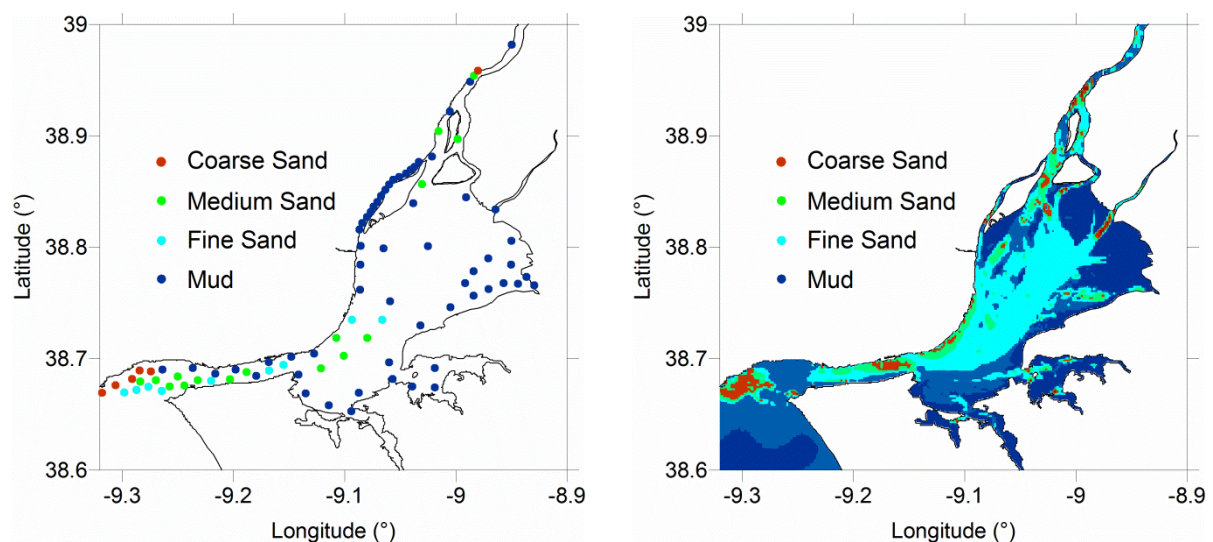


Figure 4.10 – Sediment distribution in the Tagus Estuary. Data (left) from Canário and Vale (2007) and model results (right) after a warm-up run in which sediment fractions were distributed according to the local hydrodynamic conditions.

## 4.5 Conclusions

The test cases demonstrated the model's capacity to simulate the transport dynamics of cohesive and non-cohesive sediments. The applied empirical or simplified physical relations, necessary to represent small-scale (sub-grid) processes, were proven to give satisfactory results. Thus, small-scale processes, such as consolidation, can be taken into account in large-scale simulations. The effects of sediment mixtures on the motion of individual sediment fractions also contribute to a more realistic representation of natural systems. The speed up of morphological changes by an acceleration factor was confirmed to be reliable. Therefore, modelling bed evolution for long time periods was confirmed to be feasible.

Due to the diverse processes and sediment types considered, the model can be applied to different systems, such as estuaries, bays, reservoirs, and rivers. The Tagus Estuary test case verified the model's capacity for generating a realistic sediment distribution based on the local hydrodynamic conditions. This is important for providing accurate initial conditions for further prediction of morphological developments, as the availability of bed composition data is usually a constraint. On a first impression, the morphological model described here with multiple sediment classes can be seen to be difficult to apply. However, the basic inputs are only the diameters of sand classes, as other parameters can be directly computed by the model, such as settling velocities and critical shear stresses.

In the light of modelling sediment dynamics, relevant developments in the MOHID modelling system were made in this work. Nevertheless, the test cases showed in this paper are only a preliminary demonstration of model potential. Taking into consideration the modular structure of the MOHID modelling system, the morphological model can be linked to other existing models to assess, for instance, the evolution of water properties (e.g., nutrients) or heavy metals (e.g., mercury) in the sediment column and exchanges with the water column. Future research can address the movement of fluid mud by gravity and the biological effects on sediment erosion resistance. The mathematical formulation and test cases considering the influence of waves on sediment transport will be addressed in future research.



# Chapter 5 Modelling of sediment transport and morphological evolution under the combined action of waves and currents

*The material on which this chapter is based has been previously published in Franz, G., Delphey, M.T., Brito, D., Pinto, L., Leitão, P., Neves, R, 2017. Modelling of sediment transport and morphological evolution under the combined action of waves and currents. Ocean Science Discussion, in review.*

## **Abstract**

Coastal defence structures are often constructed to prevent beach erosion. However, poorly designed structures may cause serious erosion problems in the downdrift direction. Morphological models are useful tools to predict such impacts and assess the efficiency of defence structures for different scenarios. Nevertheless, morphological modelling is still a topic under intense research effort. The processes simulated by a morphological model depend on model complexity. For instance, undertow currents are neglected in coastal area models (2DH), which is a limitation for simulating the evolution of beach profiles for long periods. Model limitations are generally overcome by predefining invariant equilibrium profiles that are allowed to shift offshore or onshore. A more flexible approach is tested in this paper, which can be generalised to 3D models. The present work is based on the coupling of the MOHID modelling system and SWAN wave model. The impacts of different designs of detached breakwaters and groynes were simulated in a schematic beach configuration following a 2DH approach. The results of bathymetry evolution are in agreement with the patterns found in the literature for several existing structures. The model was also tested in a 3D test case to simulate the formation of sandbars by undertow currents. The findings of this work confirmed the applicability of the MOHID modelling system to study sediment transport and morphological changes in coastal zones under the combined action of waves and currents. The same modelling methodology was applied to a coastal zone (Costa da Caparica) located at the mouth of a mesotidal estuary (Tagus Estuary, Portugal) to evaluate the hydrodynamics and sediment transport in calm water conditions and during events of highly energetic waves.

Keywords: coastal morphodynamics; detached breakwaters; groynes; sandbars; MOHID modelling system; SWAN wave model, Costa da Caparica

## 5.1 Introduction

The morphological features of the coastal zone depend on the sediment characteristics and the combined action of waves and currents. Wind waves are the main energy source for most beaches. Particularly in the surf zone, waves may induce considerable changes in mean sea level and strong currents (Longuet-Higgins, 1970a, 1970b, 1983). The pattern of surf zone currents varies with the obliquity of waves approaching the shore as well as with bathymetric heterogeneities, leading to longshore and rip currents. Sediment is usually carried shoreward during low wave conditions, mainly due to the asymmetry of waves in shallow waters (Myrhaug et al., 2004). The sediment accumulated during these periods may be eroded very rapidly under high wave conditions during a major storm. Following these energetic events, the bottom profile may recover its initial shape only if the longshore transport of sediment during the storm was low. Different structures such as breakwaters and groynes can prevent the along-coast movement of sediment (e.g., Dally and Pope, 1986). However, serious erosion problems in the downdrift direction may arise from the construction of these structures. Morphological models are useful tools to assess the impact of defence structures, enabling us to consider different wave conditions and structure designs.

The complexity of morphological models ranges from coastal profile models to two- or three-dimensional models. Actually, morphological models are a set of different models or modules, depending on the chosen approach. Here the focus is set on the coupling of a spectral wave model with a phase-averaged hydrodynamic and sediment transport model. Spectral wave models offer a representation of the physical processes related to the generation, propagation and dissipation of waves (e.g., Booij et al., 1999). The wave-induced forces computed by a wave model can be provided to a hydrodynamic model in order to simulate wave-related phenomena, such as wave set-up, wave-induced currents and mixing. On the other hand, the hydrodynamic model can return water levels and currents to the wave model (e.g., Warner et al., 2008). Additional processes can be considered in the hydrodynamic model, such as wind action, tidal motion, and river discharges. The transport of suspended sediment may be simulated by an advection/diffusion model. The mechanism of erosion/deposition of sediments is controlled by the bed shear stress induced by currents and waves. The bathymetry evolution resulting from the total sediment transport (suspended load and bed load) affects the patterns of currents and waves. Due to the interdependence of the physical processes involved in sediment dynamics, all of these models must be coupled.

The hydrodynamics inside the surf zone is influenced by important three-dimensional effects. Due to the absence of three-dimensional processes (e.g., undertow), coastal area models (2DH) fail to reproduce a consistent evolution of beach profiles for long periods. This shortcoming can be

overcome by predefining invariant equilibrium profiles. In this case, the equilibrium profile only shifts offshore or onshore depending on the overall sediment balance along the profile, similarly to a coastal profile model (e.g., Kriebel and Dean, 1985; Kristensen et al., 2013). As the sediment transport in the swash zone is usually neglected in large-scale 2DH models, this approach also has the advantage of updating the shoreline position. However, limitations arise when a structure is present in the surf zone. Moreover, the processes responsible for sandbar evolution are not considered. Attempts to simulate sandbar dynamics have been performed generally with cross-shore bi-dimensional (2DV) and quasi-3D models (e.g., Drønen and Deigaard, 2007; Ruessink et al., 2007). Nevertheless, the proper reproduction of sandbar migration is still an active topic of research (e.g., Dubarbier et al., 2015). Inaccuracies in the cross-shore sediment transport may degrade the coastal profile, which is a restriction for the simulation of long-term morphological evolution.

In this work, we test a more flexible approach to overcome the 2DH model limitations in order to simulate morphological evolution for long periods. Instead of fixing an equilibrium profile to update the bathymetry and shoreline position, we defined a maximum slope that when surpassed generates sediment transport in the downslope direction. Thus, rather than extrapolating erosion or deposition fluxes over the entire profile, only individual grid cells are affected. This approach may be more appropriate in order to consider the effect of non-uniform grain-size distributions on the overall sediment transport, through morphological models that account for multiple sediment fractions. Grain-size sorting is generally observed along the cross-shore beach profile, as well as in the longshore beach direction (Komar, 1998). Furthermore, the method can be generalised to 3D models for a better representation of sandbar slopes and to update the shoreline position.

This chapter is divided into five sections. A brief description of the effect of waves in the nearshore hydrodynamics and sediment transport is given in Section 5.2. The numerical modelling approach is presented in Section 5.3. The methodology was verified for different test cases (Section 5.4). Firstly, the morphological evolution of a schematic beach was evaluated for different designs of coastal defence structures (detached breakwaters and groynes) following a 2DH model configuration. The model was applied later in a 3D configuration for the same schematic beach to verify the development of sandbars. Finally, the numerical modelling methodology was applied to assess the hydrodynamics and sediment transport under extreme wave conditions in a coastal zone (Costa da Caparica) located at the mouth of a mesotidal estuary (Tagus Estuary, Portugal). The main conclusions found from these test cases are discussed in Section 5.5.

## 5.2 Background

The effect of breaking waves on the mean sea level (wave set-up) is known since the laboratory measurements performed by Saville (1961), confirmed further by Bowen et al. (1968). This tilt of the mean sea level is explained by the horizontal flux of momentum carried by waves, or equivalently by the radiation stress, a vertically integrated momentum flux whose gradient balances the wave set-up (Longuet-Higgins and Stewart 1962, 1964). In the surf zone, wave heights and orbital velocities decrease towards the shore due to wave breaking. As a consequence, the radiation stress also decreases, resulting in a force directed towards the shore. This force is balanced by a hydrostatic pressure gradient that increases the mean sea level onshore.

Breaking waves can also drive strong currents in the surf zone, which are important for sediment transport and morphological evolution in the coastal zone. The horizontal mass transport associated with waves, or Stokes drift, is oriented shoreward and vertically sheared, being more intense at the surface (e.g. Arduin et al., 2008). As a result, mass conservation in the nearshore is satisfied by a seaward transport in the lower part of the water column, called undertow, which has an important role in sandbar formation. The undertow is strongest in steep beaches and may be insignificant for moderate beach slopes, where circulation tends to break up into rip currents (Longuet-Higgins, 1983). Also, obliquely breaking waves generate longshore currents (Longuet-Higgins, 1970a, 1970b) and, consequently, longshore sediment transport. Although nearshore sediment dynamics are dominated by wave action, tidal motion can also play an important role, alternately moving the breaker zone and shoreline position shoreward and seaward, which may prevent the development of longshore bars in the surf zone (e.g., Levoy et al., 2000).

## 5.3 Numerical model

The present work is based on the coupling of the MOHID modelling system (Leitão, 2003; Leitão et al., 2008) and the SWAN wave model (Booij et al., 1999). The MOHID code organisation follows an object oriented strategy that permits the integration of different scales and processes. Herein, the focus is given to the hydrodynamics and sediment transport in the nearshore area. Thus, we considered the processes related to the hydrodynamics, turbulence, advection/diffusion of suspended sediment, erosion/deposition of sediments, bed load sediment transport and morphological evolution. A brief description of the most important aspects of the hydrodynamic model for this work is presented in this section, followed by the main novelties implemented in the MOHID code: a new method to calculate the bed load transport under the combined effect of currents and waves; and a bed slope correction considered to overcome the 2DH model limitations and to update the shoreline.

The SWAN wave model represents the processes of wave generation, propagation, refraction, shoaling, nonlinear (quadruplet and triad) wave-wave interactions, and dissipation (whitecapping, bottom friction, and depth-induced breaking). More information can be found in the documentation of the SWAN wave model (<http://swanmodel.sourceforge.net/>). Both MOHID and SWAN can be run with multiple processors using shared (OpenMP) or distributed (OpenMPI) memory architectures. In this work, we implemented MPI directives in the MOHID module responsible for the calculations of bed load transport and morphological evolution (Sediment module), which can consider multiple sediment classes. In addition to speeding up morphological changes by an acceleration factor, this new development reduces the computational time required for modelling bed evolution over long time periods.

### 5.3.1 Hydrodynamic module

The MOHID hydrodynamic module solves the Navier-Stokes equations, considering the hydrostatic, Boussinesq and Reynolds approximations (Martins, 2000, Leitão, 2003):

$$\begin{aligned} \frac{\partial}{\partial t} \int_V \vec{v}_H dV = & - \oint_A \vec{v}_H (\vec{v} \cdot \vec{n}) dA + \oint_A v_T (\vec{\nabla}(\vec{v}_H) \cdot \vec{n}) dA - \\ & \frac{1}{\rho} \oint_A p \cdot \vec{n}_H dA + \int_V 2\vec{\Omega} \times \vec{v}_H dV + \vec{F} \end{aligned} \quad (5.1)$$

where  $V$  represents the control volume,  $\vec{v}_H = (u, v)$  the horizontal velocity vector,  $\vec{v} = (u, v, w)$  the velocity vector,  $\vec{n}$  the normal vector to the bounding surface ( $A$ ),  $\vec{n}_H$  the normal vector related to the horizontal plane,  $v_T$  the turbulent viscosity,  $\rho$  the water density,  $p = g \int_z^\eta \rho dz + p_{atm}$  the water pressure,  $g$  the gravitational acceleration,  $p_{atm}$  the atmospheric pressure,  $\eta$  the water level,  $\vec{\Omega}$  the earth rotation vector, and  $\vec{F}$  the external forces, which include the wave-induced force (gradient of the radiation stress) computed by the wave model. The wave-induced force was considered in the MOHID hydrodynamic module in previous studies to compute the effects of waves on sea level (Malhadas et al., 2009), water renewal in a coastal lagoon (Malhadas et al., 2010), and coastal water dispersion in an estuarine bay (Delpey et al., 2014).

The spatial discretization is performed by following the finite volume method. The water level and vertical velocity are computed through the continuity equation integrated over the entire water column or applied to each control volume, respectively. The equations are solved through the Alternating Direction Implicit (ADI) method in an Arakawa C-grid structure. A generic vertical discretization allows implementing different types of vertical coordinates (e.g, Sigma or Cartesian)

(Martins, 2001). The turbulent viscosity is computed differently for the horizontal and vertical directions. The horizontal turbulent viscosity is defined as a constant value, based on the grid resolution and a reference velocity, or as a function of horizontal velocity gradients, based on Smagorinsky (1963). The vertical turbulent viscosity is computed by the Global Ocean Turbulence Model (GOTM), which is coupled to MOHID and consists of a set of turbulence-closure models (Buchard et al., 1999; Villarreal et al., 2005).

To solve the Navier-Stokes and continuity equation, appropriate boundary conditions are required for the lateral (e.g., land and open sea), surface and bottom boundaries. MOHID has available a great variety of open boundary conditions of several types: Dirichlet, Neumann, radiation, cyclic, relaxation (or nudging), etc. Some boundary conditions can be combinations of the types enumerated, e.g., a combination of radiation with nudging (Blumberg and Kantha, 1985). Open boundary conditions (OBC) can be imposed by prescribing the values of a specific variable (Dirichlet boundary condition). This condition is commonly applied in coastal models to impose tidal levels when the correspondent barotropic velocities are not available. On the other hand, following a Neumann boundary condition, the gradient of a specific variable is imposed instead of a prescribed value. Assuming a null gradient condition, the value of a variable at a boundary point is equal to the value at an adjacent interior point. When the shoreline location and bathymetry are uniforms, e.g, in schematic cases, cyclic boundary conditions can be applied.

A relaxation scheme can be applied as an OBC by assuming a decay time that increases gradually from the boundary to infinite after a defined number of cells (see Martinsen and Engedahl, 1987; Engedahl, 1995):

$$P^{t+\Delta t} = P^* + (P^{ext} - P^*) \frac{\Delta t}{T_d} \quad (5.2)$$

where  $P$  is a generic property,  $P^*$  is the property value calculated by the model,  $P^{ext}$  is the reference value of the property,  $\Delta t$  is the model time step and  $T_d$  is the relaxation time scale.

Radiation methods can also be used to impose the OBC, which allow the propagation of internal disturbances on water levels through the open boundaries. These disturbances can be caused, for example, by the wave forces. MOHID has two types of radiation conditions (Leitão, 2003), based on Blumberg and Kantha (1985), Eq. 5.3, and Flather (1976), Eq. 5.4:

$$\frac{\partial \eta}{\partial t} + (\vec{C}_E \cdot \vec{n}) \Delta \eta = \frac{1}{T_d} (\eta_{ext} - \eta) \quad (5.3)$$

$$q - q_{ext} = (\eta_{ext} - \eta) (\vec{C}_E \cdot \vec{n}) \quad (5.4)$$

where  $\eta$  and  $q$  are the water level and specific flow, respectively;  $\eta_{ext}$  and  $q_{ext}$  are the imposed values of  $\eta$  and  $q$  at open boundary points;  $\vec{C}_E$  is the celerity of internal water level disturbances or the celerity of external waves ( $C_E = \sqrt{gh}$ ). When  $T_d$  is approximated to infinity in the Eq. 5.3, the boundary condition becomes totally passive, which means that the water levels at the boundary points are computed only from the internal water levels. An approximated null relaxation time scale means that the water level is imposed as  $\eta_{ext}$ . The Flather radiation condition is mostly used in nested model domains, when velocities and water levels are known at the open boundaries. Many of the boundary conditions used by MOHID use the concept of external (or reference) solution. These solutions can be provided via input file or via a one-way nesting of a chain of models. This last process is used to downscale from large-scale domains to local ones (e.g., Franz et al., 2016). In the case of land points, the closed boundary condition is imposed as null fluxes of mass and momentum in the perpendicular direction. The covering and uncovering of boundary cells can be represented in MOHID by a wetting/drying scheme (Martins et al, 2001).

At the surface, fluxes of momentum from wind action and wave breaking can be considered (Delpy et al., 2014). At the bottom, the method proposed by Soulsby and Clarke (2005) to compute the bed shear stress was implemented in this work, consisting of a steady component due to currents together with an oscillatory component due to waves. In a laminar flow, the combined bed shear stress is a simple linear addition of the laminar current-alone and wave-alone shear stresses. However, in turbulent flows this addition is non-linear and the mean and oscillatory components of the stress are enhanced beyond the values of the laminar case. The mean bed shear stress is used for determining the friction governing the current, whereas the maximum shear stress is used to determine the threshold of sediment motion. The turbulence generated by the skin friction acts directly on bottom sediment grains (Einstein, 1950), contrarily to that related to bed forms. Thus, the threshold of sediment motion depends on the grain-related bed shear stress.

### 5.3.2 Bed load transport

The bed load transport under the combined effect of currents and waves is computed following the semi-empirical formulation of Soulsby and Damgaard (2005). The formulation was derived for current plus sinusoidal and asymmetrical waves, as well as asymmetrical waves alone. Amoudry and Liu (2010) obtained a generally good agreement comparing the results of Soulsby and Damgaard (2005) formulations with a sheet flow model, concluding that it can be implemented in both intrawave and wave-averaged models in order to study sediment transport. The parallel  $\Phi_{\parallel}$  and normal  $\Phi_{\perp}$  components of the non-dimensional bed load transport vector in relation to the current direction are:

$$\Phi_{\parallel} = \max(\Phi_{\parallel 1}, \Phi_{\parallel 2}); \text{ if } \theta_{max} > \theta_{cr} \quad (5.5a)$$

$$\Phi_{\parallel 1} = k_{\Phi 1} \theta_m^{k_{\Phi 2}} (\theta_m - \theta_{cr})^{k_{\Phi 3}} \quad (5.5b)$$

$$\Phi_{\parallel 2} = k_{\Phi 1} (0.9534 + 0.1904 \cos 2\phi) \theta_w^{1/2} \theta_m + k_{\Phi 1} (0.229 \nabla \theta_w^{3/2} \cos \phi) \quad (5.5c)$$

$$\Phi_{\perp} = k_{\Phi 1} \frac{(0.1907 \theta_w^2)}{\theta_w^{3/2} + (3/2) \theta_m^{3/2}} (\theta_m \sin 2\phi + 1.2 \nabla \theta_w \sin \phi); \text{ if } \theta_{max} > \theta_{cr} \quad (5.6)$$

where  $\theta_m$  and  $\theta_w$  are the time-mean and oscillatory part of the bed shear stress (non-dimensional), respectively;  $k_{\Phi 1}$ ,  $k_{\Phi 2}$  and  $k_{\Phi 3}$  are calibration coefficients that allow to represent different equations for the bed load transport found in the literature (e.g., Amoudry and Souza, 2011);  $\phi$  is the angle between the wave propagation and current direction;  $\nabla$  is a factor that represents the wave's asymmetry;  $\theta_{cr}$  is the critical non-dimensional bed shear stress, which depends on sediment diameter and bed-material gradation. The bed load transport is null ( $\Phi_{\parallel} = \Phi_{\perp} = 0$ ) if  $\theta_{cr}$  is greater than or equal to the maximum non-dimensional bed shear stress ( $\theta_{max}$ ):

$$\theta_{max} = \max(\theta_{max1}, \theta_{max2}) \quad (5.7a)$$

$$\theta_{max1} = \left( (\theta_m + \theta_w (1 + \nabla) \cos \phi)^2 + (\theta_w (1 + \nabla) \sin \phi)^2 \right)^{1/2} \quad (5.7b)$$

$$\theta_{max2} = \left( (\theta_m + \theta_w (1 - \nabla) \cos(\phi + \pi))^2 + (\theta_w (1 - \nabla) \sin(\phi + \pi))^2 \right)^{1/2} \quad (5.7c)$$

The bed load transport vector,  $\vec{\Phi} = (\Phi_{\parallel}, \Phi_{\perp})$ , is enhanced in the presence of waves. Regarding the symmetrical case ( $\nabla = 0$ ), the effect of the wave's asymmetry results in an additional increase in the normal component ( $\Phi_{\perp}$ ), whereas the parallel component ( $\Phi_{\parallel}$ ) can be increased or reduced, depending on the angle ( $\phi$ ) between the wave propagation and current direction. As the water depth decreases, the wave's asymmetry becomes more significant. The asymmetry factor ( $\nabla = \theta_{w,2}/\theta_{w,1}$ ) is defined as the ratio between the bed shear stress due to the waves second harmonic ( $\theta_{w,2}$ ) and basic harmonic ( $\theta_{w,1}$ ), set to a maximum value of 0.2 (Soulsby and Damgaard, 2005). Considering the quadratic friction law ( $\vec{\tau}_b = \rho C_D \vec{v}_H |\vec{v}_H|$ ) to determine the magnitude of the wave's bed shear stress, the asymmetry factor is computed as:

$$\nabla = \left( \frac{U_{w,2}}{U_{w,1}} \right)^2 = \left( \frac{3}{4} \frac{\pi H_w}{L_w \sinh^3(k_w h)} \right)^2 \quad (5.8)$$

where  $U_{w,2}$  and  $U_{w,1}$  are the amplitude of near-bed wave-orbital velocity for the second harmonic and basic harmonic of Stokes second order wave theory (e.g., Greenwood and Davis, 2011), respectively;  $H_w$  is the wave height;  $L_w$  is the wavelength;  $k_w = 2\pi/L_w$  is the wave number; and  $h$  is the water depth.

To compute the sediment fluxes between grid cells, the components of the non-dimensional bed load transport vector are rotated to the grid referential (u-axis and v-axis):

$$\Phi_u = \Phi_{\parallel} \cos \varnothing_c - \Phi_{\perp} \sin \varnothing_c \quad (5.9a)$$

$$\Phi_v = \Phi_{\parallel} \sin \varnothing_c + \Phi_{\perp} \cos \varnothing_c \quad (5.9b)$$

where  $\varnothing_c$  is the angle between the horizontal velocity vector and the u-axis. Thus, the bed load transport vector,  $\vec{q} = (q_u, q_v)$ , in mass units ( $\text{kg m}^{-1}\text{s}^{-1}$ ) is equal to:

$$q_u = \rho_s \Phi_u [g(\rho_r - 1)d^3]^{1/2} \quad (5.10a)$$

$$q_v = \rho_s \Phi_v [g(\rho_r - 1)d^3]^{1/2} \quad (5.10b)$$

where  $\rho_s$  is the sand particle density ( $\text{kg m}^{-3}$ );  $\rho_r$  is the relative density ( $\rho_s/\rho$ ); and  $d$  is the sand representative diameter (m).

### 5.3.3 Bed slope correction

Wave action induces a shoreward sediment transport that has no counterpart in 2DH models, leading to sand accumulation in the nearshore and increasing the steepness of the beach profile. Actually, undertow currents are responsible for a seaward sediment transport, which may generate sandbars. Diverse opposing forces are responsible for creating an equilibrium profile, which depends on sediment characteristics and wave heights (Dean, 1991). To account for the neglected forces in 2DH models, we defined a maximum slope ( $\alpha_{max}$ ) that when exceeded induces sediment transport in the down slope direction. This artificial sediment transport may act as the undertow, transporting sediment seaward. The mass of sand ( $M$ ) in the sediment column and, consequently, the bathymetry are updated when the bottom slope ( $\alpha$ ) is larger than  $\alpha_{max}$ :

$$M_{i,j}^{t+1} = M_{i,j}^t - \Delta M \quad (5.11a)$$

$$M_{i,j+1}^{t+1} = M_{i,j+1}^t + \Delta M \quad (5.11b)$$

where:

$$\Delta M = \Delta z_b A \rho_s (1 - n), \alpha > \alpha_{max} \quad (5.12a)$$

$$\Delta M = 0, \alpha \leq \alpha_{max} \quad (5.12b)$$

in which  $n$  is the sediment porosity,  $A$  is the grid cell area,  $t$  is an index symbol for time, and  $i, j$  are index symbols to identify the grid cell ( $i$  - line number,  $j$  - column number). Considering the  $u$ -direction, the bed change in one time step ( $\Delta z_b$ ) is computed as:

$$\Delta z_b = \min\left((|\alpha| - \alpha_{max})\Delta x, \Delta z_{b_{max}}\right), \alpha > 0 \quad (5.13a)$$

$$\Delta z_b = \min\left(-(|\alpha| - \alpha_{max})\Delta x, -\Delta z_{b_{max}}\right), \alpha < 0 \quad (5.13b)$$

where  $\alpha = (z_{b_{i,j+1}} - z_{b_{i,j}}) / \Delta x$ ,  $\Delta x$  is the cell width,  $z_b$  is the distance from the bed to a reference height (e.g., the hydrographic zero), and  $\Delta z_{b_{max}}$  is a threshold to avoid numerical instabilities due to large shockwaves. Similar equations are used in the  $v$ -direction. Different values of the maximum slope ( $\alpha_{max}$ ) can be defined in wet and dry cells. This method is based on that of Roelvink et al. (2009), previously applied to simulate dune erosion. The shoreline position is also updated following this approach.

### 5.3.4 Model Coupling

The coupling between the MOHID modelling system and the SWAN wave model was performed through tools developed in the Fortran language as part of the MOHID code in order to convert the results to the appropriate format. An external tool was also developed in Python language to automatically manage the runs of the tools and models. Fields of significant wave height, wave period, wavelength, wave direction, wave-induced force (radiation stress), and maximal orbital velocity near the bottom can be provided by SWAN to MOHID. In return, fields of water level, current velocity and bathymetry can be provided by MOHID to SWAN. The frequency of fields updating can be defined by the user for each application, depending on the variability of forcing conditions and speed of morphological changes.

## 5.4 Test Cases

### 5.4.1 Coastal Defence Structures

The morphological evolution of a schematic beach was simulated considering different designs of detached breakwaters and groynes to assess model results. Constant wave conditions were defined

along the offshore boundary (1.5 m of wave height, 8 s of peak wave period and 15° of peak wave direction), following the JONSWAP spectrum. The hydrodynamic model was applied in 2DH mode, considering the vertically integrated wave-induced forces. The sand granulometry was uniform with a diameter of 0.2 mm.

The MOHID domain was defined as 2 km cross-shore by 3 km alongshore, whereas the SWAN domain was defined as 2 km cross-shore by 9 km alongshore (3 km larger in each side of the MOHID domain). The grid resolution was equal in both models, ranging from 50 m x 50 m to 10 m x 10 m. A larger domain for the wave model was considered to avoid inaccuracies in the lateral boundaries (shadow zones), as incident wave energy was imposed only along the offshore boundary. To prevent discontinuities in the SWAN bathymetry, the part of the domain not covered by the MOHID domain was updated with the depths of the MOHID cross-shore boundaries.

The open boundary condition was defined as a null gradient for the sediment concentrations in the water column, as well as for the sediment mass evolution at the bottom column (or, equivalently, for bathymetry). A null gradient condition was also imposed at the open boundaries for the normal and tangential current velocities. The radiation condition of Blumberg and Kantha (1985) was imposed for water level (Eq. 5.3), assuming a passive condition at the cross-shore boundaries ( $T_d = 1e^{32}s$ ) and an active condition at the offshore boundary ( $T_d = 1e^{-12}s$ ). Thus, the water level was imposed at the offshore boundary as equal to the initial condition (zero in this case) to maintain the average water level inside the model domain, otherwise it would continuously decrease. The effect of lateral friction in land boundaries was considered for a better representation of the flow around the groynes. The horizontal viscosity was set as  $1.0 \text{ m}^2\text{s}^{-1}$ .

The initial bathymetry was defined by considering an equilibrium profile of the form:  $h = \beta y^{2/3}$  (Dean, 1991), where  $\beta$  is a constant set to 0.12, and  $y$  is the distance to the shoreline. The average slope is approximately 1:60 in the first 200 m from the shoreline, decreasing seaward. The maximum slope ( $\alpha_{max}$ ) was defined as 1:50 for the bed slope corrections. The bathymetry evolution was allowed only after a warm-up period, considering a morphological acceleration factor of 365. This means that 1 day of simulation time is equivalent to 1 year of morphological changes. The wave forcing was updated in MOHID, as the bathymetry and water levels were updated in SWAN, with a constant frequency of 5 min (or 30 h of morphological evolution).

#### 5.4.2 Detached Breakwaters

Detached breakwaters generate sediment transport from the adjacent coast to the lee side of the structure, leading to the formation of a bulge or salient in the beach planform. Depending on

geometrical features of the breakwater, wave climate and sediment availability, the salient may become attached to the breakwater forming a tombolo. Based on the analysis of several existing breakwater projects, Dally and Pope (1986) found that a ratio ( $r$ ) between breakwater's length and distance to the shoreline less than 0.5 prevents the development of a tombolo. In contrast, the development of a tombolo is assured if  $r$  is larger than 1.5, assuming sufficient sediment supply. Taking these values into account, we tested the model response for the four different detached breakwater designs described in Table 5.1.

Table 5.1– Detached breakwaters considered for test case scenarios

<b>Length</b>	<b>Distance</b>	<b>Ratio (<math>r</math>)</b>	<b>Beach response*</b>
100	500	0.2	Salient
100	200	0.5	Salient
200	200	1.0	Salient/tombolo
200	100	2.0	Tombolo

\* Beach response according to Dally and Pope (1986)

Models results for a near equilibrium planform of the shoreline agree with the analysis of Dally and Pope (1986), demonstrating the development of a salient for  $r$  equal to 0.2, 0.5 and 1.0 (Figure 5.1, Figure 5.2, Figure 5.3), which become attached to the breakwater forming a tombolo only for  $r$  equal to 2.0 (Figure 5.4). The obliquity of waves generates a longshore current and, consequently, longshore sediment transport in the nearshore zone. The shoreline tends to be parallel to the wave crests, creating asymmetric bulges. For  $r$  equal to 0.5 and 1.0, longshore currents restricted the size of the salients, preventing the connection with the breakwater. The shoreline advances more on the updrift side for larger values of  $r$ , trapping sediment from the littoral drift. On the other hand, the downdrift beach erosion increases. When a tombolo is formed, the detached breakwater affects the shoreline similarly to a groyne.

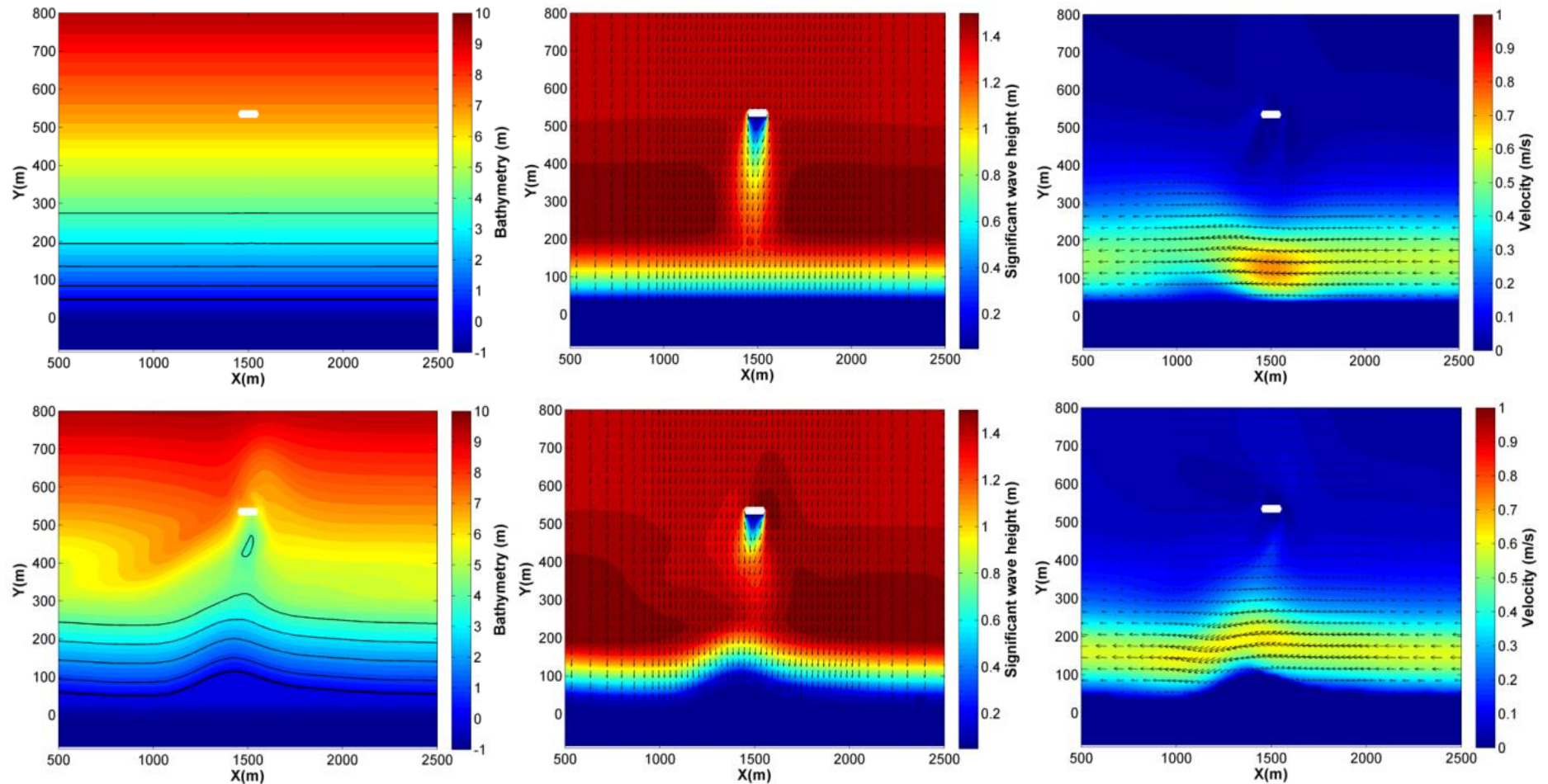


Figure 5.1– Model results for the breakwater's length to distance ratio of 0.2. Bathymetry (left), waves (middle) and currents (right) for the initial condition (above) and near equilibrium (below) after 9 years. The thicker isoline in the bathymetry represents the shoreline, whereas the remaining represent the 1 m, 2 m, 3 m and 4 m isobaths.

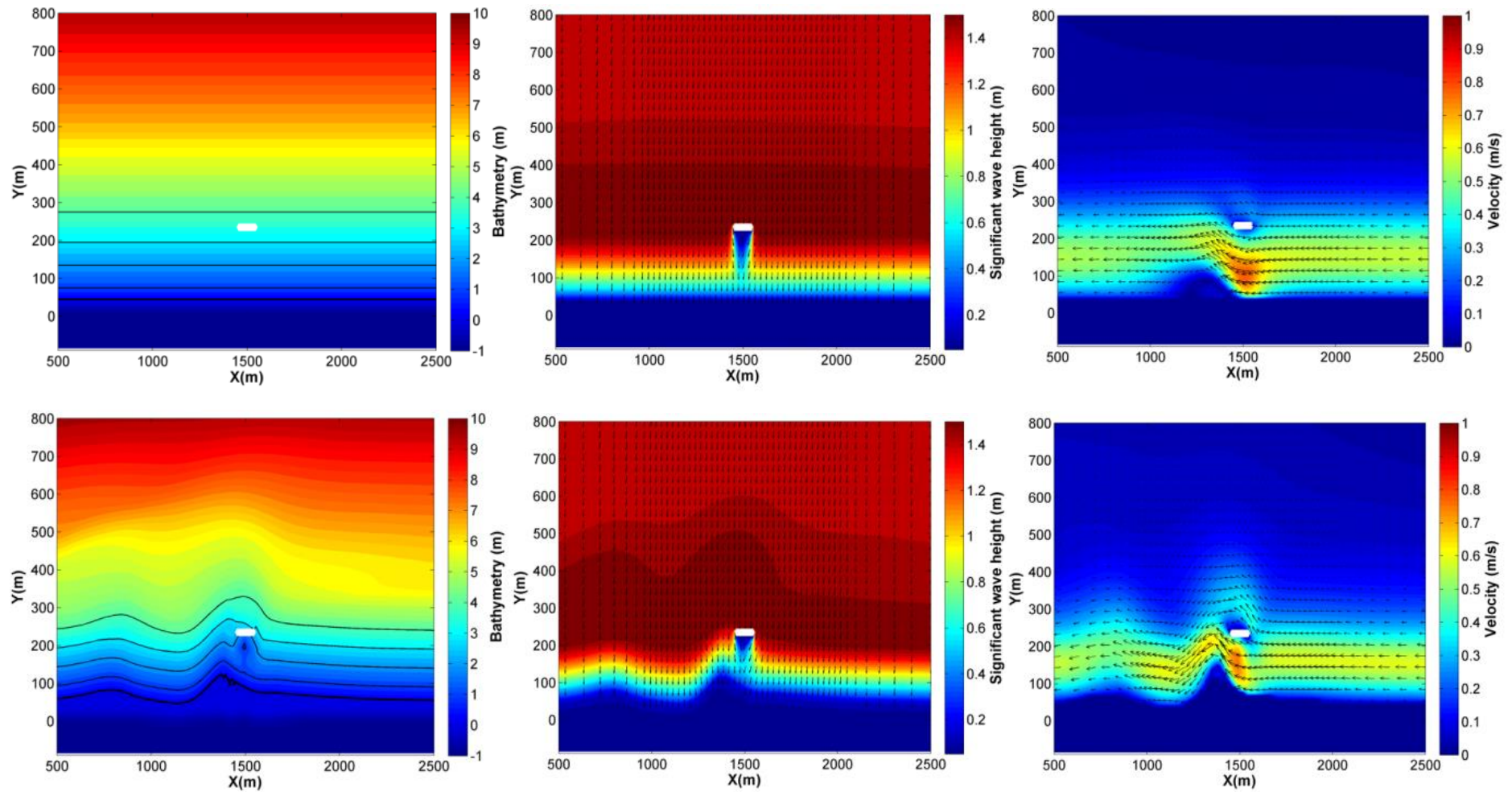


Figure 5.2 – Model results for the breakwater's length to distance ratio of 0.5. Bathymetry (left), waves (middle) and currents (right) for the initial condition (above) and near equilibrium (below) after 18 years. The thicker isoline in the bathymetry represents the shoreline, whereas the others represent the 1 m, 2 m, 3 m and 4 m isobaths.

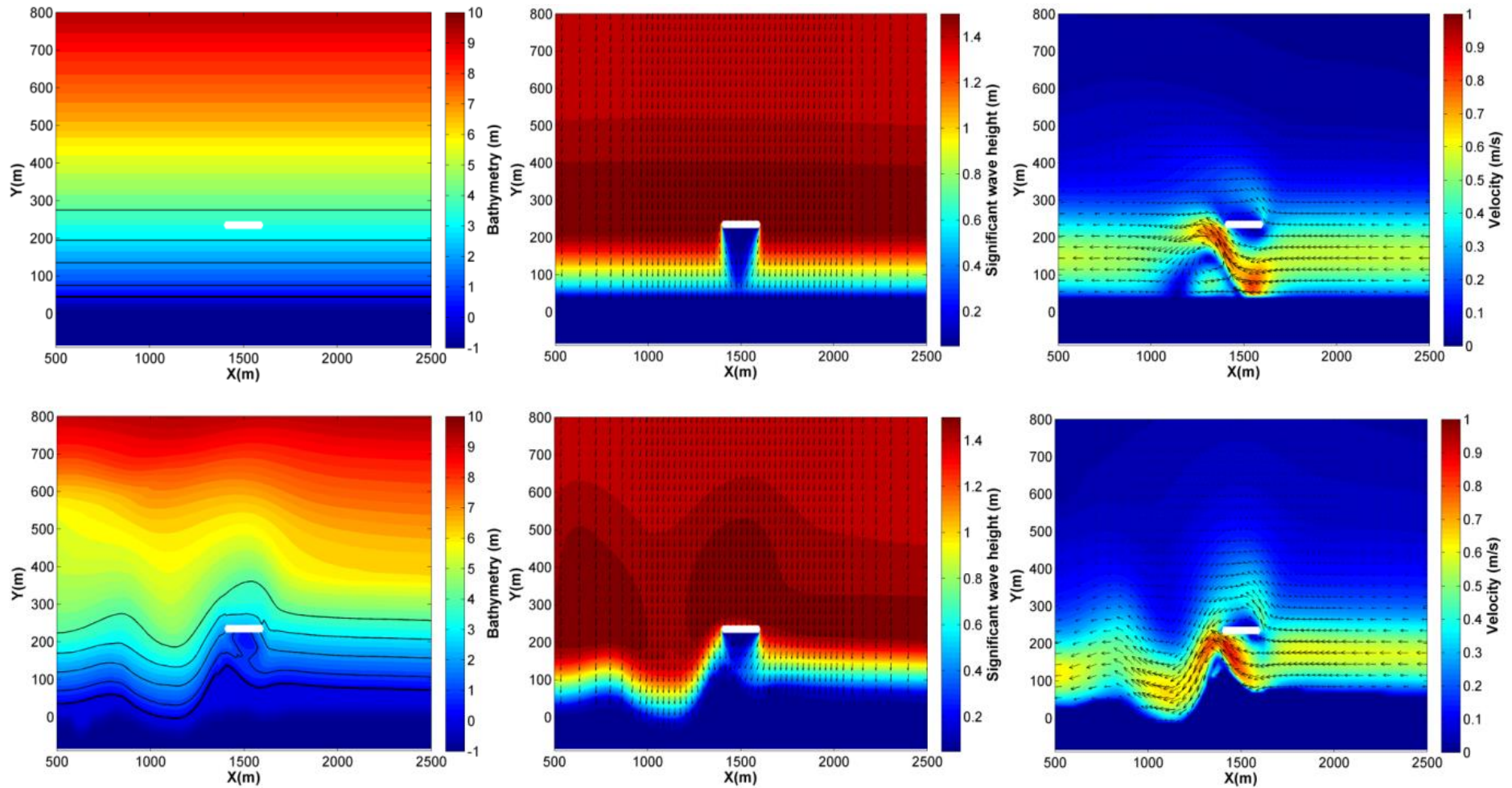


Figure 5.3 – Model results for the breakwater's length to distance ratio of 1.0. Bathymetry (left), waves (middle) and currents (right) for the initial condition (above) and near equilibrium (below) after 27 years. The thicker isoline in the bathymetry represents the shoreline, whereas the others represent the 1 m, 2 m, 3 m and 4 m isobaths.

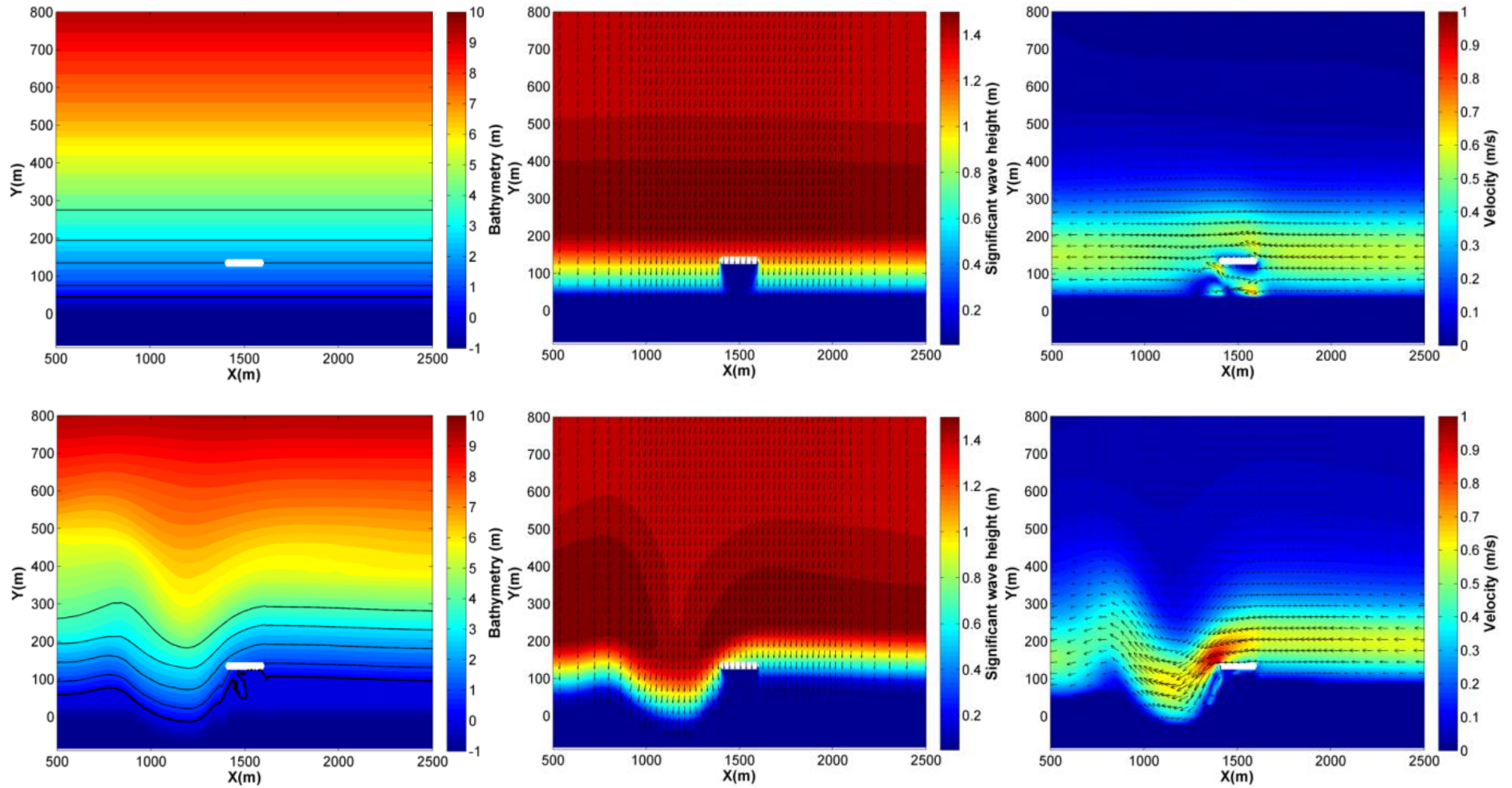


Figure 5.4 - Model results for the breakwater's length to distance ratio of 2.0. Bathymetry (left), waves (middle) and currents (right) for the initial condition (above) and near equilibrium (below) after 18 years. The thicker isoline in the bathymetry represents the shoreline, whereas the others represent the 1 m, 2 m, 3 m and 4 m isobaths.

### 5.4.3 Groynes

Groynes are applied to reduce the littoral drift in the surf zone, trapping sediment on the updrift side of the structure, which may cause erosion problems on the downdrift side. Moreover, the longshore currents are forced to deviate into deeper water around groynes, causing sediment losses from nearshore to offshore. The morphological impacts of the groynes are a function of their length from the shoreline. Model results were assessed for two designs of groynes, with lengths of 100 m and 200 m (Figure 5.5 and Figure 5.6). As expected, greater erosion occurs on the downdrift side for a longer groyne, as more sediment from the littoral drift gets trapped on the updrift side. Furthermore, offshore sediment transport becomes intensified in the 200 m length groyne design, as the deviation of longshore currents is more important. In this case, the retrogradation of the shoreline is similar to the case of a detached breakwater in which a tombolo was formed.

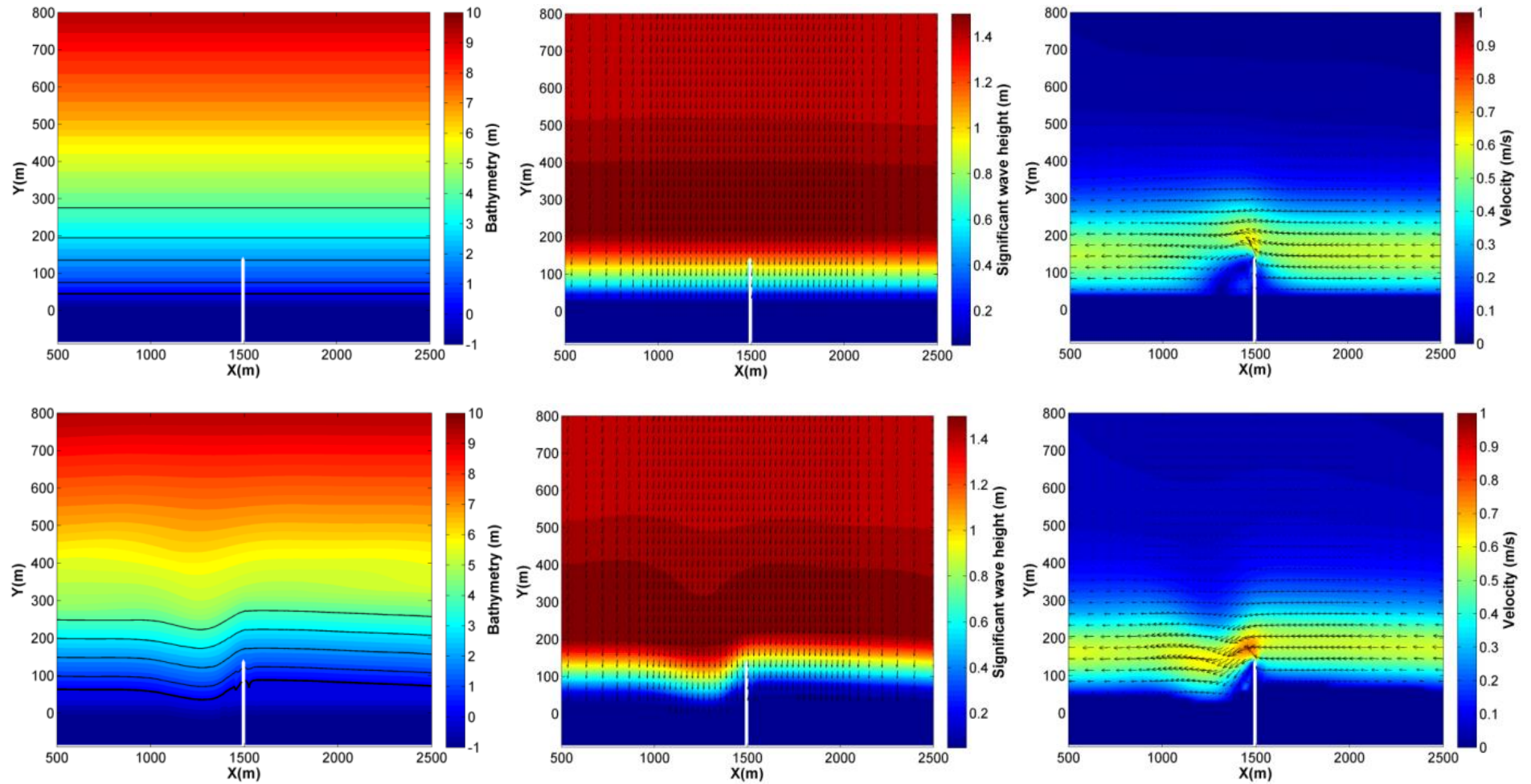


Figure 5.5 - Groyne with a length of 100 m from the shoreline. Bathymetry (left), waves (middle) and currents (right) for the initial condition (above) and near equilibrium (below) after 9 years. The thicker isoline in the bathymetry represents the shoreline, whereas the others represent the 1 m, 2 m, 3 m and 4 m isobaths.

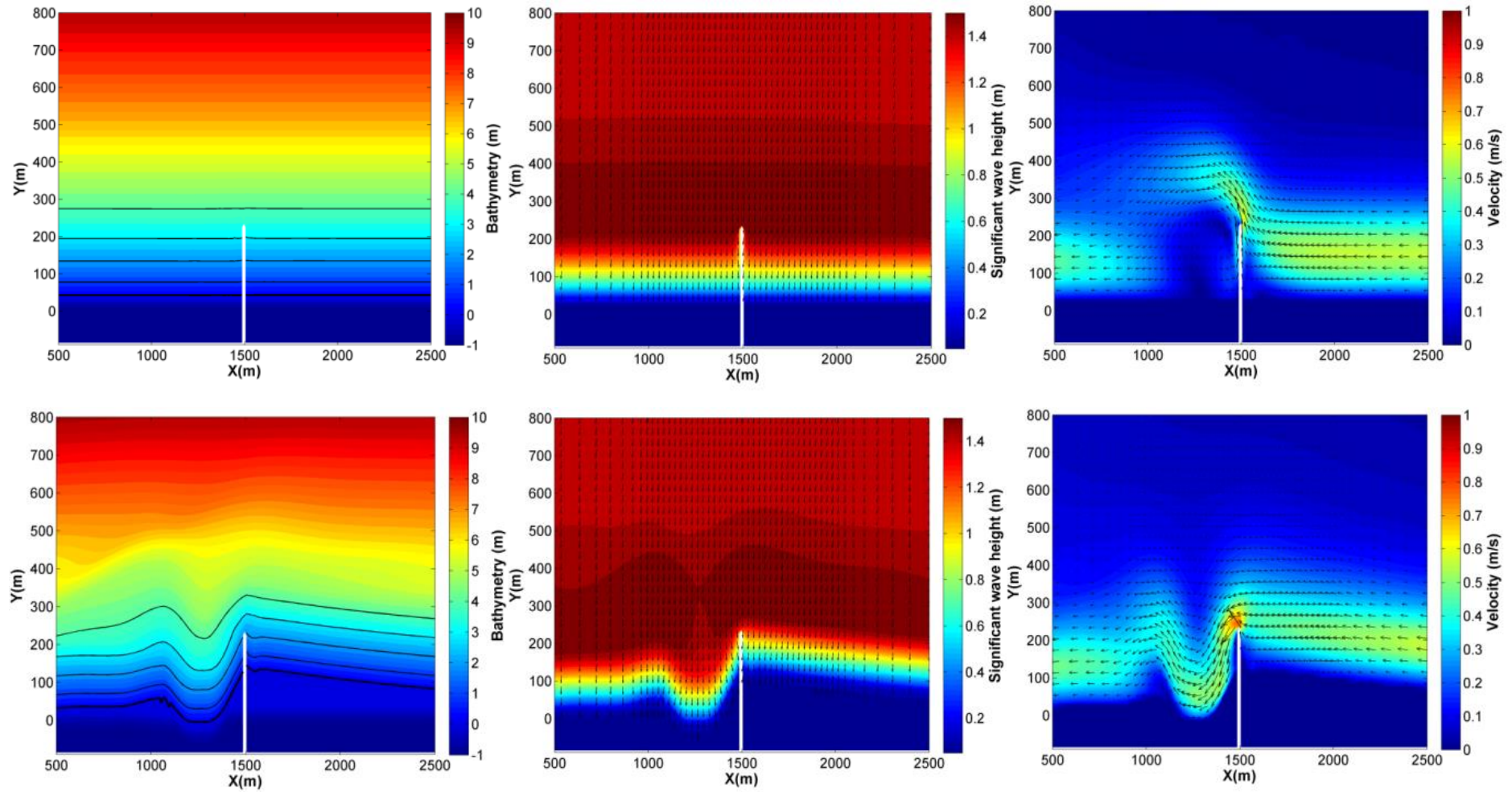


Figure 5.6 – Groyne with a length of 200 m from the shoreline. Bathymetry (left), waves (middle) and currents (right) for the initial condition (above) and near equilibrium (below) after 9 years. The thicker isoline in the bathymetry represents the shoreline, whereas the others represent the 1 m, 2 m, 3 m and 4 m isobaths.

#### 5.4.4 Sandbars Formation

In this test case, we verified the model capacity to generate sandbars in a 3D approach. The same domain and sand granulometry (0.2 mm) as in the previous 2DH test cases were considered but ignoring defence structures. Two wave heights (1.5 m and 1.0 m) were defined in sequence along the offshore boundary during periods of 45 days of morphological evolution (3 h of simulation time with a morphological acceleration factor of 365). The peak wave period and peak wave direction were maintained constant (8 s and 15°). For the 3D case, a larger maximum slope was defined as 1:10 for the bed slope corrections, considering that the seaward sediment transport due to undertow currents can now be represented. The maximum slope in 3D simulations is useful to represent the sand motion induced by excessively steep slopes.

The water column was divided into five sigma layers and a simple exponential approach was followed to consider the vertical variation of the wave-induced forces: an exponential decrease of the radiation stress is imposed from the surface to the bottom, following the same shape as the profile of the orbital velocities, provided by the linear wave theory. The vertical radiation stress profile is designed to conserve the vertically integrated flux of momentum, which remains equal to the flux given by SWAN. The idea here is only to provide an approximate representation of the vertical distribution of wave momentum, in order to generate a general undertow pattern. Thus, the corresponding results should be considered as a first qualitative evaluation of the effect of such an undertow in our morphological module, the latter being our focus here. It is left for further work to use a more advanced formulation of 3D wave-current interactions for more quantitative investigations. The k- $\epsilon$  turbulence-closure model was used to compute the vertical viscosity, with the MOHID default parameterization, whereas the horizontal viscosity was set as  $1.0 \text{ m}^2 \text{ s}^{-1}$ .

The open boundary condition for sediment concentrations in the water column and sediment mass evolution at the bottom column was defined as a null gradient, as well as the boundary conditions for normal and tangential velocities, as in the previous 2DH test cases. Considering that defence structures were ignored in this test case, the bathymetry evolution was expected to be nearly uniform along the beach. Thus, a cyclic boundary condition was imposed at the cross-shore boundaries together with a Flather radiation condition at the offshore boundary (Eq. 5.4).

The model was capable of representing an undertow pattern and associated sediment transport that induces the formation of longshore sandbars (Figure 5.7). A longitudinal current is presented in the surf zone, similarly to that observed in 2DH. However, a cross-shore velocity component is now represented by the 3D model. Inside the surf zone, this component is shoreward near the surface and seaward near the bottom. As expected, the cross-shore component has opposite directions

before and after the breaking zone. The sandbar migrated seaward, changing the location of the breaking zone until wave heights decreased to 1.0 m after 45 days. At this time, waves were able to propagate further without breaking, creating a new sandbar nearer to the coast. Finally, the results demonstrate the model's potential to represent the formation of multiple sandbars, which are observed in many places (e.g., Dolan and Dean, 1985; Ruessink et al., 2009).

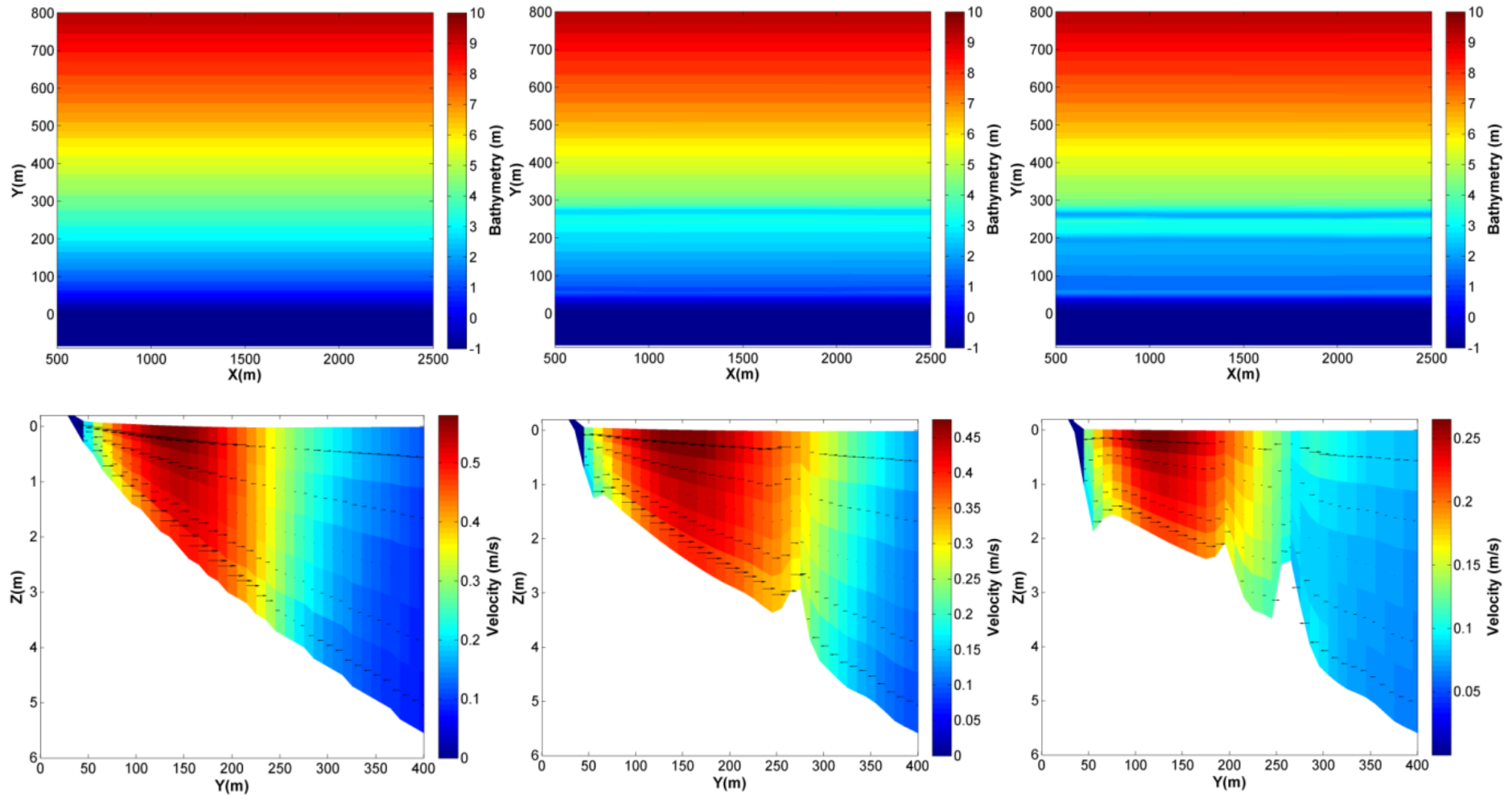


Figure 5.7 – Simulated sandbars for different wave heights. The horizontal plane of the bathymetry (above) and a vertical cut with velocity modulus and vectors (below). Left: Initial condition. Middle: After 45 days of morphological evolution with 1.5 m wave height. Right: After additional 45 days of morphological evolution with 1.0 m wave height.

### 5.4.5 Costa da Caparica

The hydrodynamics and sediment transport in the southern coast of the Tagus Estuary mouth (Costa da Caparica) were evaluated under extreme wave conditions by coupling the MOHID modelling system and the SWAN wave model. A significant coastline retreat was observed in the Costa da Caparica in the last century. Defence structures (groynes) were built around the 1960's to reduce coastal erosion, resulting in some stability until the 2000/2001 winter when this issue started to receive more attention from the local authorities (Veloso-Gomes et al., 2009). The importance of the problem has augmented due to urbanisation and tourism development. The location near to the Tagus Estuary inlet increases the complexity of sediment dynamics in this zone.

A downscaling approach was followed to provide appropriate boundary conditions for the Costa da Caparica model, considering previous results of the wave and hydrodynamic modelling system for the Portuguese Coast developed by the MARETEC research group (<http://forecast.maretec.org>). A new domain was created between the capes Raso and Espichel with 100 m x 100 m of grid resolution to propagate the waves until the Tagus Estuary mouth. The bathymetries of the father hydrodynamic model and wave model are presented in Figure 5.8, showing the domain of the Costa da Caparica model. The hydrodynamic boundary conditions (water level, current velocities, salinity, and temperature) for the Costa da Caparica model were provided by the three-dimensional baroclinic model for the Tagus Estuary (see Franz et al., 2014b, 2014c), through the application of the relaxation scheme together with the Flather radiation condition. The wave model for the Portuguese Coast was validated previously considering the data of the Port of Lisbon wave buoy, among others buoys located along the Portuguese Coast (see Franz et al., 2014d).

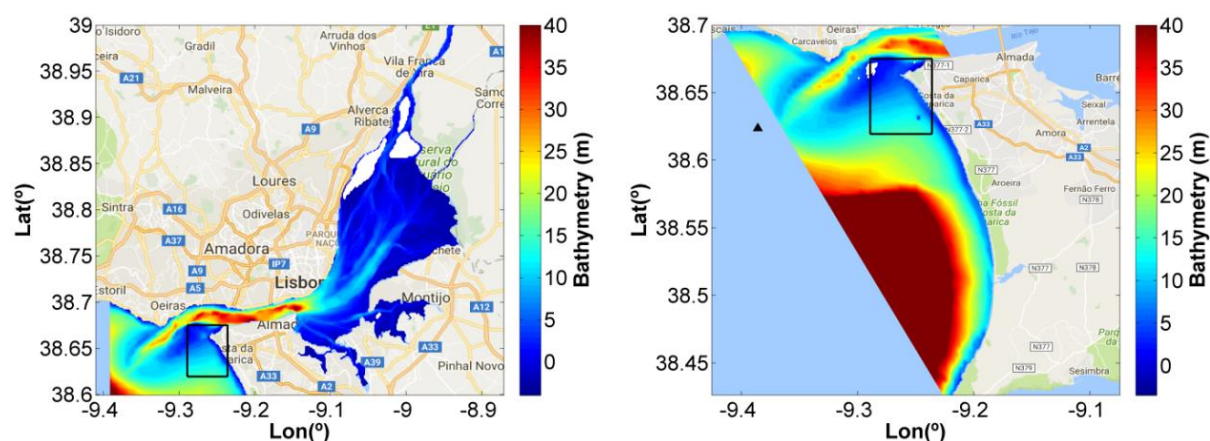


Figure 5.8 – Bathymetries of the Tagus Estuary hydrodynamic model (left) and the wave model (right) created to propagate the waves until the Tagus Estuary mouth. The domain of the Costa da Caparica model is presented by the black rectangle and the location of the Port of Lisbon wave buoy is indicated by the black triangle.

The Tagus estuary is classified as mesotidal, with an average tidal height of 2.0 m in the mouth (Lemos, 1972). The tide is the main mechanism forcing the flow in the estuary, determining current directions and water level variations (Franz et al., 2014a). The maximum velocities reach up to  $2 \text{ m s}^{-1}$  in the estuary mouth. The Tagus River is the estuary's main freshwater source, with an annual average flow of about  $300 \text{ m}^3 \text{ s}^{-1}$ . The estuary stratification is strongly related to the river flow and tidal cycle. The residual currents pattern in the Tagus Estuary mouth is characterised by a jet in the inlet channel and two adjacent vortices, originating a residual recirculation into the inlet estuary direction in front of the Costa da Caparica (Figure 5.9).

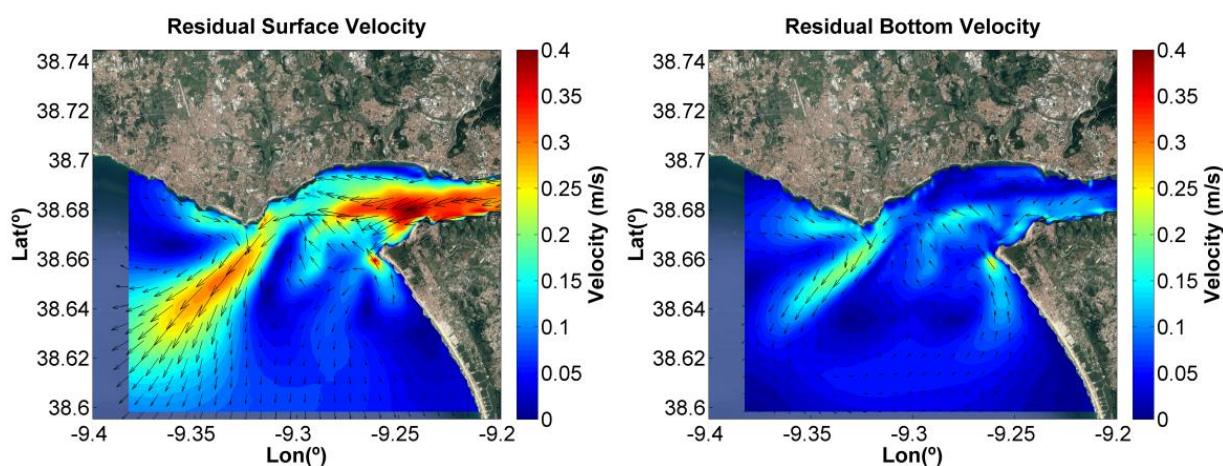


Figure 5.9 – Residual velocity in the Tagus Estuary mouth at the surface (left) and near the bottom (right) obtained from the three-dimensional baroclinic model for the Tagus Estuary.

The effects of the waves on the currents and sediment transport were investigated during a high energy event in the winter of 2013/2014 caused by Hercules storm. The wave conditions for the period of study in the location of the Port of Lisbon wave buoy reached wave heights higher than 7 m and wave periods up to 20 s (Figure 5.10). A variable grid resolution was defined for the Costa da Caparica domain, ranging from 50 m to 10 m near the coast. The water column was divided into ten layers, including five layers in the first metre above the bottom with fixed thickness ranging from 0.1 m to 0.3 m, and five sigma layers on top. The vertical viscosity was computed through the  $k-\epsilon$  turbulence-closure model and the horizontal viscosity was set as  $5.0 \text{ m}^2 \text{ s}^{-1}$ . The bathymetry data for the coast of the Costa da Caparica were provided by the Portuguese Environment Agency (APA).

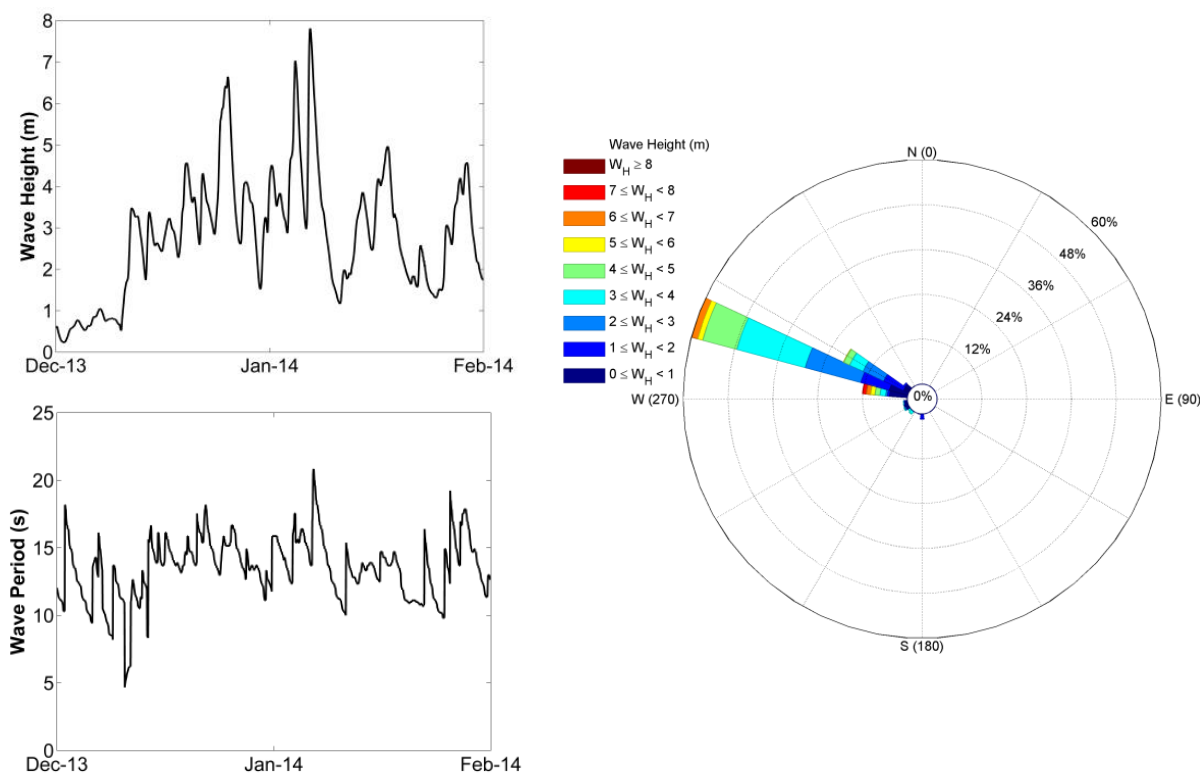


Figure 5.10 - Wave conditions for the winter of 2013/2014 obtained from the Portuguese Coast wave model in the location of the Port of Lisbon wave buoy.

In a first scenario, the effects of the waves on the currents and sediment transport were neglected. Therefore, just the influence of hydrodynamic boundary conditions from the Tagus Estuary model was taken into account. The results of the Costa da Caparica model without the wave action demonstrate strong velocities up to  $2 \text{ m s}^{-1}$  at the surface and  $0.5 \text{ m s}^{-1}$  near the bed in the northern zone (Cova do Vapor) with opposite directions on the flood and ebb tides, whereas weak velocities are found in the remaining coast directed to the inlet estuary in both situations (Figure 5.11). The strong tidal currents are deflected away from the shoreline by the long groyne with approximately 500 m length located at Cova do Vapor.

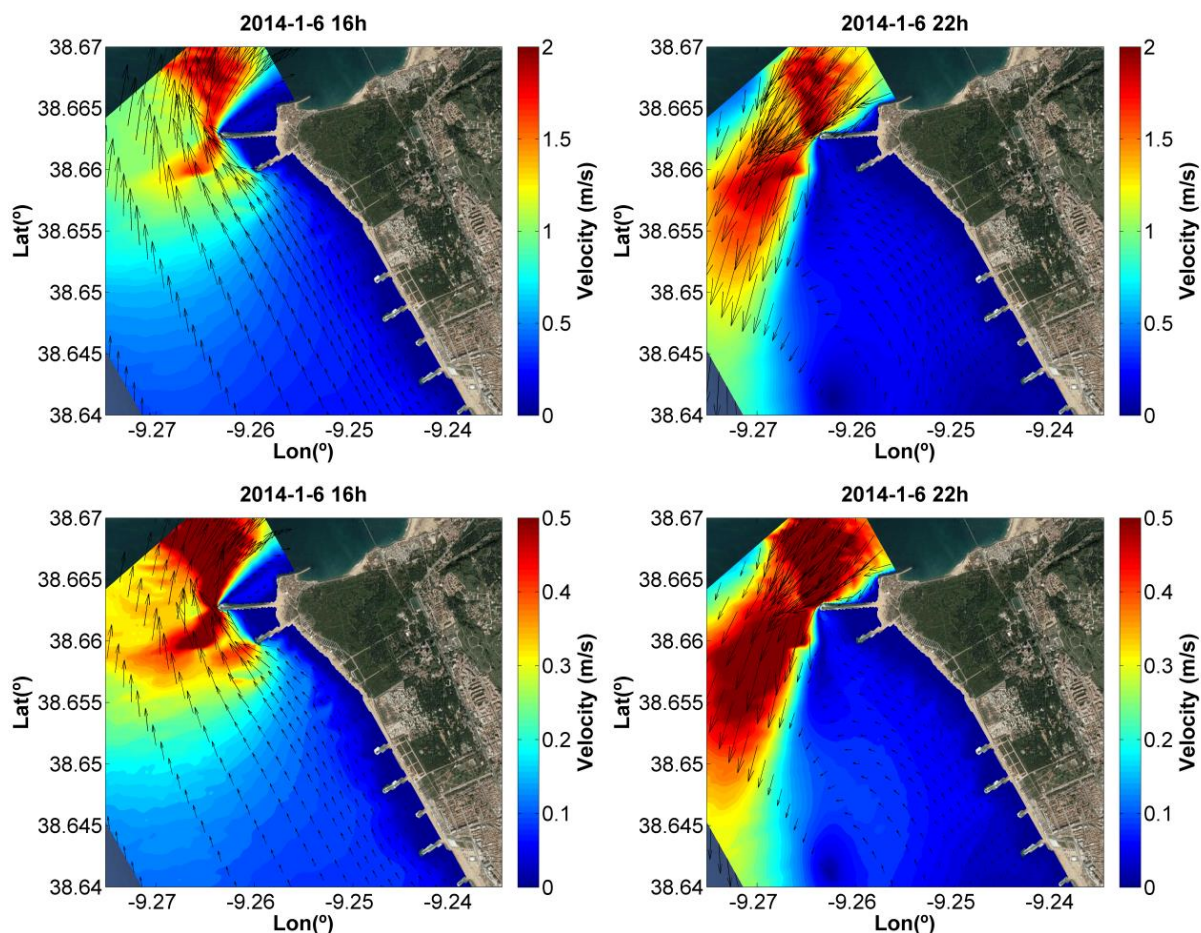


Figure 5.11 – Velocity results of the Costa da Caparica model during flood (left) and ebb (right) tides at the surface (above) and near the bottom (below) without considering the wave’s effect on the hydrodynamics.

During the period of study, the waves propagated from offshore mainly with a west-northwest (WNW) direction (Figure 5.10). The bathymetric features (Figure 5.8) cause the modification of the wave propagation direction due to refraction to a west-southwest (WSW) or southwest (SW) direction in the nearshore (Figure 5.12). The effect of the currents and water level variations on wave propagation was also considered, with an update frequency of 1 h, the same frequency in which the wave forcing was updated in MOHID. The oblique angle of the waves’ incidence generates a nearshore longitudinal current oriented to the estuary inlet (Figure 5.13), reinforcing the velocities observed in the scenario in which the wave action was neglected. The velocity vectors have a shoreward component at the surface, whereas near the bottom a seaward component is observed, caused by the vertical variation of the wave-induced forces. Although the currents were intensified along the coast of the Costa da Caparica, a small reduction of velocities can be observed in the northern part of the model domain.

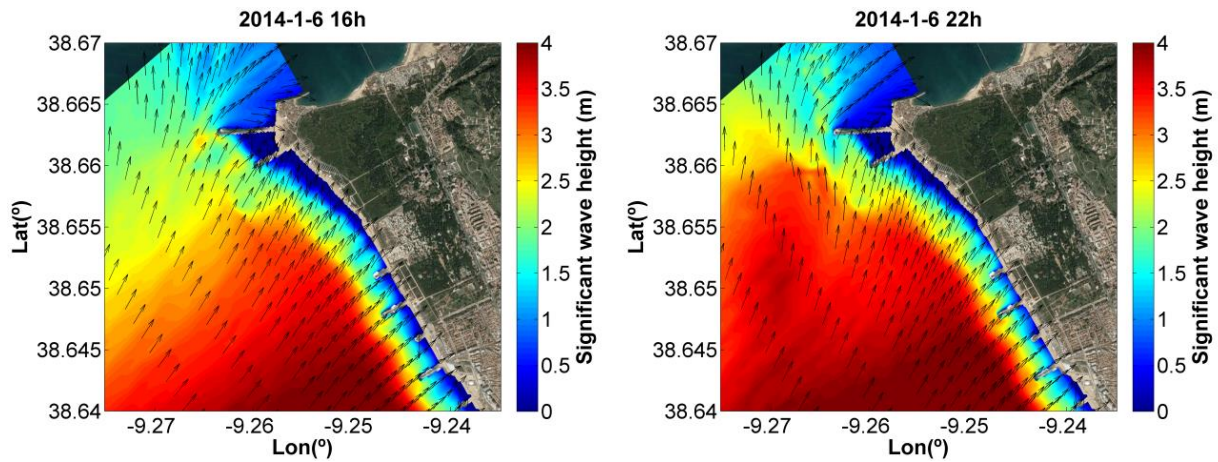


Figure 5.12 – Wave results of the Costa da Caparica model.

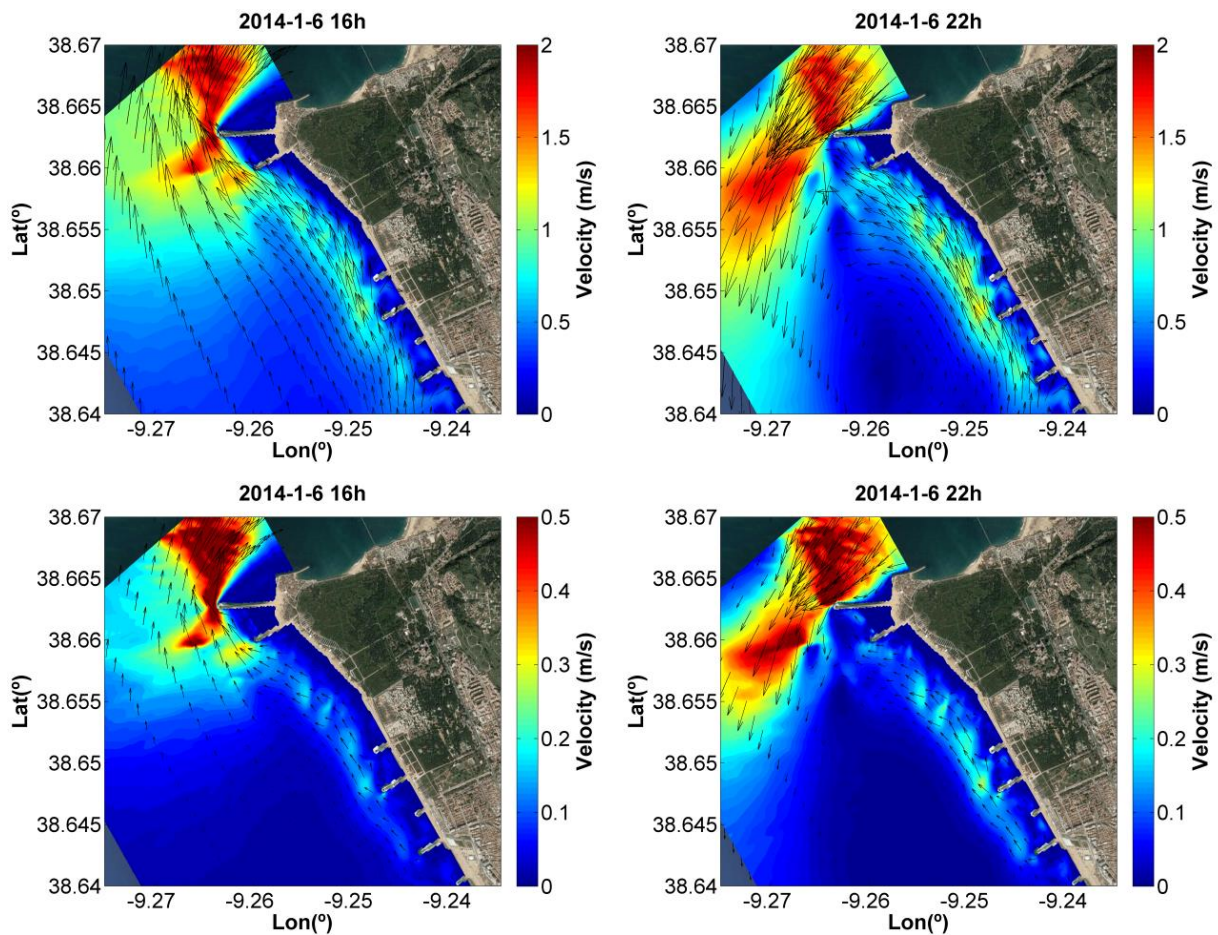


Figure 5.13 - Velocity results of the Costa da Caparica model during the flood (left) and ebb (right) tides at the surface (above) and near the bottom (below) considering the wave's effect on the hydrodynamics.

Based on few existing data in the literature, a uniform granulometry was assumed for the Costa da Caparica model with a mean diameter of 0.3 mm (Freire et al., 2006). A more representative set of

granulometry data is necessary to better characterise the sediment distribution in the model domain, considering that grain-size sorting is expected to occur due to the complex hydrodynamics, wave variability and bathymetric heterogeneities. Thus, the results of sediment transport should be seen as a first qualitative assessment. Moreover, the morphological evolution was ignored at this stage.

The patterns of the bed load sediment transport for the scenarios without waves and under extreme wave conditions are presented in Figure 5.14. Along the coast of the Costa da Caparica, the results of the bed load sediment transport are practically null when the wave action was disregarded, suggesting that the tidal currents are irrelevant for the sediment transport in this area. Although, the importance of the tidal currents for the sediment transport in the inlet of the Tagus Estuary is noticeable. The littoral drift caused by the waves is deflected seaward by the tidal currents during the ebb tide and by the longer groynes present near the estuary inlet.

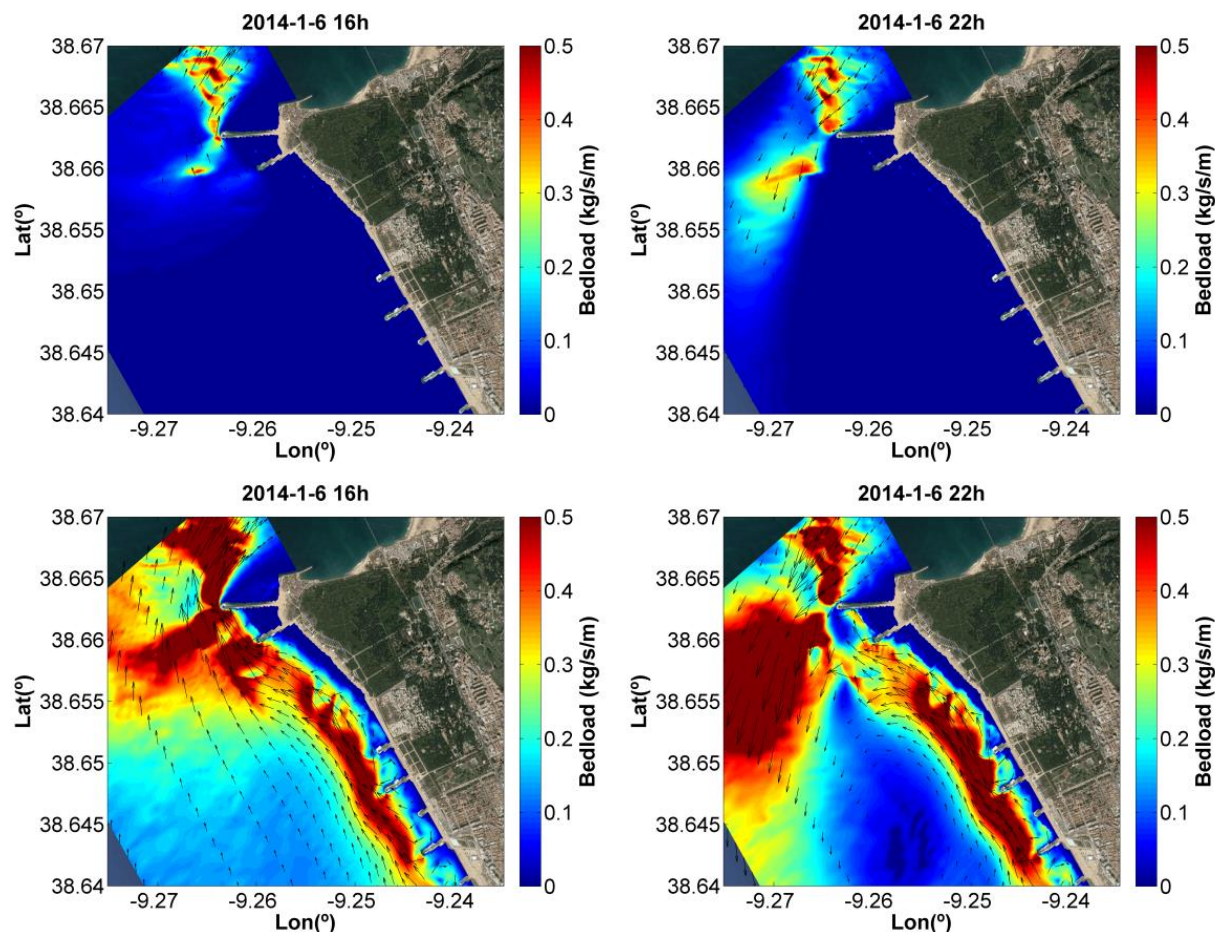


Figure 5.14 – Results of bed load sediment transport for the scenarios without waves (above) and under extreme wave conditions (below).

## 5.5 Conclusions

The potential of a new modelling approach to simulate the impact of different designs of coastal defence structures was demonstrated in this paper. The coupling between the MOHID modelling system and the SWAN wave model can be useful for engineering studies in order to evaluate the best solution to protect the coast against erosion. The speed-up of morphological changes, along with the multiprocessing architecture, allows for the modelling of bed evolution for long periods and for the study of several scenarios. A more efficient coupling method is currently being developed inside the MOHID code to further reduce the computational time. Moreover, the interface of the MOHID modelling system (MOHID Studio) is being developed to make the coupling with SWAN straightforward for all users.

The potential for modelling the evolution of sandbars was also demonstrated in this paper. In the future, an up-to-date methodology can be applied to resolve the vertical variation of wave-induced forces, as well as wave-induced vertical mixing, based on, e.g., the Generalised Lagrangian Mean (GLM) theory implemented in MOHID code (see Delpey et al., 2014). The test cases showed in this paper are only a preliminary demonstration of model potential, which is thought to be encouraging. The findings of this work confirmed the applicability of the MOHID modelling system to study sediment transport and morphological changes in coastal systems under the combined action of waves and currents.

The application of the described modelling methodology to a coastal zone located near the inlet of a mesotidal estuary with strong tidal currents allowed for an assessment of the hydrodynamics and sediment transport in situations of calm water conditions (no waves) and under extreme wave conditions. Although these initial results are just a qualitative assessment of sediment transport, the applicability of the modelling methodology to complex cases was demonstrated. In the future, with a more representative set of data, quantitative studies could be performed, taking into account the morphological evolution. Furthermore, the methodology can be used to evaluate different designs of defence structures in order to propose a more efficient solution for the coastline retreat and intense erosion observed in the last years on the coast of the Costa da Caparica.



## Chapter 6 General Conclusions

The central aim of this thesis was to develop and test a numerical modelling approach for the study of hydrodynamics and sediment transport in coastal systems, in order to support an effective coastal management. The achievement of this aim was confirmed through the application and validation of model results for the wide range of cases described in this thesis. Below, the accomplishment of each specific objective is discussed.

### 6.1 Hydrodynamic modelling of coastal systems

*Objective: Apply a hydrodynamic model to an estuarine system through a downscaling approach from regional scale to local scale.*

The downscaling approach with nested models was applied to the south-eastern Brazilian shelf (regional model) and Paranaguá estuarine system (local model). Previous studies demonstrated the applicability of the MOHID modelling system following a downscaling approach. However, studies performed considering three-dimensional baroclinic models were restricted almost only for the Western Iberian Coast (e.g. Mateus et al., 2012a). In this work, a three-dimensional baroclinic model was applied to the Brazilian coast in a zone where the broad shelf width generates interesting phenomena (e.g. tidal resonance) and a strong ocean current (Brazil current) is present.

The methodology adopted in order to provide realistic oceanic boundary conditions (e.g. water levels, currents, temperature, salinity) to the Paranaguá estuarine system can be extended to other coastal systems located in the Brazilian coast. The outcomes of this work (model results and implementations) were shared with research groups of Brazilian universities (e.g. UERJ, UFPR, UFSC). Moreover, the author has implemented a model for the Guanabara Bay (Rio de Janeiro) with oceanic boundary conditions provided by the same regional model. The idea is to promote a network for the exchange of information and knowledge connected to oceanography research. The network could be enhanced with the implementation of regional models for encompassing other zones along the Brazilian coast.

## 6.2 Modelling of cohesive sediment dynamics in estuarine systems

*Objective: Assess the dynamics of cohesive sediments in an estuarine system following a numerical approach.*

The importance of applying numerical models for assessing the dynamics of cohesive sediments was demonstrated for the Tagus estuary. Through numerical modelling it is possible to integrate over space and time the scarce field data available, helping to understand the complex dynamics of cohesive sediments. Moreover, only numerical models allow for the simulation of different scenarios and the quantification of the effects of different environmental processes. The comprehension of cohesive sediment dynamics in estuarine systems is vital for an effective coastal management, as cohesive sediments are related to several engineering problems (e.g. siltation of harbours, marinas and navigation channels) and environmental concerns (e.g. transport of contaminants and algal growth).

The methodology described in this work permitted the production of realistic results of cohesive sediment concentrations along the Tagus estuary even in a very dry year, representing the fortnightly and daily erosion-sedimentation cycle. This methodology is replicable to other estuarine systems and can be applied following a three-dimensional baroclinic approach for a better characterization of the hydrodynamics and transport. Furthermore, the coupling of MOHID with a wave model will contribute to a better description of the sediment dynamics near estuarine mouths and adjacent coasts.

## 6.3 Morphological modelling of coastal systems

*Objective: Develop a morphological model for multiple sediment fractions (non-cohesive and cohesive) to study sediment dynamics in natural systems.*

The developments performed in the scope of this thesis regarding sediment transport and morphological modelling represent progress that is relevant for the MOHID modelling system. For instance, it is now possible to explicitly account for the suspended transport of non-cohesive sediments, which contributes to a more realistic (smooth) bed evolution. Furthermore, the effects of stratified flows and vertical variation of wave-induced forces can now be taken into account for the suspended transport of non-cohesive sediments by following a three-dimensional approach. The consideration of multiple sediment classes allows for a representation of non-uniform sediment grain distributions, common in estuarine systems. In turn, the multi-layer bottom geometry permits a representation of the bed stratigraphy. The effects of sediment mixtures and bed consolidation on

resistance to erosion also contribute to a more realistic representation of sediment dynamics in natural systems.

## 6.4 Model validation

*Objective: Evaluate the morphological model performance taking into account analytic solutions, experimental and field data.*

The morphological model developed in this work was applied to schematic cases and laboratory experiments in order to evaluate its performance. These test cases included the investigation of the suspended sediment concentrations in a steady uniform flow, the migration of a trench in a flume, the bathymetry evolution of a schematic estuary for hundreds of years and the consolidation of cohesive sediments in a settling column. In another test, the model was applied to the Tagus estuary to investigate the generation of realistic sediment distribution based on the local hydrodynamic conditions. The model applicability was also tested under the combined action of waves and currents. For this purpose, the MOHID modelling system was coupled with the Swan wave model to simulate the impacts of different designs of coastal defence structures and the formation of sandbars on a schematic beach. The modelling methodology was successfully applied to a coastal zone located at the Tagus Estuary mouth (Costa da Caparica) to assess the hydrodynamics and sediment transport in situations of calm water conditions (no waves) and under extreme wave conditions. The outcomes of these test cases confirmed the model potential to be used as a valuable tool for engineering studies.

## 6.5 Future work

The test cases showed in this thesis are only a preliminary demonstration of the morphological model potential. Future applications in natural systems will establish the developed methodology and identify the necessity of further improvements. For instance, the sediment transport in the swash zone was not addressed, which may be a limitation for simulating the beach profile evolution during storm events. A possible manner to overcome this restriction may be the adaptation of the morphological model to run with the non-hydrostatic version of the MOHID hydrodynamic model. The three-dimensional morphological modelling considering the vertical variation of wave-induced forces, based on the Generalised Lagrangian Mean (GLM) theory, is also a prominent topic for future research.

The modular structure of the MOHID modelling system will allow linking the morphological model to other existing models to assess, for instance, the evolution of water properties (e.g., nutrients) or heavy metals (e.g., mercury) in the sediment column and exchanges with the water column.

Moreover, biological effects on sediment resistance to erosion can be taken into account. The development of a persistent fluid mud, considering the movement by gravity, is another field that needs future attention. Although significant advances in the numerical modelling of sediment transport have been observed in recent years, this topic still requires more research effort. The empirical or simplified physical relations necessary to represent small-scale (sub-grid) processes are a great source of uncertainty. The development of more powerful computers can contribute to a better description of natural processes in large-scale morphological models in the future.

## Bibliography

Âmbar, I., Backhaus, J., 1983. A bidimensional numerical model of circulation in the Tejo estuary. Conferência Nacional de Física, Évora.

Amoudry, L.O; Liu, P.L.-F., 2010. Parameterization of near-bed processes under collinear wave and current flows from a two-phase sheet flow model. *Continental Shelf Research*, 30 (13). 1403-1416.

Amoudry, L.O.; Souza, A.J., 2011. Impact of sediment-induced stratification and turbulence closures on sediment transport and morphological modelling. *Continental Shelf Research*, 31 (9). 912-928.

Ardhuin, F., Rascle, N., Belibassakis, K., 2008. Explicit wave averaged primitive equations using a generalized Lagrangian mean. *Ocean Modelling*, 20(1), 35–60, doi:10.1016/j.ocemod.2007.07.001.

Ariathurai, R., Arulanandan, K., 1978. Erosion rates of cohesive soils. *Journal of Hydraulics Division, ASCE*, 104(2), 279–283.

Ascione, I., 2014. Development and application of a process-oriented model for benthic marine systems. PhD thesis, Instituto Superior Técnico, Universidade Técnica de Lisboa, Lisbon, Portugal, 200 pp.

Ascione, K.I., Campuzano, F., Franz, G., Fernandes, R., Viegas, C., Sobrinho, J., de Pablo, H., Amaral, A., Pinto, L., Mateus, M., Neves, R., 2014. Advances in Modeling of Water Quality in Estuaries, in: Finkl, C.W., Makowski, C. (Eds.), *Remote Sensing and Modeling*. Springer International Publishing, pp. 237-276.

Bagnold, R.A., 1996. An approach to the sediment transport problem from general physics. *Geological Survey Professional Paper*, 422-I.

Barros, A.P., 1996. An evaluation of model parameterizations of sediment pathways: A case study for the Tejo estuary. *Continental Shelf Research* 16 no. 13, pp. 1725-1749.

Bettencourt, P., Alcobia, S., Vargas, C. Sousa, G., 2011. Equilíbrios Sedimentares e Passivos Ambientais. In: *O Plano de Ordenamento do Estuário do Tejo*. Administração da Região Hidrográfica do Tejo, Lisbon, pp. 125-130.

Blumberg, A.F., Kantha, L.H., 1985. Open boundary condition for circulation models. *Journal of Hydraulic Engineering*, 111(2), pp.237-255.

Booij, N., Ris, R.C., Holthuijsen, L.H., 1999. A third-generation wave model for coastal regions, Part I, Model description and validation. *Journal of Geophysical Research* 104 (C4), 7649–7666.

Bowen, A.J., Inman, D.L., Simmons, V.P., 1968. Wave Set-Down and Wave Set-Up. *Journal of Geophysical Research*, 73(8), 2569-2577.

Bricheno, L.M., Wolf, J.M. and Brown, J.M., 2014. Impacts of high resolution model downscaling in coastal regions. *Continental Shelf Research*, 87, pp.7-16.

Brito, D., Campuzano, F.J., Sobrinho, J., Fernandes, R., Neves, R., 2015. Integrating operational watershed and coastal models for the Iberian Coast: Watershed model implementation – A first approach. *Estuarine, Coastal and Shelf Science*, 167 (Part A), 138-146.

Buchard, H., Bolding, K., Villarreal, M.R., 1999. GOTM, a General Ocean Turbulence Model. Theory, implementation and test cases. Report EUR18745 EN, European Commission, 103 pp.

Burt, T.N., 1984. Field settling velocities of estuary muds. In: *Estuarine Cohesive Sediment Dynamics*, Springer-Verlag, Berlin, pp.126-50.

Caçador, I., Caetano, M., Duarte, B., Vale, C., 2009. Stock and losses of trace metals from salt marsh plants. *Marine Environmental Research* 67, 75–82.

Caçador, I., Duarte, B., 2012. Tagus estuary salt marsh structure and dynamics: A historical perspective. In: *Estuaries: Classification, ecology and human impacts*, Jordan, S.J. (ed.). Nova Science Publishers, pp. 41-56.

Camargo, R., Harari, J., 1994. Modelagem numérica de ressacas na plataforma sudeste do Brasil a partir de cartas sinóticas de pressão atmosférica na superfície. *Boletim do Instituto Oceanográfico da USP* 42 (1), 19–34.

Camargo R., Harari J., 2003. Modeling of the Paranaguá estuarine complex, Brazil: tidal circulation and cotidal charts. *Revista Brasileira de Oceanografia* 51, 23-31.

Campos, E.J.D., Gonçalves, J.E., Ikeda, Y., 1995. Water Mass Characteristics and Geostrophic Circulation in the South Brazil Bight-Summer of 1991. *Journal of Geophysical Research* 100(9), 18537-18550.

Campos, E.J.D., Velhote, D., da Silveira, I.C.A., 2000. Shelf break upwelling driven by Brazil Current cyclonic meanders. *Geophysical Research Letters* 27, 751– 754.

Canário, J., Vale, C., 2007. Monitoring program for the Tagus Estuary and tributaries, Scientific Report, IPIMAR, June 2007, p. 78

Canas, A., dos Santos, A., Leitão, P., 2009. Effect of large scale atmospheric pressure changes on water level in the Tagus Estuary. *Journal of Coastal Research*, SI 56 ICS2009 (Proceedings), pp. 1627 – 1631, ISSN 0749-0258.

Cancino, L., Neves, R., 1999a. Hydrodynamic and sediment suspension modelling in estuarine systems: Part I. Description of the numerical models. *Journal of Marine Systems* 22, pp. 105–116.

Cancino, L., Neves, R., 1999b. Hydrodynamic and sediment suspension modelling in estuarine systems: Part II. Application to the western Scheldt and Gironde estuaries. *Journal of Marine Systems* 22, pp. 117–131.

Carrère, L., Lyard, F., Cancet, M., Guillot, A., Roblou, L., 2012. FES2012: A New Global Tidal Model Taking Advantage of Nearly 20 Years of Altimetry. In *Proceedings of Meeting “20 Years of Altimetry”*, September 24–29. Venice: Esa Publication.

Chauchat, J., Guillou, S., Van Bang, D., P., Nguyen, K.D., 2013. Modelling sedimentation-consolidation in the framework of a one-dimensional two-phase flow model. *Journal of Hydraulic Research* 51 (3), 293-305.

Cummins, P.F., Karsten, R.H., Arbic, B.K., 2010. The semi-diurnal tide in Hudson Strait as a resonant channel oscillation. *Atmosphere-Ocean* 48 (3), 163-176.

Dally, W.R., Pope, J., 1986. Detached breakwaters for shore protection (No. CERC-TR-86-1). COASTAL ENGINEERING RESEARCH CENTER VICKSBURG MS.

Dean, R.G., 1991. Equilibrium beach profiles: characteristics and applications. *Journal of coastal research*, pp.53-84.

Delpy, M.T., Ardhuin, F., Otheguy, P., Jouon, A., 2014. Effects of waves on coastal water dispersion in a small estuarine bay, *J. Geophys. Res. Oceans*, 119, 70–86, doi:10.1002/2013JC009466.

Dias, J.M., Valentim J.M., Sousa M.C., 2013. A Numerical Study of Local Variations in Tidal Regime of Tagus Estuary, Portugal. *PLoS ONE* 8(12): e80450. doi:10.1371/journal.pone.0080450

Dolan, T.J., Dean, R.G., 1985. Multiple longshore sand bars in the upper Chesapeake Bay. *Estuarine, Coastal and Shelf Science*, 21(5), pp.727-743.

Drønen, N., Deigaard, R., 2007. Quasi-three-dimensionnal modelling of the morphology of longshore bars. *Coastal Engineering*, 54, pp. 197–215.

Droppo, I.G., 2001. Rethinking what constitutes suspended sediment. *Hydrological Processes* 15, 1551-1564.

Duarte, B., Reboreda, R., Caçador, I., 2008. Seasonal variation of Extracellular Enzymatic Activity (EEA) and its influence on metal speciation in a polluted salt marsh. *Chemosphere* 73, 1056–1063.

Dubarbier, B., Castelle, B., Marieu, V., Ruessink, G., 2015. Process-based modelling of cross-shore sandbar behaviour. *Coastal Engineering*, 95. pp. 35–50.

Dyer, K.R., 1986. *Coastal and Estuarine Sediment Dynamics*. Wiley-Interscience, 342 pp.

Einstein, H. A., 1950. The Bed-Load Function for Sediment Transportation in Open Channel Flows. United States Department of Agriculture, Washington, D.C., Technical Bulletin No. 1026, p.25.

Engedahl, H., 1995. Use of the flow relaxation scheme in a three-dimensional baroclinic ocean model with realistic topography. *Tellus*, v. 47, n. 3, p. 365–382.

Engelund, F., Fredsoe, J., 1976. A sediment transport model for straight alluvial channels. *Nordic Hydrology* 7, 293-306.

Fernandes, R., Braunschweig, F., Lourenço, F., Neves, R., 2016. Combining operational models and data into a dynamic vessel risk assessment tool for coastal regions. *Ocean Science*, 12, 285-317.

Fernandez Luque, R., Van Beek, R., 1976. Erosion and transport of bed-load sediment. *Journal of hydraulic research*, 14(2), 127-144.

Flather, R. A., 1976. A tidal model of the north-west European continental shelf. *Memoires de la Society Royal des Sciences de Liege*, 6 series, 10, 141-164.

Franz, G., Pinto, L., Ascione, I., Mateus, M., Fernandes, R., Leitão, P., Neves, R., 2014a. Modelling of cohesive sediment dynamics in tidal estuary systems: case study of Tagus estuary, Portugal. *Estuarine, Coastal and Shelf Science* 151, 34-44.

Franz, G., Fernandes, R., de Pablo, H., Viegas, C., Pinto, L., Campuzano, F.J., Ascione, I., Leitão, P., Neves, R., 2014b. Tagus Estuary hydro-biogeochemical model: Inter-annual validation and

operational model update. 3.as Jornadas de Engenharia Hidrográfica, Lisbon, Portugal. Extended abstracts: 103-106.

Franz, G., Campuzano, F., Fernandes, R., Pinto, L., de Pablo, H., Ascione, I., Neves, R., 2014c. An integrated forecasting system of hydro-biogeochemical and waves in the Tagus estuary. Proceedings of the Seventh EuroGOOS International Conference, Lisbon.

Franz, G., Campuzano, F., Pinto, L., Fernandes, R., Sobrinho, J., Simões, A., Juliano, M., Neves, R., 2014d. Implementation and validation of a wave forecasting system for the Portuguese Coast. Proceedings of the Seventh EuroGOOS International Conference, Lisbon.

Franz, G.A.S., Leitão, P., Santos, A., Juliano, M., Neves, R., 2016. From regional to local scale modelling on the south-eastern Brazilian shelf: case study of Paranaguá estuarine system. *Brazilian Journal of Oceanography*, 64(3), 277-294.

Freire, P., 2003. Evolução Morfo-Sedimentar de Margens Estuarinas. Estuário do Tejo, Portugal. PhD Thesis. Lisbon University, 380 p.

Freire, P., Taborda, R., Andrade, C., 2006. Caracterização das praias estuarinas do Tejo. In APRH, Congresso da Água (Vol. 8).

Foreman, M.G.G., 1996. Manual for Tidal Heights Analysis and Prediction. Pacific Marine Science Report, 77-10, Institute of Ocean Sciences, Patricia Bay, Sidney, B.C.

Fortunato, A.B., Baptista, A.M., Luettich, R.A. , 1997. A three-dimensional model of tidal currents in the mouth of the Tagus estuary. *Continental Shelf Research* 17, pp. 1689-1714.

Fortunato, A.B., Oliveira, A., Baptista, A.M., 1999. On the Effect of Tidal Flats on the Hydrodynamics of the Tagus Estuary. *Oceanologica Acta*, 22(1):31-44.

Gameiro, C., Cartaxana, P., Brotas, V., 2007. Environmental drivers of phytoplankton distribution and composition in Tagus estuary, Portugal. *Estuarine, Coastal and Shelf Science* 75, 21–34.

Gameiro, C., Zwolinski J., Brotas, V., 2011. Light control on phytoplankton production in a shallow and turbid estuarine system. *Hydrobiologia* 669, 249–263.

Garcia, M., Parker, G., 1991. Entrainment of bed sediment into suspension. *Journal of Hydraulic Engineering* 117 (4), 414–435.

Garcia, M.H. ed., 2008. Sedimentation engineering: Processes, measurements, modeling, and practice (Vol. 110). ASCE Publications.

Gouillon, F., Morey, S.L., Dukhovskoy, D.S., O'Brien, J.J., 2010. Forced tidal response in the Gulf of Mexico. *Journal of Geophysical Research-Oceans* 115 (C10050).

Grasso, F., Le Hir, P., Bassoullet, P., 2015. Numerical modelling of mixed-sediment consolidation. *Ocean Dynamics* 65, 607-616.

Greenwood, R., Davis, R.A., 2011. *Hydrodynamics and sedimentation in wave-dominated coastal environments* (Vol. 39). Elsevier.

Hamm, L., Migniot, C., 1994. Elements of cohesive sediment deposition, consolidation and erosion, in *Coastal, Estuarial and Harbour Engineers's Reference Book*, MB Abbot and WA Price, eds., Spon Press, London, pp. 93-106.

Harari, J., Camargo, R., 1994. Simulação da propagação das nove principais componentes de maré na plataforma sudeste brasileira através de modelo numérico hidrodinâmico. *Boletim do Instituto Oceanográfico da USP* 42 (1), 35-54.

Hayter, E.J., Mehta, A.J., 1986. Modelling cohesive sediment transport in estuarial waters. *Applied Mathematical Modelling* 10, 294-303.

Huthnance, J.M., 1980. On shelf-sea resonance with application to Brazilian M3 tides. *Deep-Sea Research Part A Oceanographic Research Papers* 27 (5), 347-366.

Ikeda, S., 1982. Lateral bed-load transport on side slopes. *Journal of the Hydraulics Division* 108 (11), 1369-1373.

Jouanneau, J.M, Garcia, C., Oliveira, A., Rodrigues., A., Dias, J.A., Weber, O., 1998. Dispersal and deposition of suspended sediment on the shelf off the Tagus and Sado estuaries, S.W. Portugal. *Progress in Oceanography* 42, 233-257.

Kang, S.W., Sheng, J.P., Lick, W., 1982. Wave Action and Bottom Shear Stress in Lake Eire. *Journal of Great Lake Research*, 8(3), pp. 482-494.

Kantha, L., Whitmer, K., Born, G. 1994. The inverted barometer effect in altimetry: a study in the North Pacific. *TOPEX/Poseidon Res. News* 2:18-23.

Kantha, L.H., Clayson, C.A., 2000. *Numerical Models of Oceans and Oceanic Processes*. International Geophysics Series. Volume 66. Academic Press.

Kleinhans, M.G., Grasmeyer, B.T., 2006. Bed load transport on the shoreface by currents and waves. *Coastal Engineering*, 53(12), 983-996.

Koltermann, C.E., Gorelick, S.M., 1995. Fractional packing model for hydraulic conductivity derived from sediment mixtures. *Water Resources Research* 31, 3283–3297.

Komar, P.D., 1998. *Beach processes and sedimentation*. Prentice-Hall, New Jersey.

Kriebel, D.L., Dean, R.G., 1985. Numerical simulations of time-dependent beach and dune erosion. *Coastal Engineering*, 9, 221–245.

Kristensen, S., Dronen, N., Deigaard, R., Fredsoe, J., 2013. Hybrid morphological modelling of shoreline response to a detached breakwater. *Coastal Engineering*, 71, pp. 13–27.

Krone, R. B., 1962. Flume studies of the transport of sediment in estuarial shoaling processes. Hydraulic Engineering Laboratory and Sanitary Engineering Research Laboratory, University of California, Berkeley, 110 pp.

Kynch, G. J., 1952. A theory of sedimentation. *Transactions of the Faraday Society* 48, 166-176.

Lefèvre, F., Lyard, F.H., Le Provost, C., and Schrama, E.J.O, 2002. FES99: A Global Tide Finite Element Solution Assimilating Tide Gauge and Altimetric Information. *Journal of Atmospheric and Oceanic Technology* 19, 1345–1356.

Le Hir, P., Cayocca, F., Waeles, B., 2011. Dynamics of sand and mud mixtures: A multiprocess-based modelling strategy. *Continental Shelf Research* 31, S135-S149.

Leitão, P., 2003. *Integração de Escalas e de Processos na Modelação no Ambiente Marinho*. Ph.D thesis, Instituto Superior Técnico, Universidade Técnica de Lisboa, Lisbon, Portugal, 296 pp.

Leitão, P.C., Mateus, M., Braunschweig, F., Fernandes L. and Neves, R., 2008. Modelling coastal systems: the MOHID Water numerical lab. In: R. Neves, J. Baretta & M. Mateus (Eds.), *Perspectives on Integrated Coastal Zone Management in South America*. IST Press, Lisbon, pp 77-88.

Lemos, P.A.F. 1972. *Estuário do Tejo*. Administração Geral do Porto de Lisboa, Lisbon.

Lesser, G.R., Roelvink, J.A., van Kester, J.A.T.M., Stelling, G.S., 2004. Development and validation of a three-dimensional morphological model. *Coastal Engineering* 51, 883–915.

Lesser, G.R., 2009. *An approach to medium-term coastal morphological modelling*. PhD thesis, Delft University of Technology, Delft, The Netherlands.

Levoy, F., Anthony, E.J., Monfort, O. and Larssonneur, C., 2000. The morphodynamics of megatidal beaches in Normandy, France. *Marine Geology*, 171(1), pp.39-59.

Longuet-Higgins, M.S., Stewart, R.W., 1962. Radiation stress and mass transport in gravity waves, with application to 'surf beats'. *Journal of Fluid Mechanics*, 13(04), pp.481-504.

Longuet-Higgins, M.S., Stewart, R.W., 1964. Radiation stresses in water waves; a physical discussion, with applications. *Deep Sea Research and Oceanographic Abstracts*, Vol. 11 (4), pp. 529-562.

Longuet-Higgins, M.S., 1970a. Longshore currents generated by obliquely incident sea waves: 1. *Journal of geophysical research*, 75(33), pp.6778-6789.

Longuet-Higgins, M.S., 1970b. Longshore currents generated by obliquely incident sea waves: 2. *Journal of geophysical research*, 75(33), pp.6790-6801.

Longuet-Higgins, M.S., 1983. Wave set-up, percolation and undertow in the surf zone. In *Proceedings of the Royal Society of London A: Mathematical, Physical and Engineering Sciences* (Vol. 390, No. 1799, pp. 283-291). The Royal Society.

Lyard, F., Lefèvre, F., Letellier, T., Francis, O., 2006. Modelling the global ocean tides: modern insights from FES2004, *Ocean Dynamics* 56, 394-415.

Malhadas, M.S., Leitão, P.C., Silva, A., Neves, R., 2009. Effect of coastal waves on sea level in Óbidos Lagoon. *Continental Shelf Research*, *Continental Shelf Research* 29 (9), pp. 1240-1250.

Malhadas, M.S., Neves, R., Leitão, P.C., Silva, A., 2010. Influence of tide and waves on water renewal in Óbidos Lagoon, Portugal. *Ocean Dynamics* 60, pp. 41-55.

Maraldi, C., Chanut, J., Levier, B., Ayoub, N., De Mey, P., Refray, G., Lyard, F., Cailleau, S., Drévilion, M., Fanjul, E., Sotillo, M.G., 2013. NEMO on the shelf: assessment of the Iberia-Biscay-Ireland configuration. *Ocean Science*, 9, pp.745-771.

Martins, F., 2000. *Modelação Matemática Tridimensional de escoamentos costeiros e estuarinos usando uma abordagem de coordenada vertical genérica*. PhD thesis, Universidade Técnica de Lisboa, Instituto Superior Técnico, Lisbon, Portugal.

Martins, F., Leitão, P.C., Silva, A., Neves, R., 2001. 3D modelling in the Sado estuary using a new generic vertical discretization approach. *Oceanologica Acta* 24, 551-562.

Martinsen, E.A., Engedahl, H., 1987. Implementation and testing of a lateral boundary scheme as an open boundary condition in a barotropic ocean model. *Coastal Engineering* 11, 603-627.

Mateus, M., 2006. *A process-oriented biogeochemical model for marine ecosystems: Development, numerical study and application*. PhD thesis. Technical University of Lisbon, Portugal.

Mateus, M., Neves, R., 2008. Evaluating light and nutrient limitation in the Tagus estuary using a process-oriented ecological model. *Journal of Marine Engineering and Technology* 12A, 43-54.

Mateus, M., Riflet, G., Chambel, P., Fernandes, L., Fernandes, R., Juliano, M., Campuzano, F., de Pablo, H., Neves, R., 2012a. An operational model for the West Iberian coast: products and services, *Ocean Science* 8, 713-732.

Mateus, M., Vaz, N., Neves, N., 2012b. A process-oriented model of pelagic biogeochemistry for marine systems. Part II: Application to a mesotidal estuary. *Journal of Marine Systems* 94, S90-S101.

Mehta, A.J., 1986. Characterisation of cohesive sediment properties and transport processes in estuaries. In: Mehta, A.J. (ed.), *Estuarine Cohesive Sediment Dynamics* 14, Springer-Verlag, Berlin, pp. 290–325.

Mesquita, A.R., Harari, J., 2003. On the harmonic constants of tides and tidal currents of the South-eastern Brazilian shelf. *Continental Shelf Research* 23, 1227-1237.

Meyer-Peter, E., Müller, R., 1948. Formulas for bed-load transport. Proc., 2nd IAHR Congress, Stockholm, Sweden, 39-64.

Migniot, C., 1968. Etude des propriétés physiques de différents sédiments très fins et de leur comportement sous les actions hydrodynamiques. *La Houille Blanche*, 7, 591-620.

Mitchener, H., Torfs, H., 1996. Erosion of mud/sand mixtures. *Coastal Engineering*, 29, pp. 1–25.

Monteiro, A.J., 1995. Dispersão de Efluentes Através de Exutores Submarinos. Uma contribuição para a modelação matemática. Tese de doutoramento. Universidade Técnica de Lisboa, Instituto Superior Técnico.

Mulder, H.P.J., Udink, C., 1991. Modelling of cohesive sediment transport. A case study: the western Scheldt estuary. In: Edge, B.L. (ed.). *Proceedings of the 22nd International Conference on Coastal Engineering*. American Society of Civil Engineers, New York, pp. 3012–3023.

Murray, W.A., 1977. Erosion of coarse sand–clayey silt mixtures. *Journal of Hydraulics Division, ASCE*, 103 (HY10), 1222–1227.

Myrhaug, D., Holmedal, L.E., Rue, H., 2004. Bottom friction and bedload sediment transport caused by boundary layer streaming beneath random waves. *Applied Ocean Research*, 26(5), pp.183-197.

Neves, F.J., 2010. Dynamics and Hydrology of the Tagus Estuary: Results from In Situ Observations. PhD thesis, Universidade de Lisboa, Lisbon, Portugal, 210 pp.

Neves, R.J.J., 1985. Étude Experimentale et Modélisation des Circulations Transitoire et Résiduelle dans l'Estuaire du Sado, Ph. D. Thesis, Univ. Liège, 371 pp.

Nicholson, J., O'Connor, B.A., 1986. Cohesive sediment transport model, *Journal of Hydraulic Engineering* 112, 621-639.

Noernberg, M.A., Lautert, L.F.C., Araújo, A.D., Marone, E., Angelotti, R., Netto Jr, J.P.B., Krug, L.A., 2006. Remote sensing and GIS integration for modelling the Paranaguá estuarine complex- Brazil. *Journal of Coastal Research* 39, pp. 1627–1631.

Nogueira Mendes, R., Ceia, R., Silva, T., Rilo, A., Guerreiro, M., Catalão, J., Taborda, R., Freitas, M. C., Andrade, A., Melo, R., Fortunato, A.B., Freire, P., 2012. Remote sensing and intertidal cartography. Contribution of the MorFeed project. *Actas das 2.as Jornadas de Engenharia Hidrográfica*, 341-344.

Odamaki, M., 1989. Co-oscillating and independent tides of the Japan Sea. *Journal of the Oceanographical Society of Japan* 45 (3), 217-232.

Pairaud, I.L., Lyard, F., Auclair, F., Letellier, T., Marsaleix, P., 2008. Dynamics of the semi-diurnal and quarter-diurnal internal tides in the Bay of Biscay. Part 1: barotropic tides. *Continental Shelf Research* 28 (10–11), pp. 1294–1315.

Panagiotopoulos, I., Voulgaris, G., Collins, M.B., 1997. The influence of clay on the threshold of movement on fine sandy beds. *Coastal Engineering* 32, 19–43.

Papanicolaou, A.T.N., Elhakeem, M., Krallis, G., Prakash, S., Edinger, J., 2008. Sediment transport modeling review—current and future developments. *Journal of Hydraulic Engineering*, 134(1), pp.1-14.

Parker, B.B., 1991. The relative importance of the various nonlinear mechanisms in a wide range of tidal interactions (review), in *Tidal Hydrodynamics*, edited by B.B. Parker, pp. 237-268, John Wiley, New York.

Partheniades, E., 1965. Erosion and deposition of cohesive soils. *ASCE Journal of Hydraulic Division* 91 (HY1), 105–139.

Pawlowicz, R., Beardsley, B., Lentz, S., 2002. Classical tidal harmonic analysis including error estimates in MATLAB using T\_TIDE. *Computers and Geosciences* 28, 929–937.

Pereira, A.F., Castro, B.M., 2007. Internal tides in the southwestern Atlantic off Brazil: observations and numerical modelling. *Journal of Physical Oceanography*, 37(6), 1512-1526.

Pereira, A.F., Castro, B.M., Calado, L., Silveira, I.C.A., 2007. Numerical simulation of M2 internal tides in South Brazil Bight and their interaction with the Brazil Current. *Journal of Geophysical Research*, 112(C04009).

Pinto, L., Fortunato, A.B., Zhang, Y., Oliveira, A., Sancho, F.E.P., 2012. Development and validation of a three-dimensional morpho-dynamic modelling system for non-cohesive sediments. *Ocean Modelling*, 57-58: 1-14.

Portela, L.I., Neves, R., 1994. Numerical modelling of suspended sediment transport in tidal estuaries: a comparison between the Tagus (Portugal) and the Scheldt (Belgium-The Netherlands). *Netherlands Journal of Aquatic Ecology* 28, 329-335.

Portela, L.I., 1996. *Modelação Matemática da Hidrodinâmica e dos Processos de Qualidade da Água no Estuário do Tejo*. PhD thesis, Instituto Superior Técnico, Universidade Técnica de Lisboa, Lisbon, Portugal.

Portela, L.I., 1997. Effect of settling velocity on the modelling of suspended sediment transport. In: Acinas, J.R. and Brebbia, C.A. (eds.), *Computer Modelling of Seas and Coastal Regions III*. Southampton, United Kingdom. Computational Mechanics Publications, pp. 347-403.

Portela, L.I., Ramos, S., Teixeira, A.T., 2013. Effect of salinity on the settling velocity of fine sediments of a harbour basin. In: Conley, D.C., Masselink, G., Russell, P.E., O'Hare, T.J. (eds.), *Proceedings 12<sup>th</sup> International Coastal Symposium (Plymouth, England)*. *Journal of Coastal Research*, Special Issue No. 65, pp. 1188-1193, ISSN 0749-0208.

Pugh, D.T., Woodworth, P.L., 2014. *Sea-Level Science: Understanding Tides, Surges Tsunamis and Mean Sea-Level Changes*, 407 p.p., Cambridge Univ. Press, Cambridge, U.K.

Puls, W., Kuehl, H., 1986. Field measurements of the settling velocities of estuarine flocs, in *Proceedings of the Third International Symposium On River Sedimentation*, March 31 – April 14, 1986, Jackson, Mississippi. ASCE, New York, pp. 525-36.

Raudkivi, A.J., 1990. *Loose Boundary Hydraulics (3rd ed.)*. Oxford: Pergamon Press.

Ribberink, J. S., 1998. Bed-load transport for steady flows and unsteady oscillatory flows. *Coastal Engineering*, 34(1), 59-82.

Riflet, G., 2010. *Downscaling large-scale ocean basin solutions in regional three-dimensional hydrodynamic models*. PhD thesis. Technical University of Lisbon, Portugal.

Roelvink, D., Reniers, A., Van Dongeren, A.P., de Vries, J.V.T., McCall, R., Lescinski, J., 2009. Modelling storm impacts on beaches, dunes and barrier islands. *Coastal engineering*, 56(11), pp.1133-1152.

Rouse, H., 1937. Modern conceptions of mechanics of turbulence. *Transactions of American Society of Civil Engineers*, 102, 436–505.

Ruessink, B.G., Kuriyama, Y., Reniers, A.J.H.M., Roelvink, J.A., Walstra, D.J.R., 2007. Modeling cross-shore sandbar behavior on the time scale of weeks. *Journal of Geophysical Research*, 112 (F3), pp. 1–15.

Ruessink, B. G., Pape, L., Turner, I.L., 2009. Daily to interannual cross-shore sandbar migration: observations from a multiple sandbar system. *Continental Shelf Research*, 29(14), pp.1663-1677.

Salgueiro, N., Caçador, I., 2007. Short-term sedimentation in Tagus estuary, Portugal: the influence of salt marsh plants. *Hydrobiologia* 587, 185–193.

Sanford, L.P., Halka, J.P., 1993. Assessing the paradigm of mutually exclusive erosion and deposition of mud, with examples from upper Chesapeake Bay. *Marine Geology* 114, 37–57.

Sanford, L., 2008. Modeling a dynamically varying mixed sediment bed with erosion, deposition, bioturbation, consolidation and armouring. *Computers and Geosciences* 34, 1263–1283.

Santoro, P.E., Fossati M., Piedra-Cueva, I., 2013. Study of the meteorological tide in the Río de la Plata. *Continental Shelf Research*, 60, 51-63.

Santos, A.J.P., 1995. Modelo hidrodinâmico tridimensional de circulação oceânica e estuarina. Tese de doutoramento. Instituto Superior Técnico, Universidade Técnica de Lisboa, 273 pp., Lisboa.

Saraiva, S., 2014. Modelling Bivalves in estuaries and coastal areas. PhD thesis. Amsterdam: Vrije Universiteit and Instituto Superior Técnico, Universidade de Lisboa.

Saville, T., 1961. Experimental determination of wave set-up, In Proc. 2nd Tech. Conf. on Hurricanes, Miami Beach, FL., Nat. Hurricane Res. Proj. Rep. 50, pp. 242-252.

Seymour, R.J., 1977. Estimating Wave Generation in Restricted Fetches. *J. ASME WW2*, pp251-263.

Shields, A., 1936. Application of similarity principles and turbulent research to bed-load movement (Mitteilungen der Preussischer Versuchsanstalt für Wasserbau und Schiffen, Berlin), in: W. M. Keck Laboratory of Hydraulics and Water Resources, Report 167 (W. P. Ott and J. C. van Uchelen, translators), California Institute of Technology, Pasadena, California.

Silva, A.J.R., 1991. *Modelação Matemática Não Linear de Ondas de Superfície e de Correntes Litorais*, Tese apresentada para obtenção do grau de Doutor em Engenharia Mecânica. IST, Lisboa.

Smagorinsky, J., 1963. General circulation experiments with the primitive equations: I. The basic experiment. *Monthly weather review*, 91(3), pp.99-164.

Smith, J. D., McLean, S. R., 1977. Spatially averaged flow over a wavy surface, *Journal of Geophysical Research*, 82 (12), 1735–1746.

Soulsby, R.L., Damgaard, J.S., 2005. Bedload sediment transport in coastal waters. *Coastal Engineering* 52, 673-689.

Soulsby, R.L., Clarke, S., 2005. Bed shear-stresses under combined waves and currents on smooth and rough beds. *Hydraulics research report TR 137*.

Soulsby, R.L., Manning, A.J., Spearman, J., Whitehouse, R.J.S., 2013. Settling velocity and mass settling flux of flocculated estuarine sediments. *Journal of Marine Geology* 339, 1-12.

Toorman, E.A., Berlamont, J.E., 1993. Mathematical modeling of cohesive sediment settling and consolidation. In A. J. Mehta, *Nearshore and estuarine cohesive sediment transport*. Washington, DC: American Geophysical Union, 167–184.

Toorman, E.A., 1999. Sedimentation and self-weight consolidation: constitutive equations and numerical modelling. *Géotechnique* 49, No. 6, 709-726.

Torfs, H., Mitchener, H., Huysentruyt, H., Toorman, E., 1996. Settling and consolidation of mud/sand mixtures. *Coastal Engineering* 29, 27-45.

Trancoso, A.R., 2012. *Operational Modelling as a Tool in Wind Power Forecasts and Meteorological Warnings*. PhD thesis. Technical University of Lisbon, 120 pp.

Vale, C., 1981. Input of suspended particulate matter in the Tagus estuary during the flood of February 1979. *Recursos Hidricos* 2, 37–45.

Vale, C., Sundby, B., 1987. Suspended sediment fluctuations in the Tagus estuary on semi-diurnal and fortnightly time scales. *Estuarine, Coastal and Shelf Science* 25, 495–508.

Vale, C., 1990. Temporal variations of particulate metals in the Tagus river estuary. *Science of the Total Environment* 97/98, 137–154.

Valente, A.S., Silva, J.C.B., 2009. On the observability of the fortnightly cycle of the Tagus estuary turbid plume using MODIS ocean colour images. *Journal of Marine Systems* 75, pp. 131-137.

Van, L.A., Pham Van Bang, D., 2013. Hindered settling of sand/mud flocc mixtures: From model formulation to numerical validation. *Advances in Water Resources* 53, 1-11.

van der Wegen, M., Jaffe, B.E., Roelvink J.A., 2011. Process-based, morphodynamic hindcast of decadal deposition patterns in San Pablo Bay, California, 1856–1887, *Journal of Geophysical Research* 116, F02008, doi:10.1029/2009JF001614.

van Ledden, M., 2003. Sand-mud segregation in estuaries and tidal basins. PhD thesis. Repository TU Delft, 221 p.

van Leussen, W., 1988. Aggregation of particles, settling velocity of mud flocc – a review, in *Physical Processes in Estuaries*, Springer-Verlag, Berlin, pp. 347-403.

van Rijn, L.C., 1984. Sediment Transport, Part II: Suspended Load Transport. *Journal of Hydraulic Engineering* 110 (11).

van Rijn, L.C., 1987. *Mathematical Modeling of Morphological Processes in the Case of Suspended Sediment Transport*. Delft Technical University, Delft, The Netherlands.

van Rijn, L.C., 1993. *Principles of Sediment Transport in Rivers, Estuaries and Coastal Seas*. 715p., Aqua Publications, Amsterdam, Holland. ISBN: 90-800356-2-9.

van Rijn, L.C., 2007a. Unified View of Sediment Transport by Currents and Waves. I: Initiation of Motion, Bed Roughness, and Bed-Load Transport. *Journal of Hydraulic Engineering* 133 (6).

van Rijn, L.C., 2007b. Unified view of sediment transport by currents and waves. II: Suspended Transport. *Journal of Hydraulic Engineering* 133 (6).

van Rijn, L.C., 2007c. Unified view of sediment transport by currents and waves, III: Graded beds *Journal of Hydraulic Engineering* 133 (7).

van Rijn, L.C., 2012. *Principles of sedimentation and erosion engineering in rivers, estuaries and coastal seas*. Aqua Publications, The Netherlands, 580 pp.

Vaz, N., Mateus M., Dias, J.M., 2009. Semidiurnal and spring-neap variations in the Tagus Estuary: Application of a process-oriented hydro-biogeochemical model. SI 64 (Proceedings of the 10th International Coastal Symposium), 1619 - 1623.

Vaz, N., Mateus, M., Dias, J.M., 2011. Semidiurnal and spring-neap variations in the Tagus Estuary: Application of a process-oriented hydro-biogeochemical model. *Journal of Coastal Research* 64, 1619-1623.

Veloso-Gomes, F., Costa, J., Rodrigues, A., Taveira-Pinto, F., Pais-Barbosa, J., Neves, L.D., 2009. Costa da Caparica artificial sand nourishment and coastal dynamics. *Journal of Coastal Research*, pp.678-682.

Villaret, C., Hervouet, J.M., Kopmann, R., Merkel, U., Davies, A.G., 2013. Morphodynamic modeling using the Telemac finite-element system. *Computers & Geosciences*, 53, pp.105-113.

Villarreal, M.R., Bolding, K., Burchard, H., Demirov, E., 2005. Coupling of the GOTM turbulence module to some three-dimensional ocean models, pp. 225-237. In: Baumert, H.Z., J.H. Simpson, and J. Sündermann (eds.), *Marine Turbulence: Theories, Observations and Models*, Cambridge University Press, Cambridge, 630 pp.

Warner, J.C., Sherwood, C.R., Signell, R.P., Harris, C.K., Arango, H.G., 2008. Development of a three-dimensional, regional, coupled wave, current, and sediment-transport model. *Computers and Geosciences* 34, 1284–1306.

Whitehouse, R., Soulsby, R., Roberts, W., Mitchener, H., 2000. *Dynamics of estuarine muds*. Thomas Telford, London, 210 pp.

Wijeratne E.M.S., Pattiaratchi C., Eliot M., Haigh I.D., 2012. Tidal characteristics in Bass Strait, southeast Australia. *Estuarine, Coastal and Shelf Science* 114:156–165.

Wilcock, P.R., 1993. Critical shear stress of natural sediments. *Journal of Hydraulic Engineering* 119, 491–505.

Wilson, K.C., 1966. Bedload transport at high shear stress. *Journal of the Hydraulics Division, ASCE*, 92(6), 49–59.

Winterwerp, J.C., 2002. On the flocculation and settling velocity of estuarine mud. *Continental Shelf Research* 22, I339-I360.

Wu, W., Wang, S.S.Y., Jia, Y., 2000. Nonuniform sediment transport in alluvial rivers. *Journal of Hydraulic Research*, 38(6), 427–434.

Zyserman, J., Fredsoe, J., 1994. Data analysis of bed concentration of suspended sediment. *Journal of Hydraulic Engineering* 120 (9), 1021–1042.



## List of Figures

Figure 2.1 – Geometry features of the south-eastern Brazilian shelf (right) and Paranaguá estuarine system (left) with wetlands, showing the tidal gauges sites used for model validation. ....	10
Figure 2.2 – Area covered by the local (left) and regional (right) scale models .....	14
Figure 2.3 – Amplitudes (m) of M2, S2 and M3 tidal constituents from model results (left) and differences (cm) from FES2012 tidal solution (right).....	19
Figure 2.4 – Amplitudes and phases of the three most important diurnal and semidiurnal tidal constituents on the south-eastern Brazilian shelf. ....	20
Figure 2.5 – Amplitudes and phases of the most important tidal constituents in the tidal gauges located at Paranaguá estuary. ....	22
Figure 2.6 – Salinity and temperature results compared with Argo floats profiles in summer (above). Statistics between results and Argo floats profiles in January 2013 (below). ....	26
Figure 2.7 – Salinity and temperature results compared with Argo floats profiles in winter (above). Statistics between results and Argo floats profiles in July 2013 (below). ....	27
Figure 2.8 – SST (°C) results compared with satellite measurements in summer (left) and in winter (right). ....	28
Figure 2.9 – Statistics between SST (°C) results and satellite measurements in January 2013 (left) and July 2013 (right). ....	28
Figure 3.1- Tagus estuary area according to the WFD (2000/60/EC) (darker area) and the location of the monitoring stations (left). Bathymetry (m) of the Tagus estuary relative to the hydrographic zero (2.08 meters below the mean sea level in Cascais). Negative depths represent the intertidal zones that can be above water in low tides. Locations of the tide gauges used to verify the model results are also shown (right). ....	37
Figure 3.2 - Monthly average Tagus river flow (A) and CSS load (B) in 2012 (black) and in an average year (grey). ....	41
Figure 3.3 - Comparison between the harmonic analysis for data (■) and model results in 2012 (*) for the two most important tidal components in the Tagus estuary .....	43
Figure 3.4 - Comparison between the velocity modulus results (–) and data (■) measured by the ADCP installed on buoy B2 for the period between July and December of 2012 (A), with detail to the August month (B). The water level (...) is plotted to show the effect of tide on velocity in a spring tide (C) and a neap tide (D) .....	44
Figure 3.5 - Comparison of simulated (–) cohesive suspended sediment (CSS) concentrations and measured data in the reference year (2012) (*) and the maximum, median and minimum of the monthly data series between 2004 and 2012 (†) .....	46

Figure 3.6 - Simulated (–) cohesive suspended sediment (CSS) concentrations ( $\text{mg L}^{-1}$ ) and turbidity data (■) measured by multiparametric probes installed in the buoys B1 and B2 between June and December 2012.....	48
Figure 3.7 - Cohesive suspended sediment (CSS) mass (t) in the Tagus estuary delimited area for the five simulated years (A), during the third simulated year (B) - with waves (black) and without waves (gray) and comparison between the third simulated year with (black) and without (gray) bottom initialization (C) .....	49
Figure 3.8 - Initial (A) and final bottom sediment mass ( $\text{kg m}^{-2}$ ) after the first (B), second (C) and third (D) year of simulation .....	50
Figure 4.1 – Four compartments used for modelling sediment dynamics. The different colours in the settled layers represent sediment stratigraphy. ....	57
Figure 4.2 - Processes associated with the different model compartments. ....	57
Figure 4.3 – Equilibrium profiles of velocity (left) and suspended sediment concentration (right) computed by using different numbers (k) of vertical layers compared with analytical solutions. ....	70
Figure 4.4 – Bed load for non-cohesive sand-mud mixtures. Results of bed load transport versus bed shear stress for different mud content compared with the experimental analysis of Murray (1977). ....	71
Figure 4.5 – Consolidation of cohesive sediments in a 2 m deep settling column. Model results of bulk density for 0.11, 0.92, and 14 days compared with the experimental data of Toorman and Berlamont (1993). The experiment duration was extended to assess model results after longer periods (1 year and 10 years). ....	72
Figure 4.6 - Geometry of the flume and trench including the locations of the different measured profiles (adapted from van Rijn, 1987) .....	72
Figure 4.7 - Measured and computed profiles of velocity and sediment concentration at the beginning of the experiment (before bed changes) .....	73
Figure 4.8 – Trench migration in a flume. Figure 4.8A - Results with morphological acceleration factors varying from 1 to 300. Figure 4.8B - Contribution of bed load and suspended load to the final bed profile. Figure 4.8C and Figure 4.8D - Results for the trenches with side slopes of 1:7 and 1:10, respectively, considering the bed load equation of Meyer-Peter and Müller (1948) and the bed load equation of Soulsby and Damgaard (2005). ....	75
Figure 4.9 – Morphological evolution of a schematic estuary. The initial and resultant bathymetries after a period of 10, 100, 200, and 300 years are shown from the left to right. The initial bathymetry was defined as uniform (1 m deep), with the exception of the upper estuary. Negative depths represent intertidal zones that may be covered in high tides and uncovered in low tides. Channels	

with maximum depths near 20 m were generated for the given hydrodynamic conditions and sand diameters. ....	77
Figure 4.10 – Sediment distribution in the Tagus Estuary. Data (left) from Canário and Vale (2007) and model results (right) after a warm-up run in which sediment fractions were distributed according to the local hydrodynamic conditions. ....	78
Figure 5.1– Model results for the breakwater’s length to distance ratio of 0.2. Bathymetry (left), waves (middle) and currents (right) for the initial condition (above) and near equilibrium (below) after 9 years. The thicker isoline in the bathymetry represents the shoreline, whereas the remaining represent the 1 m, 2 m, 3 m and 4 m isobaths. ....	93
Figure 5.2 – Model results for the breakwater’s length to distance ratio of 0.5. Bathymetry (left), waves (middle) and currents (right) for the initial condition (above) and near equilibrium (below) after 18 years. The thicker isoline in the bathymetry represents the shoreline, whereas the others represent the 1 m, 2 m, 3 m and 4 m isobaths. ....	94
Figure 5.3 – Model results for the breakwater’s length to distance ratio of 1.0. Bathymetry (left), waves (middle) and currents (right) for the initial condition (above) and near equilibrium (below) after 27 years. The thicker isoline in the bathymetry represents the shoreline, whereas the others represent the 1 m, 2 m, 3 m and 4 m isobaths. ....	95
Figure 5.4 - Model results for the breakwater’s length to distance ratio of 2.0. Bathymetry (left), waves (middle) and currents (right) for the initial condition (above) and near equilibrium (below) after 18 years. The thicker isoline in the bathymetry represents the shoreline, whereas the others represent the 1 m, 2 m, 3 m and 4 m isobaths. ....	96
Figure 5.5 - Groyne with a length of 100 m from the shoreline. Bathymetry (left), waves (middle) and currents (right) for the initial condition (above) and near equilibrium (below) after 9 years. The thicker isoline in the bathymetry represents the shoreline, whereas the others represent the 1 m, 2 m, 3 m and 4 m isobaths. ....	98
Figure 5.6 – Groyne with a length of 200 m from the shoreline. Bathymetry (left), waves (middle) and currents (right) for the initial condition (above) and near equilibrium (below) after 9 years. The thicker isoline in the bathymetry represents the shoreline, whereas the others represent the 1 m, 2 m, 3 m and 4 m isobaths. ....	99
Figure 5.7 – Simulated sandbars for different wave heights. The horizontal plane of the bathymetry (above) and a vertical cut with velocity modulus and vectors (below). Left: Initial condition. Middle: After 45 days of morphological evolution with 1.5 m wave height. Right: After additional 45 days of morphological evolution with 1.0 m wave height. ....	102

Figure 5.8 – Bathymetries of the Tagus Estuary hydrodynamic model (left) and the wave model (right) created to propagate the waves until the Tagus Estuary mouth. The domain of the Costa da Caparica model is presented by the black rectangle and the location of the Port of Lisbon wave buoy is indicated by the black triangle. ....	103
Figure 5.9 – Residual velocity in the Tagus Estuary mouth at the surface (left) and near the bottom (right) obtained from the three-dimensional baroclinic model for the Tagus Estuary. ....	104
Figure 5.10 - Wave conditions for the winter of 2013/2014 obtained from the Portuguese Coast wave model in the location of the Port of Lisbon wave buoy. ....	105
Figure 5.11 – Velocity results of the Costa da Caparica model during flood (left) and ebb (right) tides at the surface (above) and near the bottom (below) without considering the wave’s effect on the hydrodynamics.....	106
Figure 5.12 – Wave results of the Costa da Caparica model. ....	107
Figure 5.13 - Velocity results of the Costa da Caparica model during the flood (left) and ebb (right) tides at the surface (above) and near the bottom (below) considering the wave’s effect on the hydrodynamics.....	107
Figure 5.14 – Results of bed load sediment transport for the scenarios without waves (above) and under extreme wave conditions (below).....	108

## List of Tables

Table 2.1 – Features of the domains .....	16
Table 2.2 – Coordinates and data series period of the tidal gauges.....	18
Table 2.3 – Sum of the amplitudes (m) and relative importance of the main tidal constituents in different frequency bands .....	18
Table 2.4 – Relative differences for amplitude (%) and absolute differences for phase (°) between model’s results and tidal gauge data on the shelf.....	21
Table 2.5 – Relative differences for amplitude (%) and absolute differences for phase (°) between the different scenarios and tidal gauge data inside the Paranaguá estuarine system .....	24
Table 2.6 – Mean absolute error of amplitudes (cm) and phases (°) for the five most important tidal constituents .....	25
Table 3.1 - Parameters used in the calculation of the cohesive sediment transport.....	39
Table 4.1 – Coefficients for the bed load equation based on different sources .....	63
Table 5.1– Detached breakwaters considered for test case scenarios .....	92